

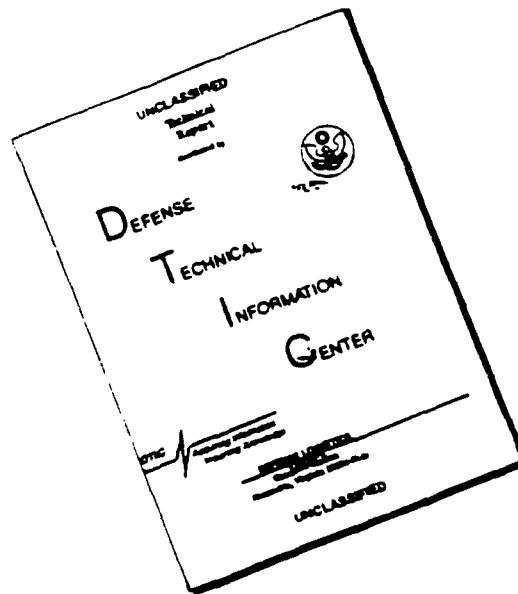
AD-A267 590 TION PAGE

Form Approved
OMB No 0704-0188

average 1 hour per response, including the time for reviewing instructions, searching existing data sources, gathering the information, and sending comments regarding this burden estimate or any other aspect of this collection of information, Washington Headquarters Services, Directorate for Information Operations and Reports, 1215 Jefferson Management and Budget, Paperwork Reduction Project (0704-0188), Washington, DC 20503

1. AGENCY USE ONLY (Leave blank)		2. REPORT DATE Dec 1990		3. REPORT TYPE AND DATES COVERED THESIS/DISSERTATION	
4. TITLE AND SUBTITLE Analysis of Global Radiation Budgets and Cloud Forcing Using Three-Dimensional Cloud Nephanalysis Data Base				5. FUNDING NUMBERS	
6. AUTHOR(S) Bruce Mitchell					
7. PERFORMING ORGANIZATION NAME(S) AND ADDRESS(ES) AFIT Student Attending: Univ of Utah				8. PERFORMING ORGANIZATION REPORT NUMBER AFIT/CI/CIA- 93-078	
9. SPONSORING/MONITORING AGENCY NAME(S) AND ADDRESS(ES) DEPARTMENT OF THE AIR FORCE AFIT/CI 2950 P STREET WRIGHT-PATTERSON AFB OH 45433-7765				10. SPONSORING/MONITORING AGENCY REPORT NUMBER	
11. SUPPLEMENTARY NOTES					
12a. DISTRIBUTION / AVAILABILITY STATEMENT Approved for Public Release IAW 190-1 Distribution Unlimited MICHAEL M. BRICKER, SMSgt, USAF Chief Administration				12b. DISTRIBUTION CODE	
13. ABSTRACT (Maximum 200 words)					
93 8 05 1 20					
93-18072					
14. SUBJECT TERMS				15. NUMBER OF PAGES 97	
				16. PRICE CODE	
17. SECURITY CLASSIFICATION OF REPORT		18. SECURITY CLASSIFICATION OF THIS PAGE		19. SECURITY CLASSIFICATION OF ABSTRACT	
				20. LIMITATION OF ABSTRACT	

DISCLAIMER NOTICE



THIS DOCUMENT IS BEST
QUALITY AVAILABLE. THE COPY
FURNISHED TO DTIC CONTAINED
A SIGNIFICANT NUMBER OF
PAGES WHICH DO NOT
REPRODUCE LEGIBLY.



DEPARTMENT OF THE AIR FORCE
USAF ENVIRONMENTAL TECHNICAL APPLICATIONS CENTER (AWSI)
SCOTT AIR FORCE BASE, ILLINOIS 62225-5438

REPLY TO
ATTN OF

USAFETAC/DOS (Capt Mitchell, DSN576-3543)
859 BUCHANNAN ST
SCOTT AFB IL 62225-5116

18 Dec 92

SUBJECT

Master's Thesis

93-078

TO

AFIT/CIR (Maj Smith)

Per conversation on 18 Dec 92, I have enclosed my completed master's thesis to be given to the AFIT Technical Library.

Bruce G. Mitchell

BRUCE G. MITCHELL, Capt, USAF

Atch
Thesis

ANALYSIS OF GLOBAL RADIATION BUDGETS AND CLOUD FORCING
USING THREE-DIMENSIONAL CLOUD NEPHANALYSIS DATA BASES

by

Bruce Mitchell

A thesis submitted to the faculty of
The University of Utah
in partial fulfillment of the requirements for the degree of

Master of Science

Department of Meteorology

University of Utah

December 1990

Accession For	
NTIS CRA&I	<input checked="checked" type="checkbox"/>
DTIC TAB	<input type="checkbox"/>
Unannounced	<input type="checkbox"/>
Justification	
By	
Distribution /	
Availability Codes	
Dist	Avail and/or Special
A-1	

DTIC QUALITY INSPECTED 3

Copyright © Bruce Mitchell 1992

All Rights Reserved

THE UNIVERSITY OF UTAH GRADUATE SCHOOL

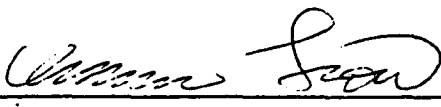
SUPERVISORY COMMITTEE APPROVAL

of a thesis submitted by

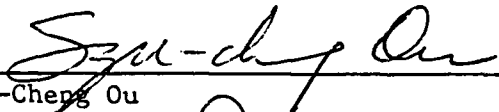
Bruce Gordon Mitchell

This thesis has been read by each member of the following supervisory committee and by majority vote has been found to be satisfactory.

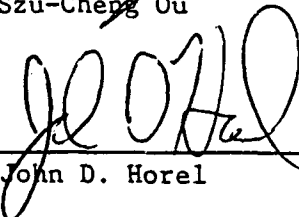
August 23, 1990


Chairman: Kuo-Nan Liou

August 23, 1990


Szu-Cheng Ou

August 23, 1990


John D. Horel

THE UNIVERSITY OF UTAH GRADUATE SCHOOL

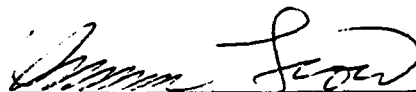
FINAL READING APPROVAL

To the Graduate Council of the University of Utah:

I have read the thesis of Bruce Gordon Mitchell in its final form and have found that (1) its format, citations, and bibliographic style are consistent and acceptable; (2) its illustrative materials including figures, tables, and charts are in place; (3) the final manuscript is satisfactory to the Supervisory Committee and is ready for submission to the Graduate School.

August 23, 1990

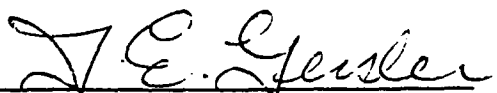
Date



Kuo-Nan Liou

Chair, Supervisory Committee

Approved for the Major Department



J.E. Geisler
Chair/Dean

Approved for the Graduate Council

B. Gale Dick

Dean of The Graduate School

ABSTRACT

A one-dimensional radiative transfer model was used to compute the global radiative budget at the top of the atmosphere (TOA) and the surface for January and July, 1979. The model was also used to determine the global cloud radiative forcing for all clouds and for high and low cloud layers. In the computations, we used the monthly cloud data derived from the Air Force Three-Dimensional Cloud Nephanalysis (3DNEPH). These data were used in conjunction with conventional temperature and humidity profiles analyzed during the 1979 First GARP (Global Atmospheric Research Program) Global Experiment (FGGE) year. Global surface albedos were computed from available data and were included in the radiative transfer analysis. Comparisons of the model-produced outgoing solar and infrared fluxes with those derived from Nimbus 7 Earth Radiation Budget (ERB) data were made to validate the radiative model and cloud cover. For reflected solar and emitted infrared (IR) flux, differences within 20 W/m^2 were shown. These differences are reasonable in view of the uncertainties in the ERB data.

A number of parameters have been derived to isolate the effects of clouds on the radiation budgets at TOA and the surface and heating rates in the atmosphere. Comparisons of the model derived surface solar and infrared fluxes with those from Griffin were made to cross check the radiative transfer model at the surface. For the reflected solar and emitted IR flux, differences within 10 W/m^2 were shown.

These differences are reasonable in light of the inherent differences of the two radiative transfer models. The cloud radiative forcing results due to all clouds at TOA compared reasonably well with those presented by Slingo and Slingo. As at TOA, cloud radiative forcing at the surface was computed and had similar results.

The heating rates were then computed and analyzed. The overall effect of all clouds is to cool directly above them and to warm below and in them. The net effects of low and high clouds are similar to all clouds. However, the difference lies in the magnitude of the warming and cooling for each of the cloud decks and the location in the atmosphere where it is taking place.

TABLE OF CONTENTS

ABSTRACT.	iv
LIST OF FIGURES	vii
ACKNOWLEDGMENTS	xi
CHAPTER	
1. INTRODUCTION	1
2. MODEL INPUT DATASETS	3
2.1 Surface Albedo.	3
2.2 Atmospheric Profile Data.	6
2.3 3DNEPH Global Cloud Climatology	6
3. MODEL SENSITIVITY TESTS.	25
3.1 ERB Data Base	25
3.2 Radiative Transfer Parameterizations.	26
3.3 Cloud Overlap Adjustments	29
3.4 Comparison of Model and ERB Results	30
4. CLOUD RADIATIVE FORCING.	60
4.1 TOA Fluxes.	60
4.1.1 Cloud Solar Forcing.	60
4.1.2 Cloud IR Forcing	61
4.1.3 Net Cloud Forcing.	65
4.2 Surface Fluxes.	73
4.3 Heating Rates	78
4.3.1 Forcing Due To All Clouds.	78
4.3.2 Forcing Due To High Clouds	84
4.3.3 Forcing Due To Low Clouds.	89
5. SUMMARY AND CONCLUSIONS.	94
REFERENCES.	98
VITA.	100

LIST OF FIGURES

<u>Figure</u>	<u>Page</u>
2.1 January 1979 global monthly average surface albedo. Contour interval (.2).	4
2.2 July 1979 global monthly average surface albedo. Contour interval (.2).	5
2.3 January 1979 zonally average surface albedo.	7
2.4 July 1979 zonally average surface albedo.	8
2.5 January monthly average low cloud amount (%). Model 3DNEPH (top) versus H-S 3DNEPH (bottom). Contour interval for the top is 20% and is as shown for the bottom.	10
2.6 January monthly average middle cloud amount (%). Model 3DNEPH (top) versus H-S 3DNEPH (bottom). Contour interval for the top is 20%, and is as shown for the bottom.	12
2.7 January monthly average high cloud amount (%). Model 3DNEPH (top) versus H-S 3DNEPH (bottom). Contour interval for the top is 10%, and is as shown for the bottom.	13
2.8 January monthly average total cloud amount (%). Model 3DNEPH (top) versus H-S 3DNEPH (bottom). Contour interval for the top is 10%, and is as shown for the bottom.	15
2.9 July monthly average low cloud amount (%). Model 3DNEPH (top) versus H-S 3DNEPH (bottom). Contour interval for the top is 20%, and is as shown for the bottom.	16
2.10 July monthly average middle cloud amount (%). Model 3DNEPH (top) versus H-S 3DNEPH (bottom). Contour interval for the top is 20%, and is as shown for the bottom.	17
2.11 July monthly average high cloud amount (%). Model 3DNEPH (top) versus H-S 3DNEPH (bottom). Contour interval for the top is 10%, and is as shown for the bottom.	19
2.12 July monthly average total cloud amount (%). Model 3DNEPH (top) versus H-S 3DNEPH (bottom). Contour interval for the top is 10%, and is as shown for the bottom.	20

2.13	January 1979 zonal average 3DNEPH total cloud (%), Model versus H-S.	22
2.14	July 1979 zonal average 3DNEPH total cloud (%), Model versus H-S.	23
3.1	Global Nimbus 7 ERB grid target areas.	27
3.2	Computed zonal averages of the daily average NFOV net flux (...) plotted against published values from the NFOV (____) and WFOV (---) radiometers for January 1979.	28
3.3	January 1979, Model (top) versus ERB (bottom), global net downward TOA solar flux (W/m^2). Contour interval is 40 W/m^2	31
3.4	January 1979, Model (top) versus ERB (bottom), global outgoing TOA IR flux (W/m^2). Contour interval is 40 W/m^2	32
3.5	July 1979, Model (top) versus ERB (bottom), global net downward TOA solar flux (W/m^2). Contour interval is 40 W/m^2	34
3.6	July 1979, Model (top) versus ERB (bottom), global outgoing TOA IR flux (W/m^2). Contour interval is 40 W/m^2	35
3.7	January 1979, Model - ERB, global net downward TOA solar flux (W/m^2). Contour interval is 40 W/m^2	37
3.8	January 1979, Model - ERB, global out going TOA IR flux (W/m^2). Contour interval is 40 W/m^2	39
3.9	July 1979, Model - ERB, global net downward TOA solar flux (W/m^2). Contour interval is 40 W/m^2	40
3.10	July 1979, Model - ERB, global out going TOA IR flux (W/m^2). Contour interval is 40 W/m^2	41
3.11	January 1979, Model versus ERB, zonal average net downward TOA solar flux.	43
3.12	January 1979, Model versus ERB, zonal average outgoing TOA IR flux.	44
3.13	July 1979, Model versus ERB, zonal average net downward TOA solar flux.	45

3.14	July 1979. Mode versus ERB. zonal average outgoing TOA IR flux.	47
3.15	January 1979. Model global downward surface solar flux (W/m^2). Contour interval is 40 W/m^2	48
3.16	January 1979. Model global upward surface IR flux (W/m^2). Contour interval is 20 W/m^2	50
3.17	July 1979. Model global downward surface solar flux (W/m^2). Contour interval is 40 W/m^2	51
3.18	July 1979. Model global upward surface IR flux (W/m^2). Contour interval is 40 W/m^2	53
3.19	January 1979. zonal average downward surface solar flux. .	54
3.20	January 1979. zonal average upward surface IR flux. . . .	56
3.21	July 1979. zonal average downward surface solar flux. . .	57
3.22	July 1979. zonal average upward surface IR flux.	59
4.1	January 1979. Model global net downward TOA solar flux (W/m^2) for a partially cloudy sky. Contour interval is 40 W/m^2	62
4.2	January 1979. Model global net downward TOA solar flux (W/m^2) for a clear sky. Contour interval is 60 W/m^2	63
4.3	January 1979. Model global cloud forcing of the net incoming TOA solar flux (W/m^2). Contour interval is 60 W/m^2	64
4.4	January 1979. Model global outgoing TOA IR flux (W/m^2) for a partially cloudy sky. Contour interval is 40 W/m^2	66
4.5	January 1979. Model global outgoing TOA IR flux (W/m^2) for a clear sky. Contour interval is 40 W/m^2	67
4.6	January 1979. Model global cloud forcing of the outgoing TOA IR flux (W/m^2). Contour interval is 40 W/m^2	68
4.7	January 1979. Model global net TOA flux (W/m^2) for a partially cloudy sky. Contour interval is 40 W/m^2	70
4.8	January 1979. Model global net TOA flux (W/m^2) for a clear sky. Contour interval is 40 W/m^2	71

4.9	January 1979. Model global cloud forcing of the net TOA flux (W/m^2). Contour interval is 40 W/m^2	72
4.10	January 1979. Model global net surface flux (W/m^2) for a partially cloudy sky. Contour interval is 40 W/m^2	74
4.11	January 1979. Model global net surface flux (W/m^2) for a clear sky. Contour interval is 40 W/m^2	76
4.12	January 1979. Model global cloud forcing of the net surface flux (W/m^2). Contour interval is 40 W/m^2	77
4.13	January 1979 solar heating rate. a) cloudy, contour interval 1K/day . b) clear, contour interval 1K/day . and c) solar cloud forcing, contour interval $.5\text{K/day}$	79
4.14	January 1979 IR heating rate. a) cloudy, contour interval 1K/day . b) clear, contour interval 1K/day . and c) IR cloud forcing, contour interval $.5\text{K/day}$	81
4.15	January 1979 net heating rate. a) cloudy, contour interval 1K/day . b) clear, contour interval 1K/day . and c) net cloud forcing, contour interval $.5\text{K/day}$	83
4.16	January 1979 solar heating rate. a) cloudy, contour interval 1K/day . b) cloudy without high clouds, contour interval 1K/day . and c) solar cloud forcing, contour interval $.5\text{K/day}$	85
4.17	January 1979 IR heating rate. a) cloudy, contour interval 1K/day . b) cloudy without high clouds, contour interval 1K/day . and c) IR cloud forcing, contour interval $.5\text{K/day}$	87
4.18	January 1979 net heating rate. a) cloudy, contour interval 1K/day . b) cloudy without high clouds, contour interval 1K/day . and c) net cloud forcing, contour interval $.5\text{K/day}$	88
4.19	January 1979 solar heating rate. a) cloudy, contour interval 1K/day . b) cloudy without low clouds, contour interval 1K/day . and c) solar cloud forcing, contour interval $.5\text{K/day}$	90
4.20	January 1979 IR heating rate. a) cloudy, contour interval 1K/day . b) cloudy without low clouds, contour interval 1K/day . and c) IR cloud forcing, contour interval $.5\text{K/day}$	91
4.21	January 1979 net heating rate. a) cloudy, contour interval 1K/day . b) cloudy without low clouds, contour interval 1K/day . and c) net cloud forcing, contour interval $.5\text{K/day}$	93

ACKNOWLEDGMENTS

I would like to thank Professor Kuo-Nan Liou, my supervisory committee chairman, whose guidance throughout this project was vital to its completion. Professors John Horel and Steve Ou were my committee members. I appreciate their counseling and assistance in the preparation of this thesis, especially Professor Steve Ou, whose assistance during the analyses and research phase was essential to its completion. In addition, I would like to acknowledge Dr. Mike Griffin, whose discussions and assistance during the initial phase of this research were essential to the completion of this work. Finally, I thank my wife, Pamela, for her encouragement and understanding.

The research contained in this thesis has been supported, in part, by NASA Grant NAG-1050 and the Air Force Office of Scientific Research Grant AFOSR-87-0294 to the University of Utah.

CHAPTER 1

INTRODUCTION

Previous studies of cloud-radiation interactions and cloud forcing have generally used zonal mean clouds (Hunt, 1978; Le Treut and Laval, 1984) or clouds derived from geographical distributions (Meleshko and Wetherald, 1981). Generally, limited information on the cloud field was known except for the presence or absence of clouds. The cloud tops and bases, thicknesses, and physical types were usually estimated from climatology (Slingo and Slingo, 1988). Recognizing these shortcomings, the present study utilizes the Air Force Global Weather Central (AFGWC) 3DNEPH cloud data base which was compiled based on satellite data and ground observations, along with other data bases of atmospheric parameters that are concurrent in time and of sufficient quality and resolution. The methodology of how to use the 3DNEPH archive over the Northern Hemisphere was developed by Griffin (1987) and was modified for use here over the entire globe. In particular, three (low, middle, and high) cloud layers are compacted from the original 15 cloud layers. Using this input in a comprehensive, yet efficient radiative transfer model (Ou and Liou, 1987), the model-generated TOA radiative budgets were validated by comparing it to those derived by Griffin (1987) from the ERB data. Then, a comprehensive analysis of the surface radiation budget and cloud radiative forcing due to all clouds was performed using a

methodology similar to Ramanathan (1987). However, this study is unique because it not only looks at the cloud radiative forcing due to all clouds, but also due to high and low clouds. This will give us a comprehensive understanding of the role of these clouds in the radiative budget of the earth-atmosphere system.

A high resolution analysis over the entire globe will be performed, with a resolution of approximately $160 \times 160 \text{ km}^2$. In Chapter 2 of this thesis, model input data sets including their format are described, including surface albedo, atmospheric profile data, and 3DNEPH cloud climatology. The cloud climatology was compared to that of Henderson-Sellers (1986). In Chapter 3, the model radiation budgets at TOA are compared with ERB data. In Chapter 4, global cloud radiative forcing (both solar and IR) at TOA and surface are determined. The IR and solar heating rates are then calculated for the cases with and without clouds. Finally, a summary is given in Chapter 5.

CHAPTER 2

MODEL INPUT DATASETS

2.1 Surface Albedo

The methodology incorporated in this study to determine the global surface albedo is the same as that used by Griffin (1987) for his work on the Northern Hemisphere. Therefore, a description of the methodology will not be included in this study.

Each geographical type, along with its corresponding data source, that was used to define the surface albedo is listed in Table 2.1 (Griffin, 1987). Figures 2.1 and 2.2 are maps of the global surface albedo for January and July 1979. These two figures show that the surface albedo changes sharply along the continental coastlines.

Table 2.1 Surface albedo sources for each geographical type.

Geographical Type	Surface Albedo Source
Snow-free land	Matthews 1985 ($1^{\circ} \times 1^{\circ}$)
Snow covered land	Equation for snow albedo
Ice-free water	Zonally average values from HR 1979
Ice covered water	HR ($10^{\circ} \times 10^{\circ}$)

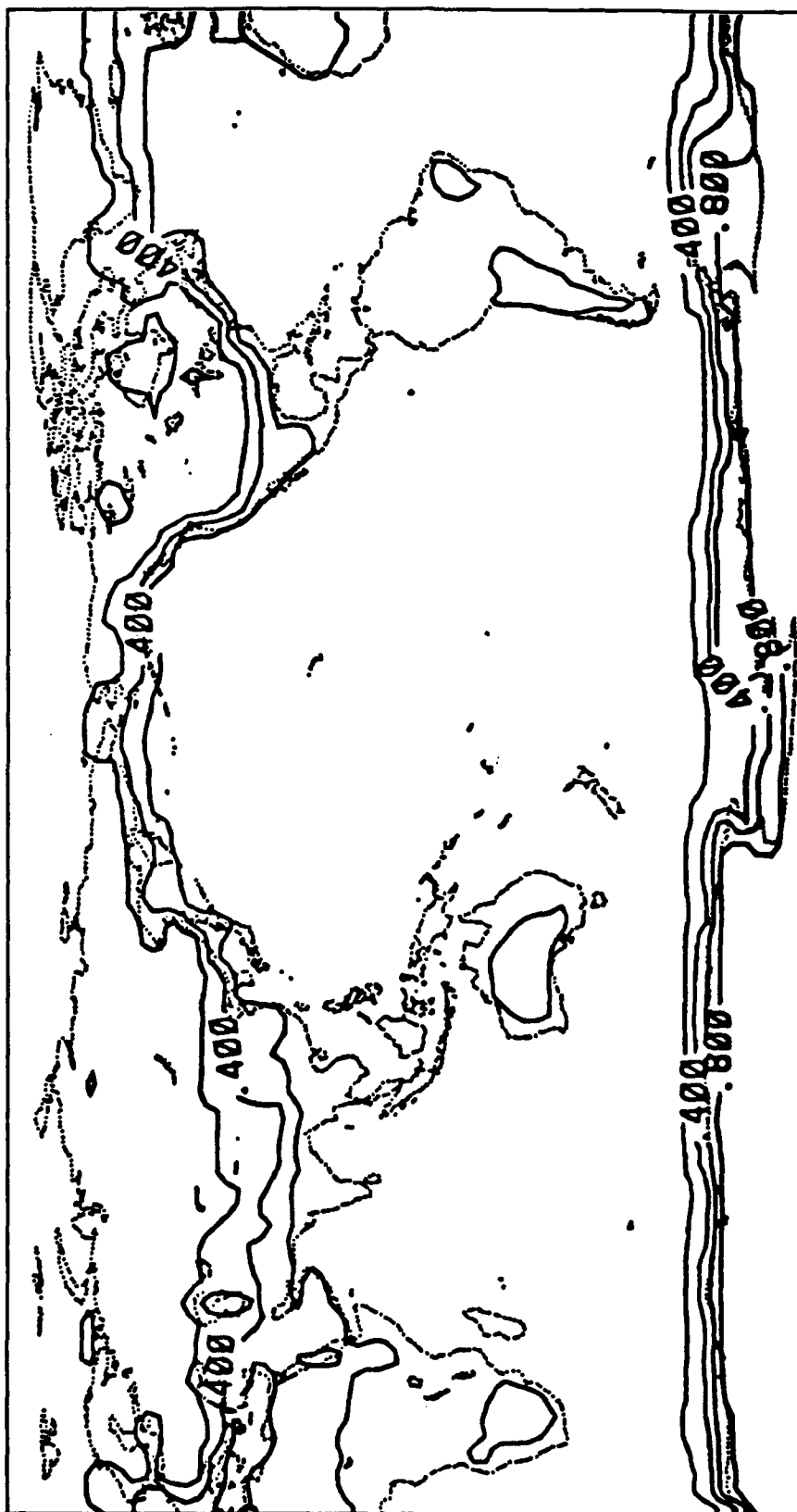


Fig 2.1 January 1979 global monthly average surface albedo. Contour interval (.2).

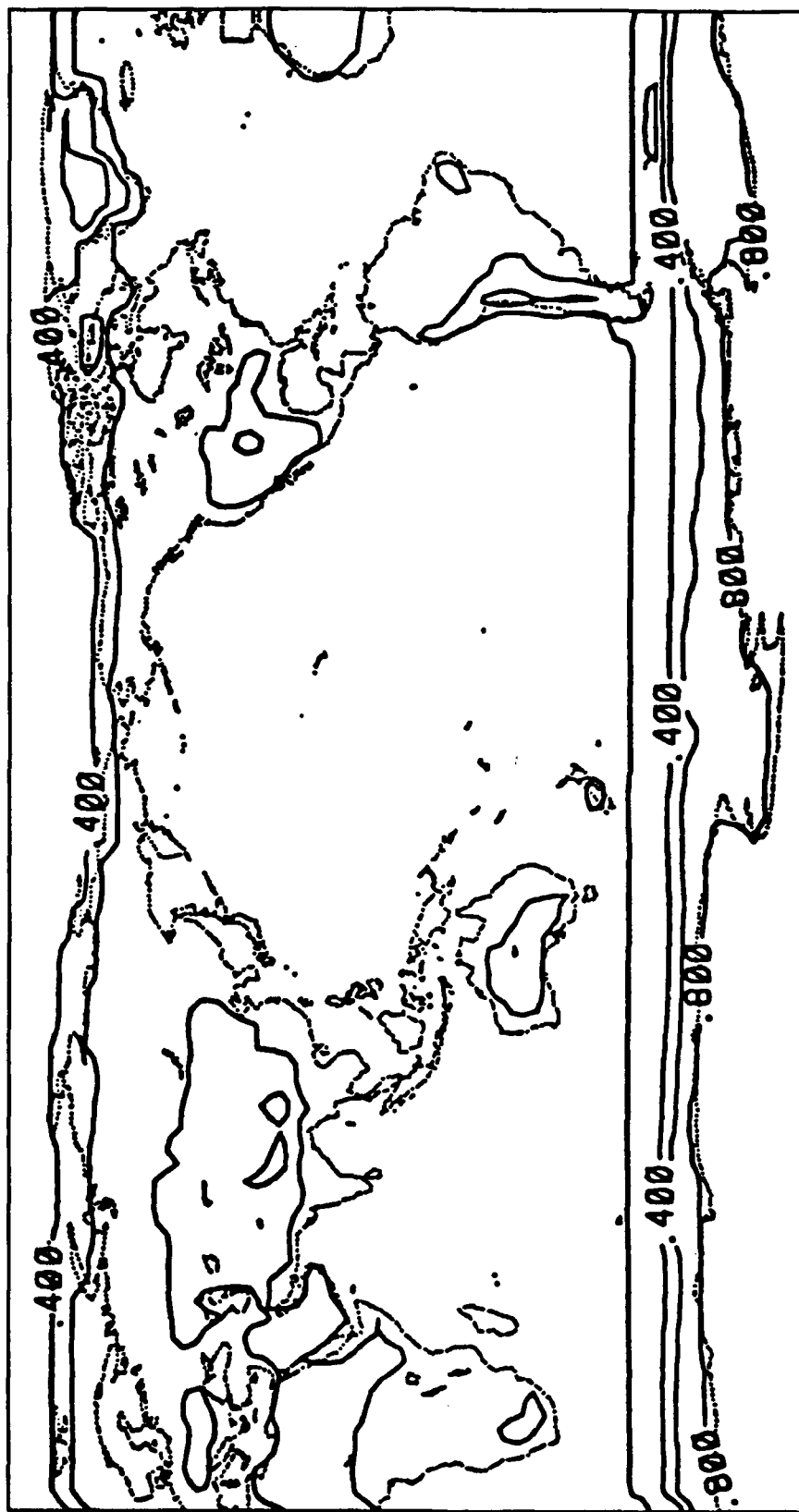


Fig 2.2 July 1979 global monthly average surface albedo. Contour interval (.2).

Although some of the changes in the surface albedo over land areas can be attributed to seasonal changes in vegetation, the greatest influence on the surface albedo is snow. The increase in snow cover in January causes the high surface albedo contours to move southward over the continents of North America and Eurasia. The reduction in pack ice around Antarctica in January causes the contours to retreat toward the South Pole. In July, the behaviors are reversed. Figures 2.3 and 2.4 depict the zonal average surface albedo as compared to Hummel and Reck (1979, hereafter referred to as HR) for January and July 1979. Overall, the model surface albedo distributions agree well with HR, with differences of no more than 15%.

In January (Figure 2.3), the differences in the Northern Hemisphere and Antarctica can be attributed to the model having more snow cover in the present scheme than HR. This is due to the fact that HR used seasonal values and the present scheme used specific monthly values. In July (Figure 2.4), the differences over Antarctica are also due to a greater amount of snow as compared to HR. The difference over the northern midlatitudes can also be attributed to the model having a finer resolution ($1^\circ \times 1^\circ$) than HR ($10^\circ \times 10^\circ$).

2.2 Atmospheric Profile Data

The methodology used to compute the global atmospheric profile data is the same that was used by Griffin (1987) for the Northern Hemisphere, so it will not be discussed here.

2.3 3DNEPH Global Cloud Climatology

The AFGWC 3DNEPH combined pilot reports, satellite, rawinsonde, and ground observations to produce a high resolution global cloud

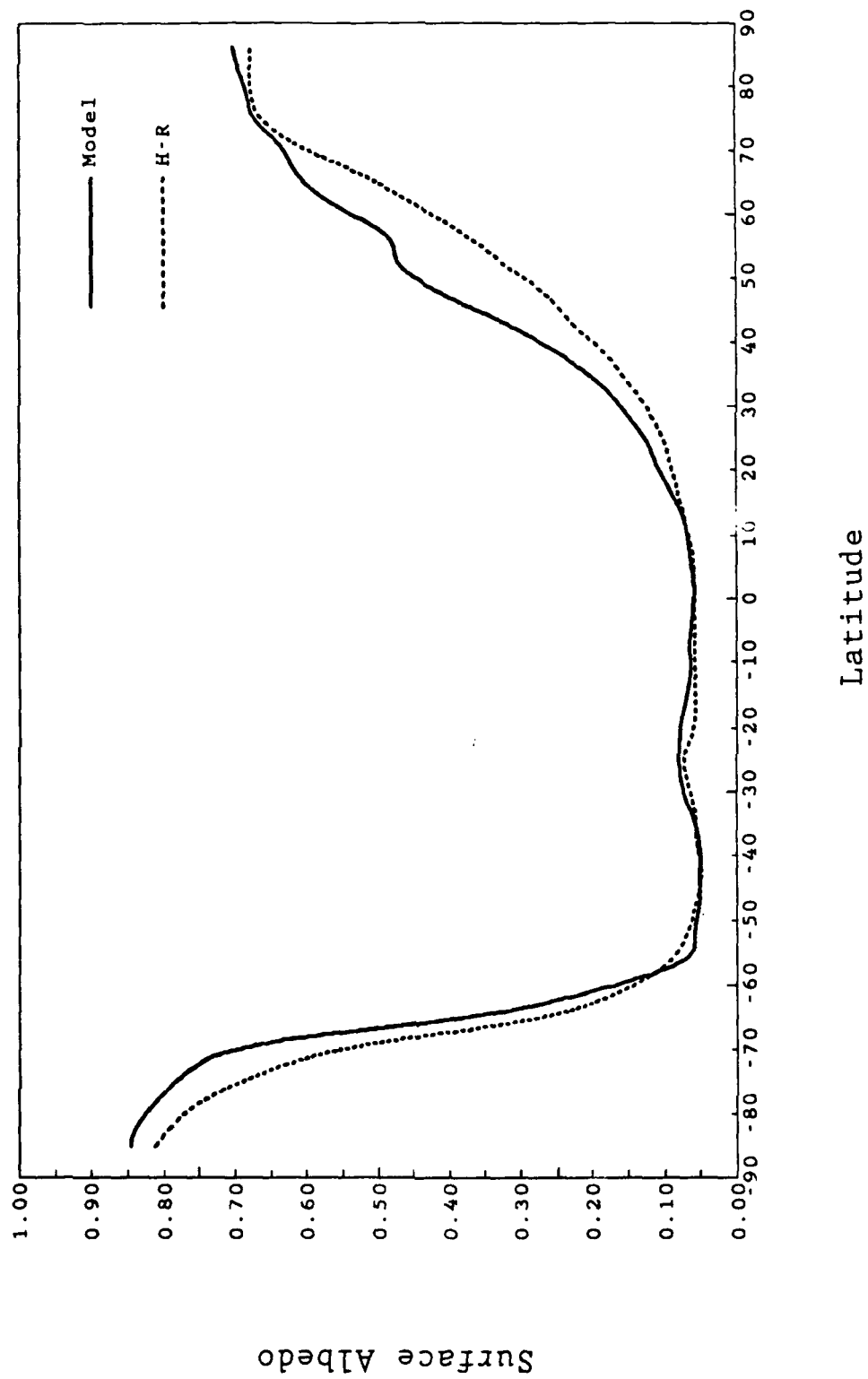


Fig 2.3 January 1979 zonally average surface albedo.

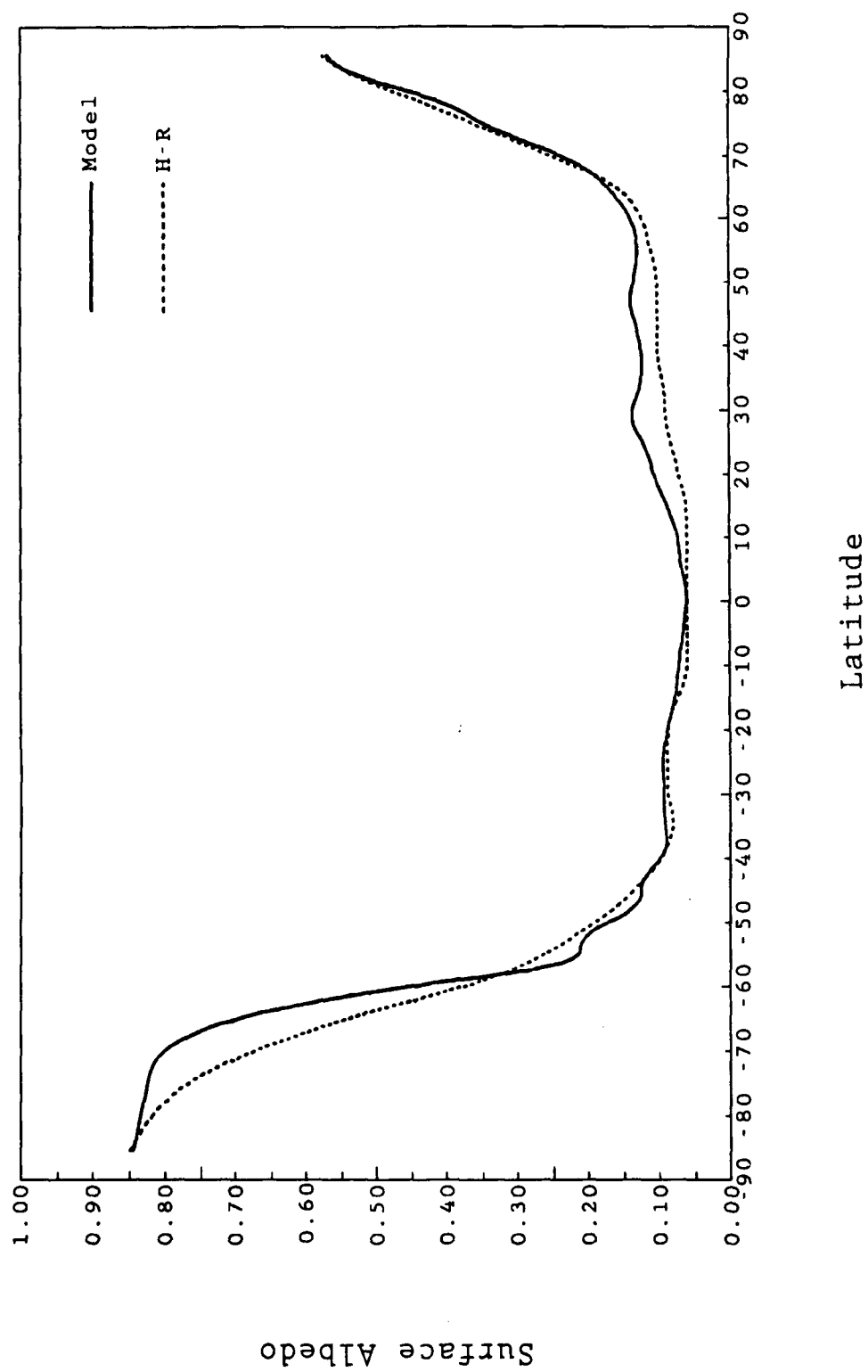


Fig 2.4 July 1979 zonally average surface albedo.

analysis. Griffin (1987) developed a methodology to compact the Northern Hemisphere 3DNEPH data from 15 cloud layers to 3 LMH (low, middle, and high) cloud layers. That methodology was used here to compact the Southern Hemisphere cloud layers. As described in Griffin, the Northern and Southern Hemispheres are divided into square grids of 262,144 points (512 x 512), each of which is overlaid onto a polar stereographic image of the hemispheres. The hemispheric grid is further divided into 64 (8 x 8) 3DNEPH boxes. Each box contains 4096 (64 x 64) grid points. Also, Griffin devised the methodology to convert the 3DNEPH Northern Hemisphere cloud data from its 64 box polar stereographic grid to the ERB, 1035 TA format. In this study, that methodology was converted in order to create a complete three-layer (low, middle, and high) 3DNEPH cloud data base for the Southern Hemisphere. This cloud data base, along with Griffin's Northern Hemisphere 3DNEPH cloud data base provides the model with a complete global data base.

Henderson-Sellers (1986; referred to as HS henceforth) also compiled a layered cloud climatology from a compressed version of the 3DNEPH data archive for the same two months in 1979 (January and July) as those used in this research. A comparison is made between the model's and HS' global monthly mean low, middle, high, and total cloud amounts.

Figure 2.5 depicts a comparison between the model (top) and HS (bottom) January 1979 low cloud average. Starting with North Africa, both the model and HS have from 0 to 20% low clouds. In Australia, both the model and HS have from 0 to 60% low clouds. Finally in the

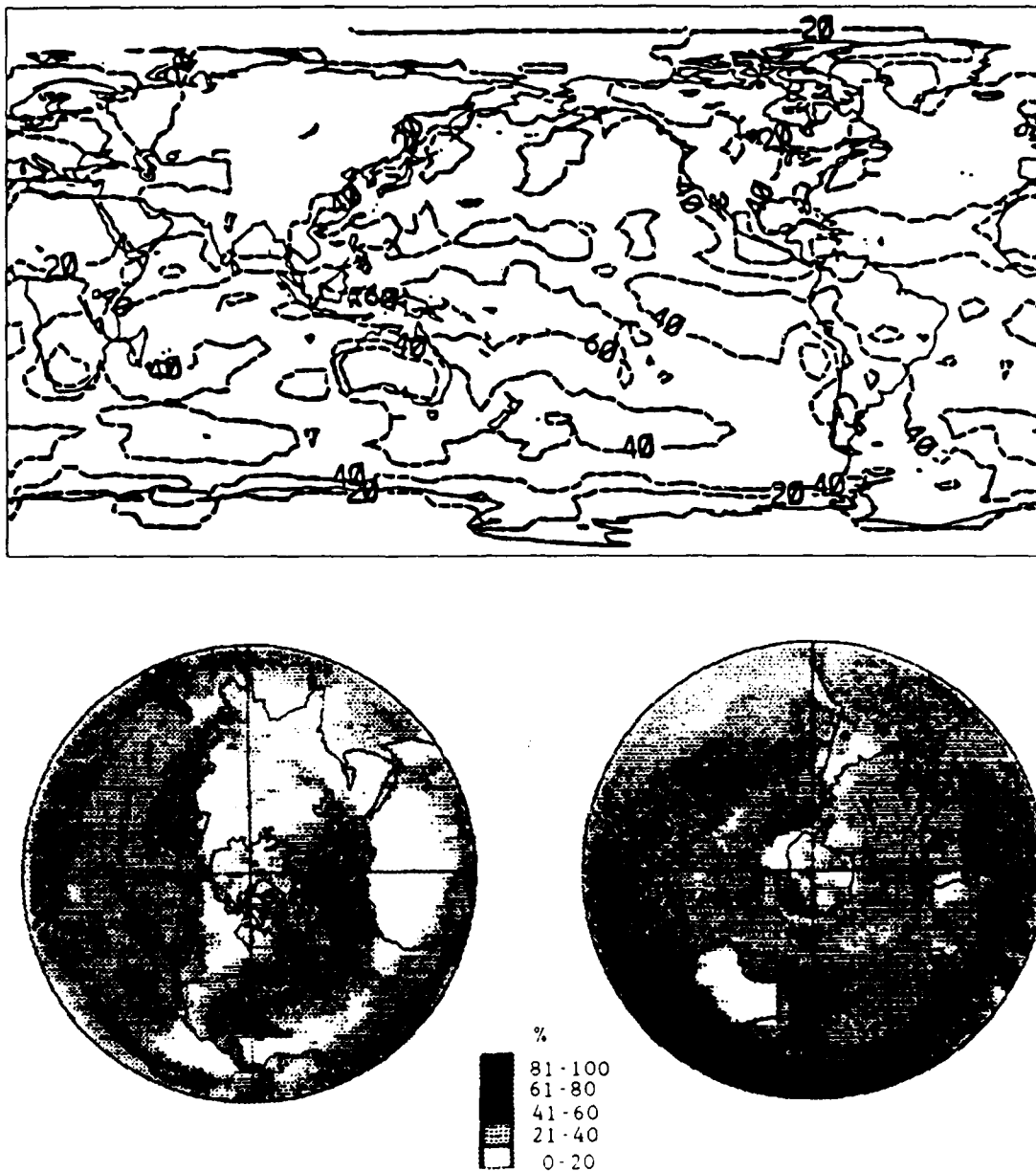


Fig 2.5 January monthly average low cloud amount (%). Model 3DNEPH (top) versus HS 3DNEPH (bottom). Contour interval for the top is 20% and is as shown for the bottom.

United States. both the model and HS have from 20 to 60% low clouds. Within the limits of the resolution of the contours, the model and HS low cloud amounts compare very well. Next, we will move up a layer and compare the middle cloud results.

Figure 2.6 is a comparison between the model (top) and HS (bottom) January 1979 middle cloud average. Starting again in North Africa, both the model and HS have 40 to 60% middle clouds. Moving southward to central Africa (Congo), the model and HS have 40 to 60% middle clouds with a small area that has 80% middle clouds. Finally in central South America, the model and HS have 40 to 60% middle clouds with a small area as high as 80% middle clouds, much like the Congo. Again, like the low cloud comparison, the middle cloud results for January 1979 compare very well. Next, we will move up one more layer and compare the high cloud layer results.

Figure 2.7 is a comparison between the model (top) and HS (bottom) January 1979 high cloud average. This time the comparison starts in the southeastern United States, with the model's high cloud average being between 20 and 30%, and HS' high cloud average in the range of 20 to 40%. In the South Pacific, the model shows high clouds ranging from 15% to greater than 20%, while HS' high cloud range is from 20 to 40%. In central South America, the model's high cloud average ranges from 10% to greater than 30%, while HS' high cloud average is in the 20 to 40% range. Clearly, within the resolution of the contours, the two high cloud results compare very well. Finally, we will end this portion by comparing the models' total cloud cover results.

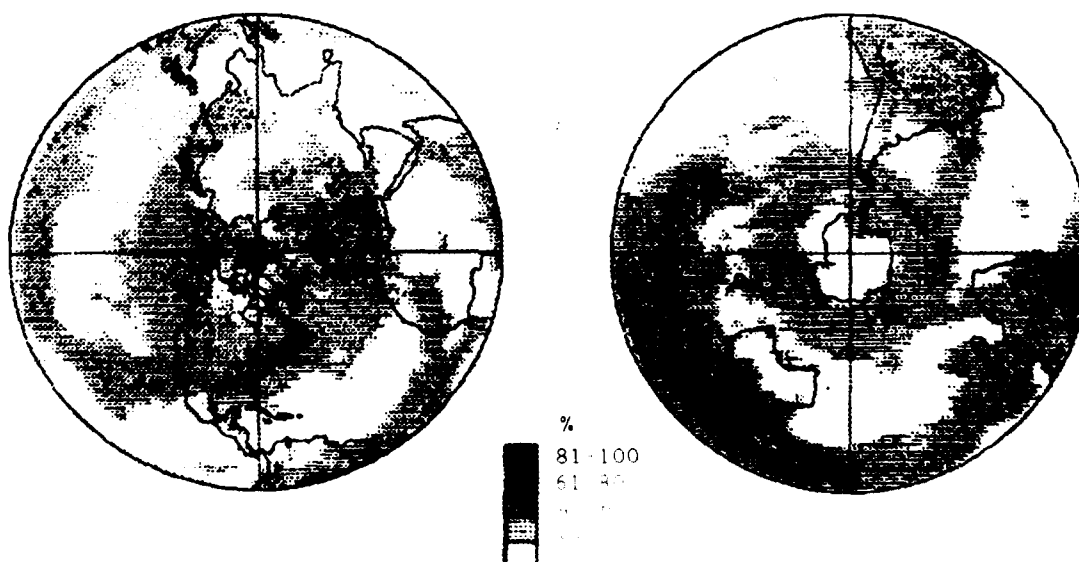
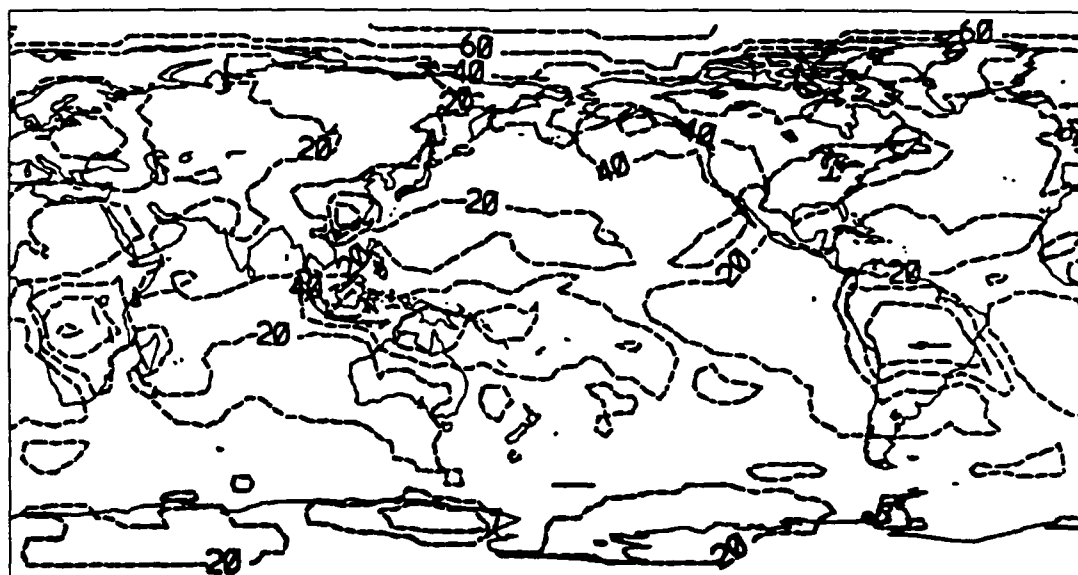


Fig 2.6 January monthly average middle cloud amount (%). Model 3DNEPH (top) versus HS 3DNEPH (bottom). Contour interval for the top is 20% and is is shown for the bottom.

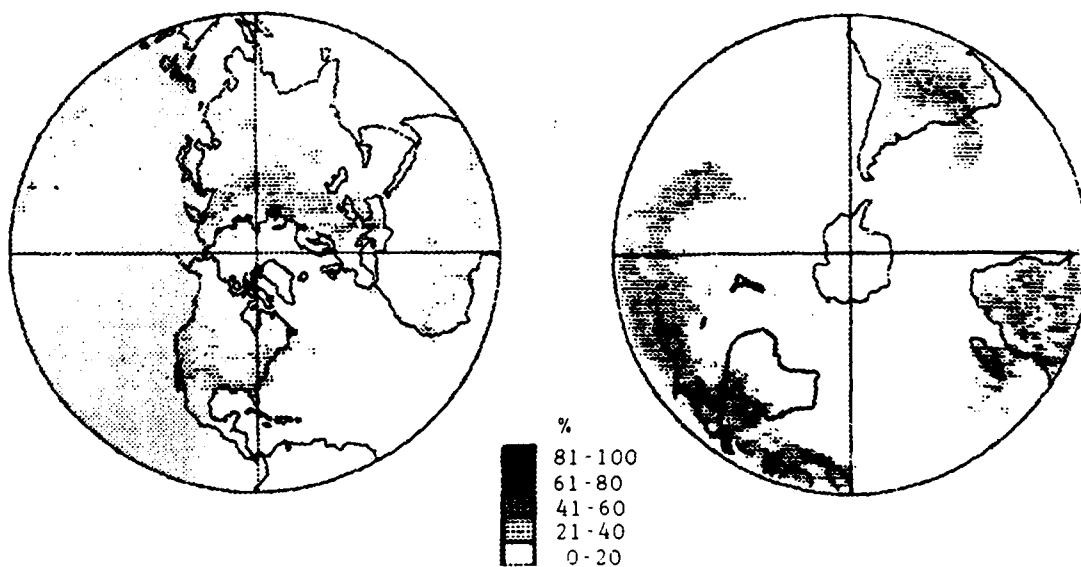
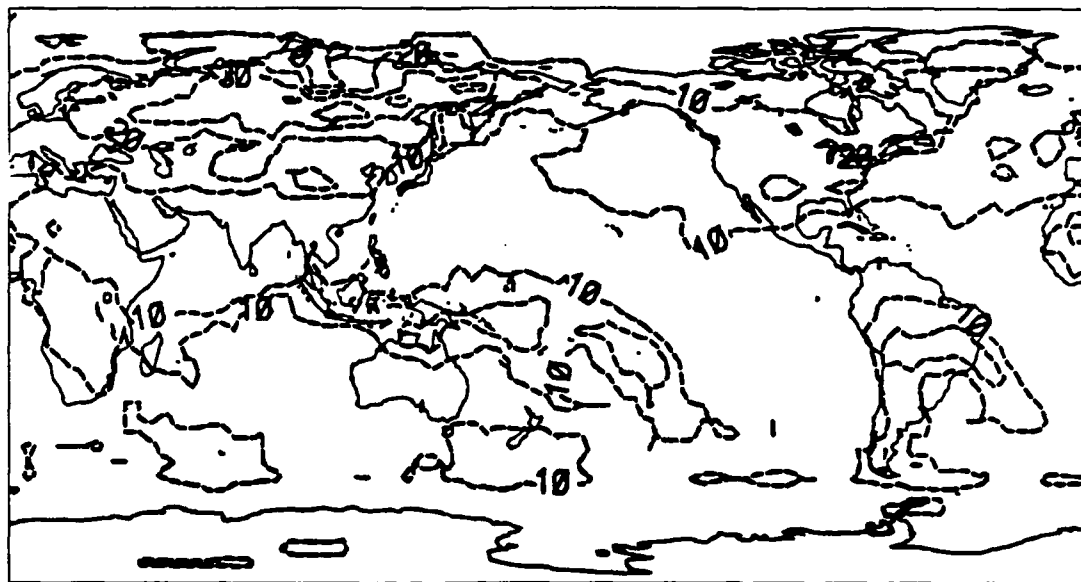


Fig 2.7 January monthly average high cloud amount (%), Model 3DNEPH (top) versus HS 3DNEPH (bottom). Contour interval for the top is 20% and is as shown for the bottom.

Figure 2.8 is a comparison between the model (top) and HS (bottom) January 1979 total cloud average. Starting with North Africa, both the model and HS have a 20 to 40% total cloud average. In Australia, both the model and HS have a 20 to 40% total cloud average. While in central South America, both the model and HS have a 60 to 80% total cloud average. Finishing in Europe, both the model and HS have a 40 to 60% total cloud average. As with the individual cloud layers, the comparison of the model's and HS' results is very good. Next, we will perform the same comparison for July 1979.

We will start this portion of the comparison by first examining the low cloud average. Figure 2.9 depicts a comparison between the model (top) and HS (bottom) July 1979 low cloud cover averages. Starting in North Africa, the model has 20 to 40% low clouds while HS has a greater range of 0 to 40% low clouds. Over the Australian continent, the model displays 20 to 40% low clouds while HS displays a greater range of 0 to 40% low clouds. In South America, the model has 20 to 40% low clouds and HS has 0 to 40% low clouds. In the United States, the model shows 20 to 40% low clouds while HS has 0 to 40% low clouds. Within the resolution of the contours, the model's and HS' low cloud results compare very well. Now, we will move up a layer and study the middle cloud averages.

Figure 2.10 is a comparison between the model (top) and HS (bottom) July 1979 middle cloud averages. Over the United States, the model shows 20 to 40% middle clouds while HS shows 0 to 40% middle clouds. In North Africa and the Middle East, both the model and HS have 0 to 20% middle clouds. Over the Australian continent, the model

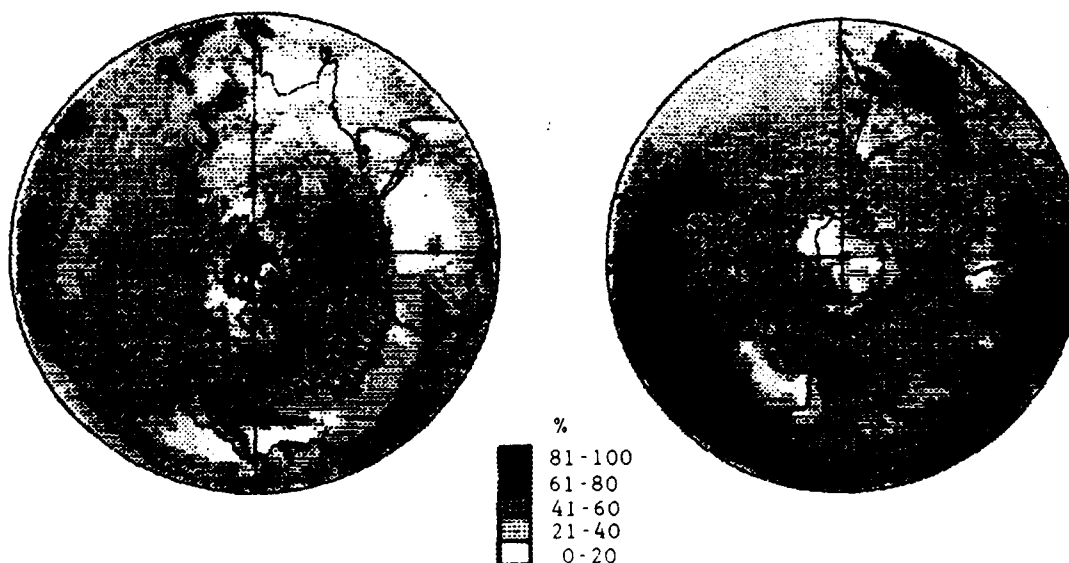
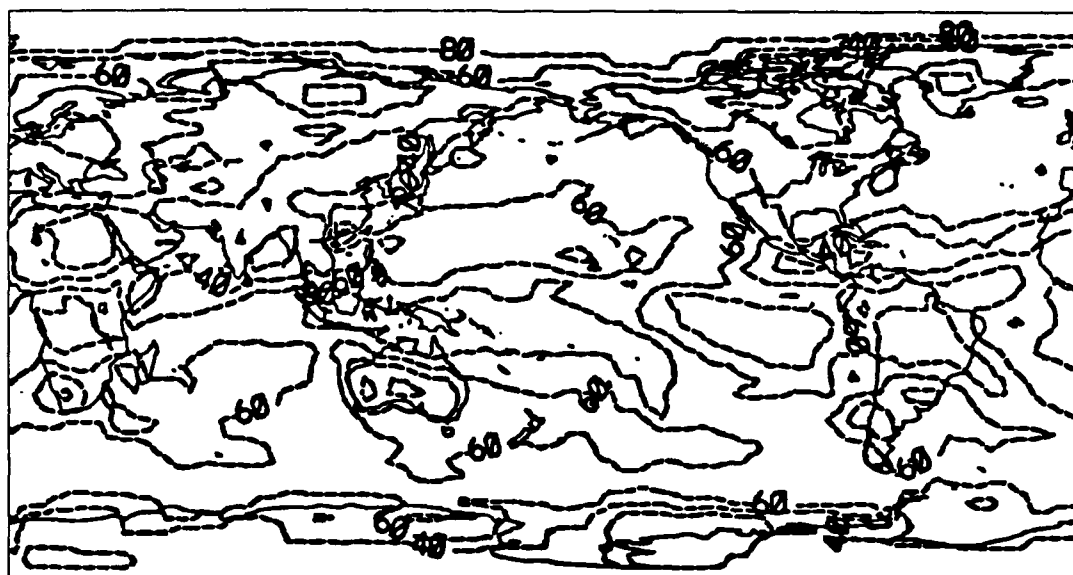


Fig 2.8 January monthly average total cloud amount (%). Model 3DNEPH (top) versus HS 3DNEPH (bottom). Contour interval for the top is 10%, and is as shown for the bottom.

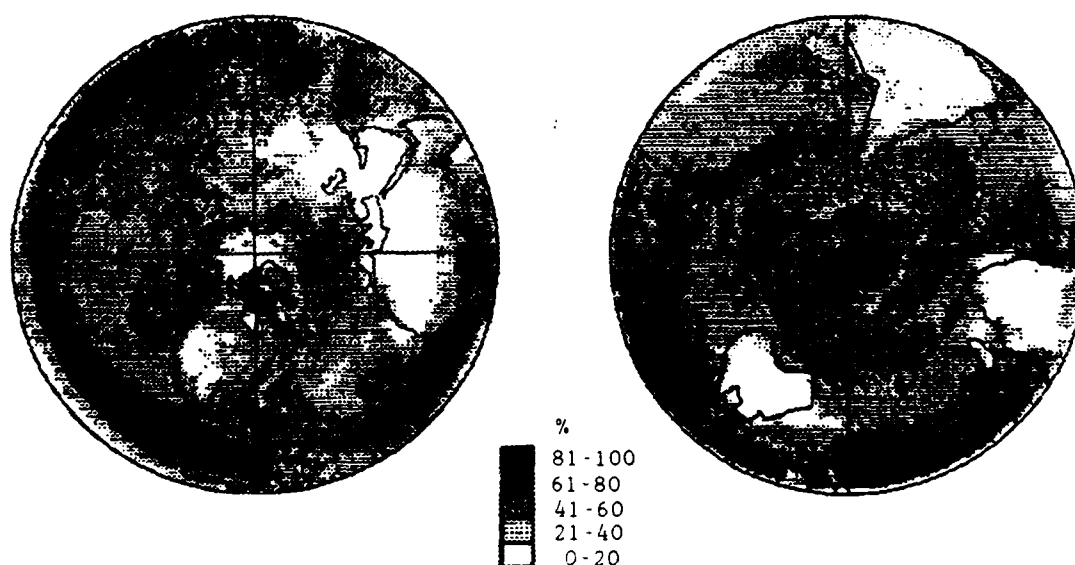
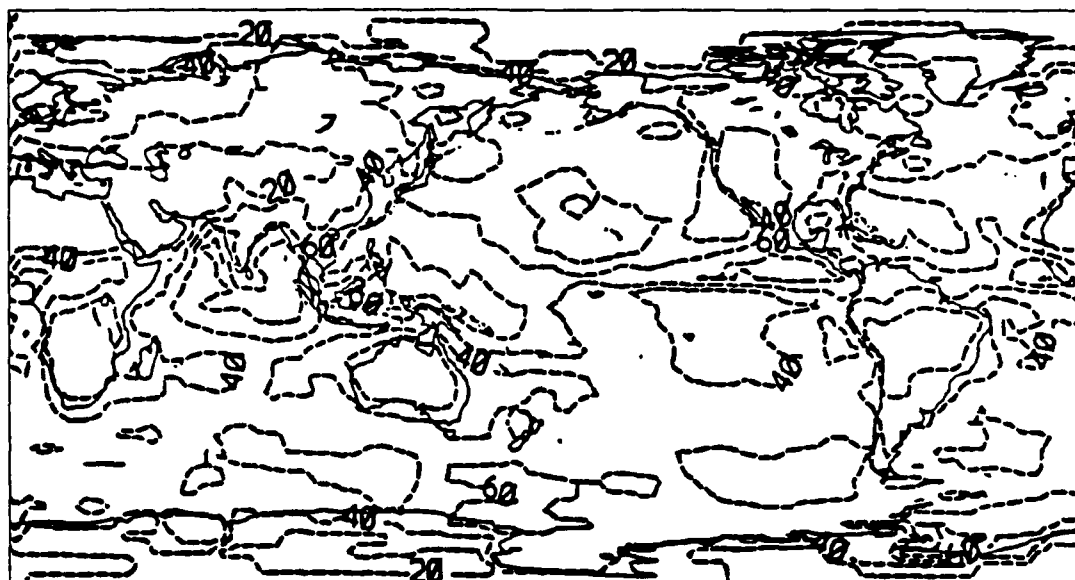


Fig 2.9 July monthly average low cloud amount (%). Model 3DNEPH (top) versus HS 3DNEPH (bottom). Contour interval for the top is 20%, and is as shown for the bottom.

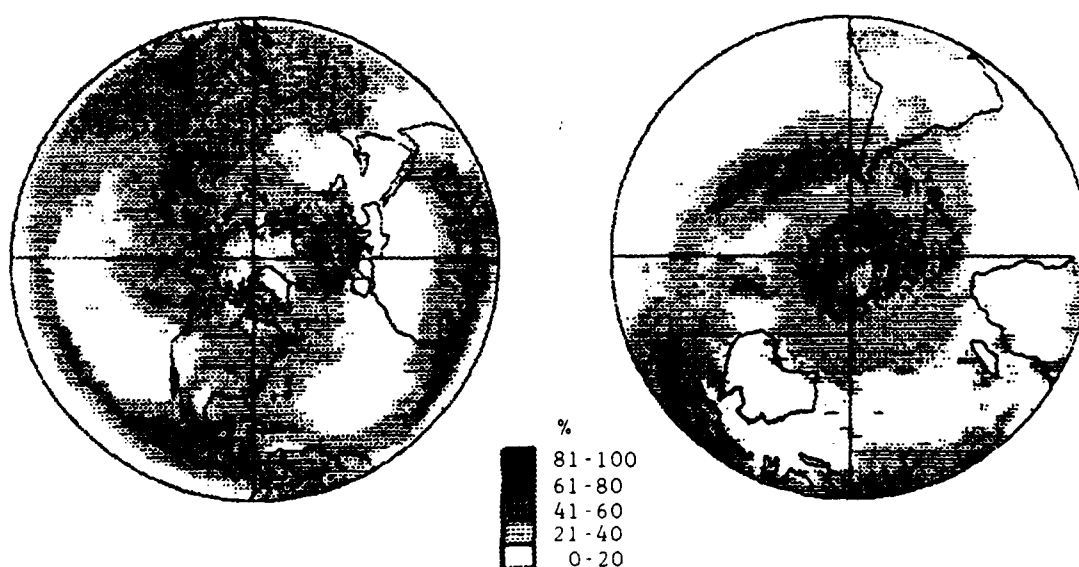
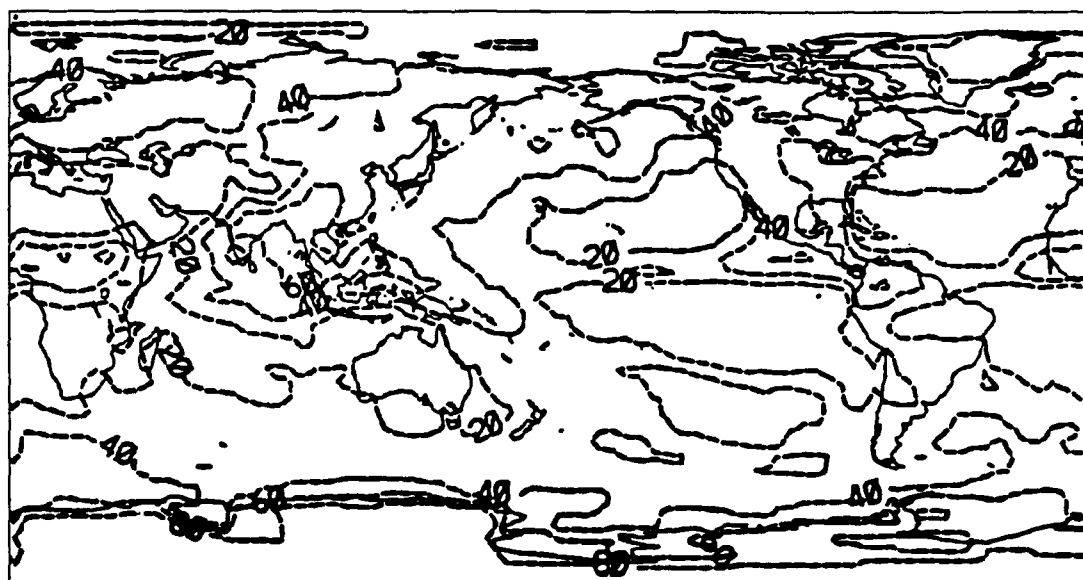


Fig 2.10 July monthly average middle cloud amount (%). Model 3DNEPH (top) versus HS 3DNEPH (bottom). Contour interval for the top is 20%, and is as shown for the bottom.

displays 20% middle clouds while HS displays 0 to 20% middle clouds. Over South America, the model has 20 to 60% middle clouds while HS has 0 to 60% middle clouds. As with the low cloud comparison, the model's and HS' middle cloud results compare very well. Next, let us continue the comparison by moving up another layer.

Figure 2.11 shows a comparison between the model (top) and HS (bottom) July 1979 high cloud averages. Over the United States, the model has 0 to 20% high clouds while HS has 0 to 40% high clouds. In Central America, the model has 10 to 20% high clouds while HS has 0 to 40% high clouds. Over Southeast Asia, the model displays 10 to 20% high clouds while HS displays 20 to 40% high clouds. Again, as with the other layers of the comparison, within the resolution of the contours, the model's and HS' high cloud results compared very well. Now, we will finish the comparison of the clouds by looking at the total cloud amounts for July 1979.

Figure 2.12 is a comparison between the model (top) and HS (bottom) July 1979 total cloud average. Starting in North Africa and the Middle East, the model's total cloud average ranges from 0 to more than 20% while HS total cloud average is 0 to 20%. Over Australia, the model shows 40 to 60% total cloud coverage while HS has 0 to 60%. Over South America, the model has 20 to 60% total cloud coverage while HS displays 0 to 60%. For July 1979 the biggest difference is in the high cloud comparison, which is also reflected in the total cloud amounts. The difference is due, at least in part, to the way the two studies determine middle and high clouds. The model uses the -20°C isotherm as the middle-high cloud boundary. The -20°C isotherm is

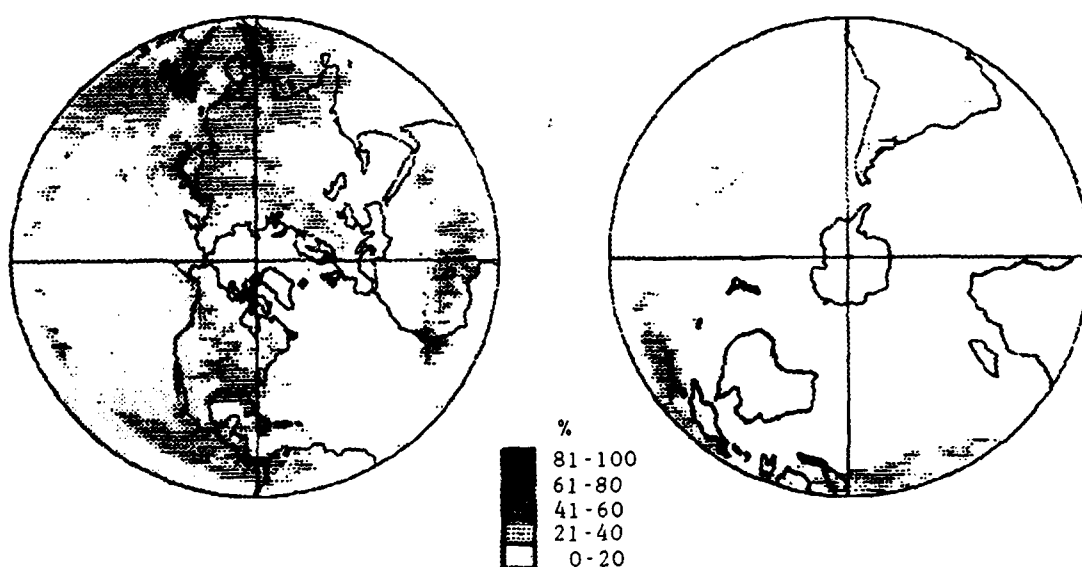
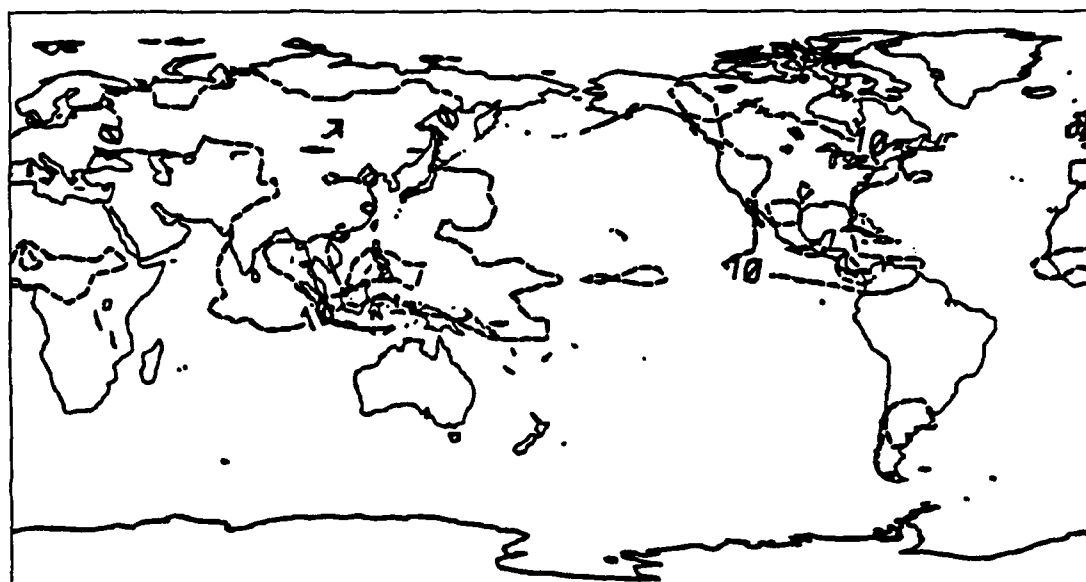


Fig 2.11 July monthly average high cloud amount (%). Model 3DNEPH (top) versus HS 3DNEPH (bottom). Contour interval for the top is 10%, and is as shown for the bottom.

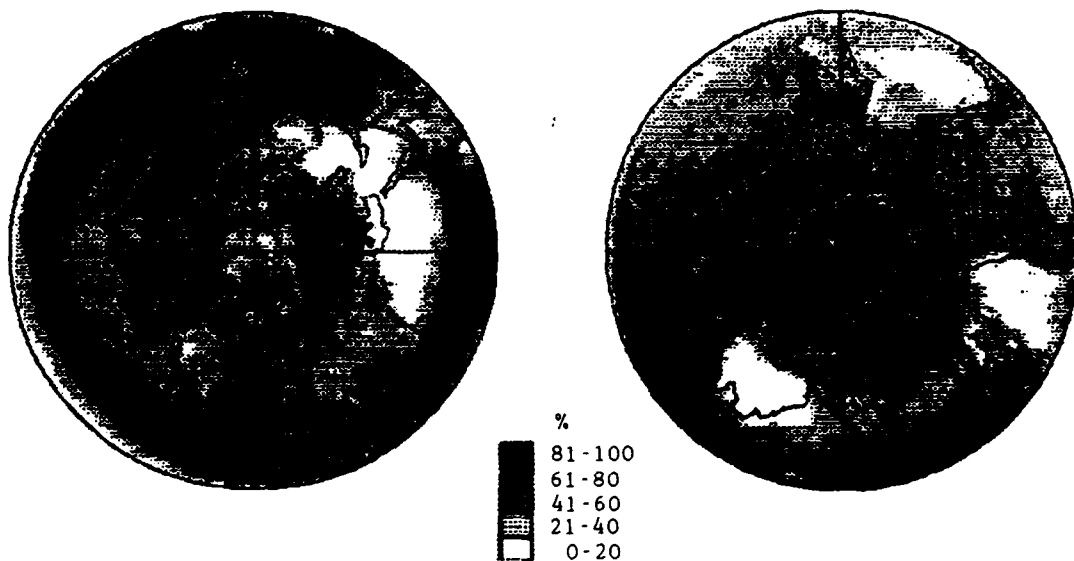
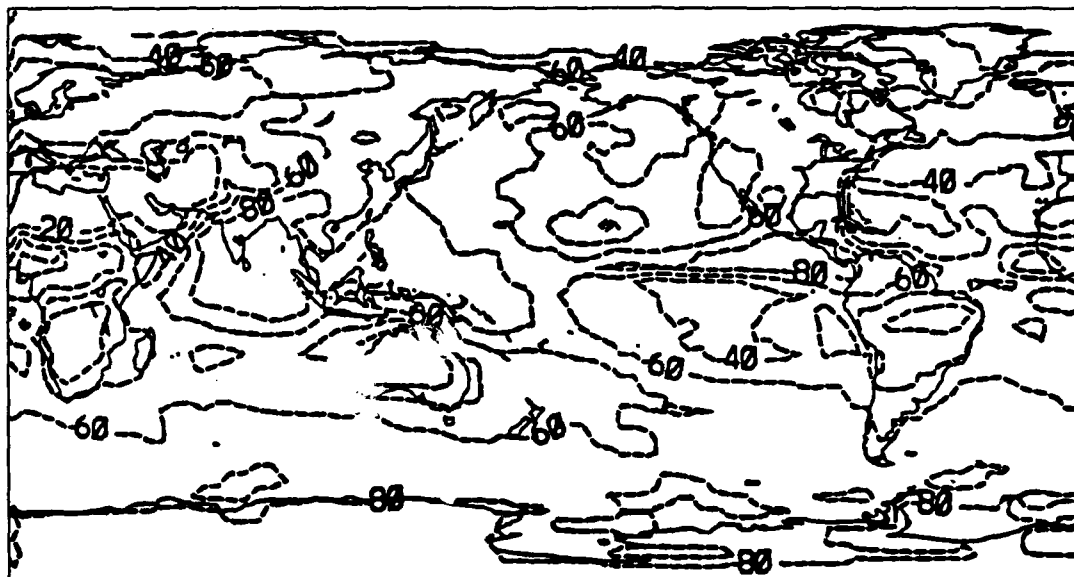
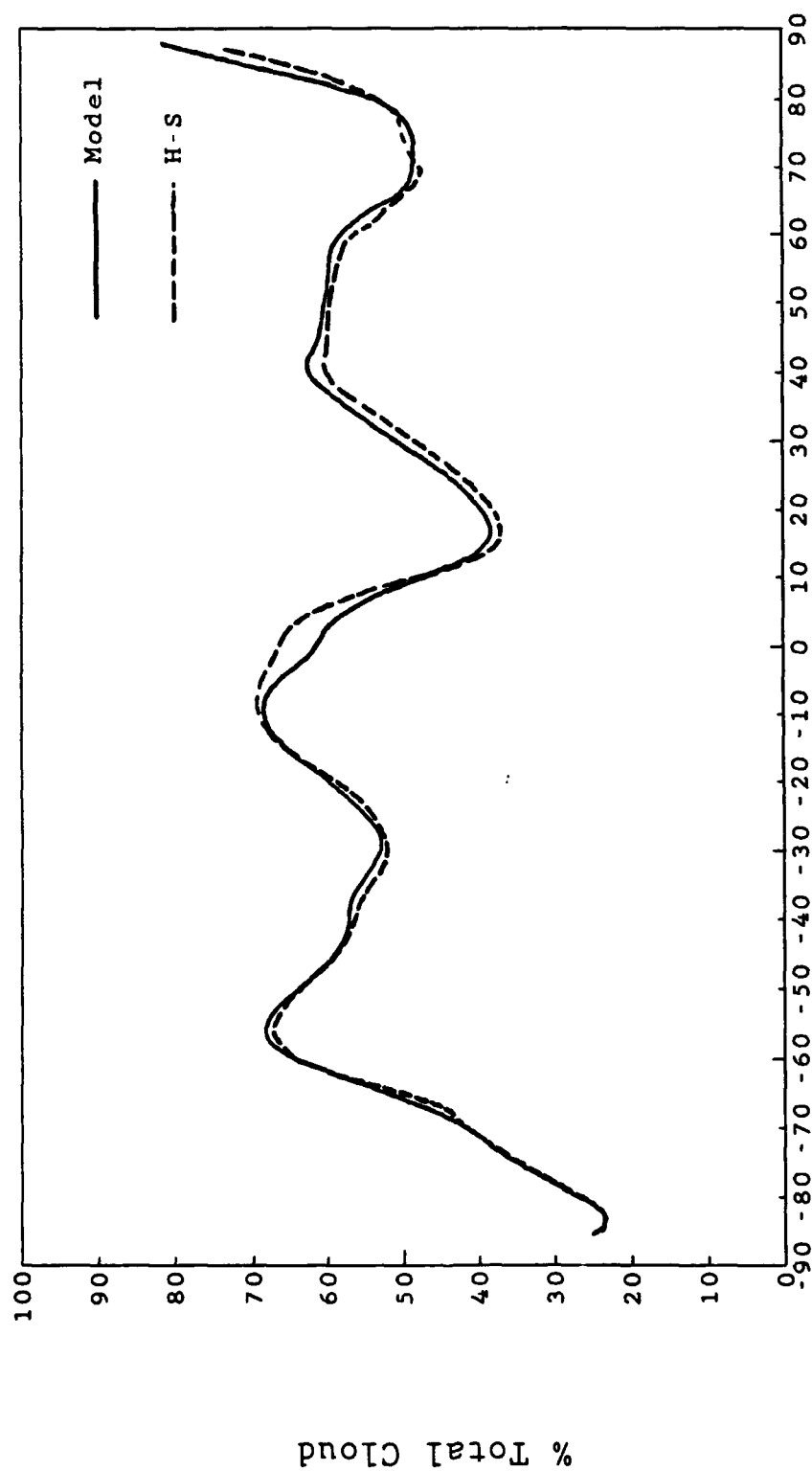


Fig 2.12 July monthly average total cloud amount (%), Model 3DNEPH (top) versus HS 3DNEPH (bottom). Contour interval for the top is 20%, and is as shown for the bottom.

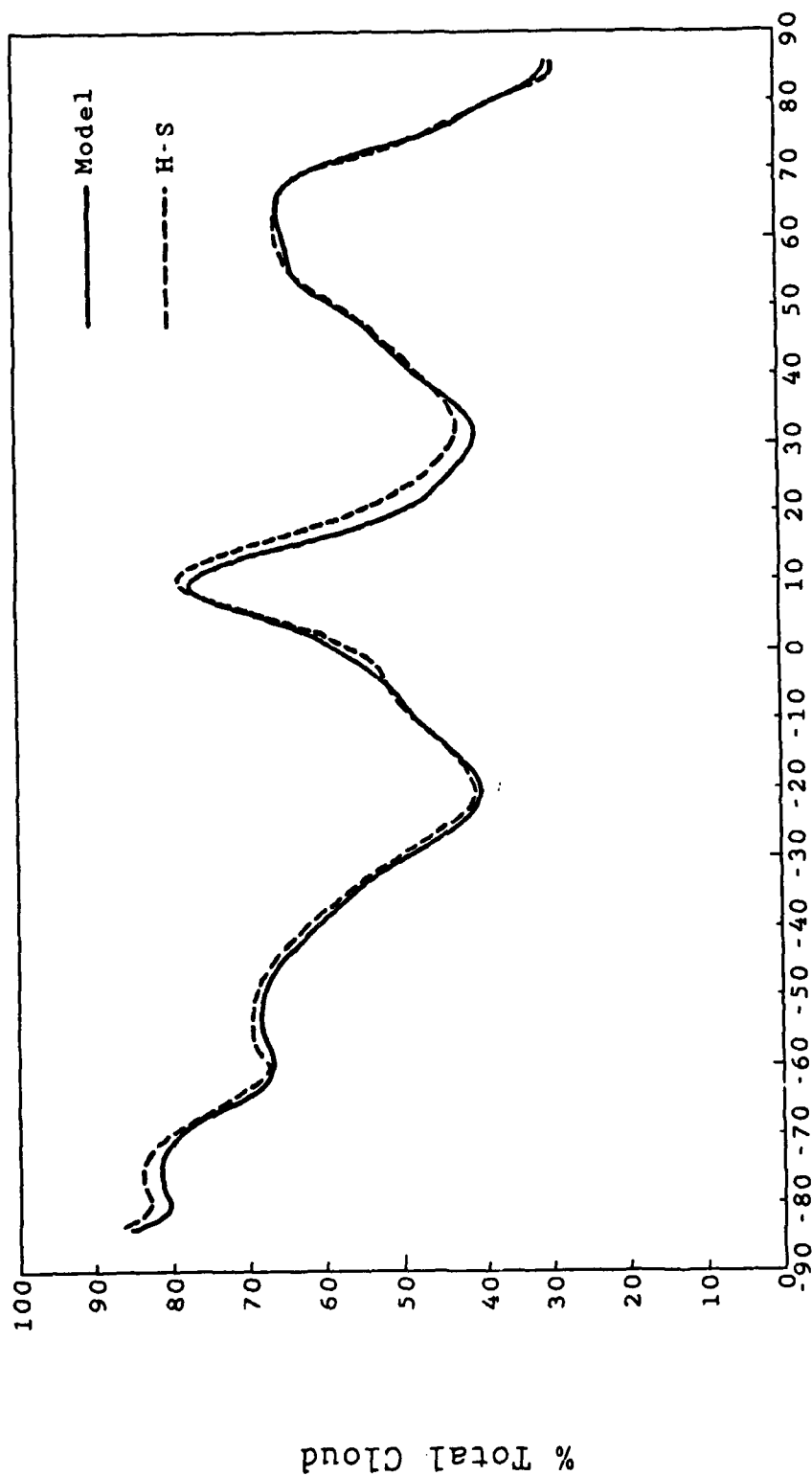
approximately 2.5 km at the poles to over 9.0 km at the equator. HS used a height of 6.0 km as the middle-high cloud boundary. Thus, from 30°S to 30°N latitude, clouds that would be middle clouds in the model are high clouds in HS.

Figures 2.13 and 2.14 depict a comparison between the model's and HS' zonal average total cloud climatology for the months of January and July 1979, respectively. Both figures show good agreement with one another. A large difference occurs at the winter poles (January, North Pole; July, South Pole) due to an error in the processing of the IR satellite information. (Visible satellite information does not exist for the polar regions in the winter because of a lack of sunshine.) If the IR satellite greyscale is incorrectly converted to a temperature or the surface-atmosphere information is incorrect, then it is possible that the land surfaces in the polar regions are being interpreted as clouds (Griffin 1987). The January 1977 zonal cloud climatology developed by Gordon et al. (1984), based on the 3DNEPH cloud information, also has extremely high total cloud amounts near the North Pole. The figures show that the maximum total cloud amount in the vicinity of the equator and correlates with the position of the ITCZ. The January and July tropical cloud maxima, associated with the ITCZ (Figure 2.13 and 2.14), are near 10°S and 10°N, respectively, and the July maxima reaches 80% (Figure 2.14). The minimum total cloud amount on either side of the ITCZ is associated with the subtropical high. Proceeding poleward, the next maximum in total clouds is associated with the midlatitude storm tracks. In addition, the amplitude of the maximum



Latitude

Fig 2.13 January 1979 zonal average 3DNEPH total cloud (%). Model versus HS.



Latitude

Fig 2.14 July 1979 zonal average 3DNEPH total cloud (%). Model versus HS.

increases significantly and is well documented by other cloud climatologies (Henderson-Sellers, 1985). In July, the midlatitude storm tracks move northward in both hemispheres. The northern midlatitude cloud cover maxima shifts from approximately 35° to 65°N and becomes better defined (sharper). The southern cloud cover maxima shifts from approximately 58° to 50°S and becomes less well-defined (less sharp). Unlike the winter polar region, the cloud cover over the summer polar region is more realistic than over the winter polar region.

Overall, the favorable results of the comparisons validate the model's cloud data base use in this research.

CHAPTER 3

MODEL SENSITIVITY TESTS

To ensure accurate model results, modification must be made to the radiative transfer models input parameters before the model can be run to produce TOA and surface radiation budgets, as well as the cloud forcing experiments. The primary adjustment involves choosing an appropriate cloud overlap scheme for the model, which in turn determines the cloud amount that the radiative transfer model uses. The earth radiation budget (ERB) dataset was used in this study to tune the model cloud overlap scheme.

3.1 ERB Data Base

The archive used to compare and tune the radiative transfer model's results was originally developed for use in cloud/radiation studies at the University of Utah (Koenig, 1985; Koenig et al., 1987) and required considerable amount of effort and time by Koenig and Griffin to develop and execute the methodology for producing a global radiative climatology. Griffin (1987) obtained and processed ERB data for the months of January and July 1979 to produce zonally averaged infrared (IR) and solar flux values. Since a detailed discussion of the ERB data base was included in the previous work, only a brief description will be given in this chapter.

The exact boundaries for the 2070 equal area ERB Target Areas (TAs) are displayed on a Mercator projection on Figure 3.1. Each TA

is approximately $500 \times 500 \text{ km}^2$ and is bounded by latitude and longitude lines. The TAs are numbered from 1 (South Pole) to 2070 (North Pole) in a westerly fashion. Each TA is further subdivided into nine (3×3) Subtarget Areas (STAs). Each STA has dimensions of $160 \times 160 \text{ km}^2$.

The ERB IR and solar flux values, used for comparing the model's results, were obtained from Griffin (1987). Figure 3.2 (Griffin, 1987) shows that Griffin's daily averaged ERB net flux compares very well with published values from the NFOV (narrow-field-of-view) and WFOV (wide-field-of-view) radiometers. As can be seen, the quality of the results validates their use for comparison purposes.

3.2 Radiative Transfer Parameterizations

In this study, the model that was used was developed by Ou and Liou (1987). The model was based on the principle of the broadband model approximation to the radiative transfer approximation. For the parameterization of the radiative properties of clouds, the model is based on the results from the work by Liou and Wittman (1979). The model was originally developed to be a computationally economical and accurate radiation program for incorporation into the global models developed at the Geophysics Laboratory (GL). The program was specifically developed for applications to atmospheres containing high, middle, and low clouds and combinations thereof. The model had originally been designed to use its own cloud formation schemes for general circulation models in connection with the radiation program. The model has been modified to use the 3DNEPH cloud climatology, discussed in Chapter 2. The program has been modified to run on a

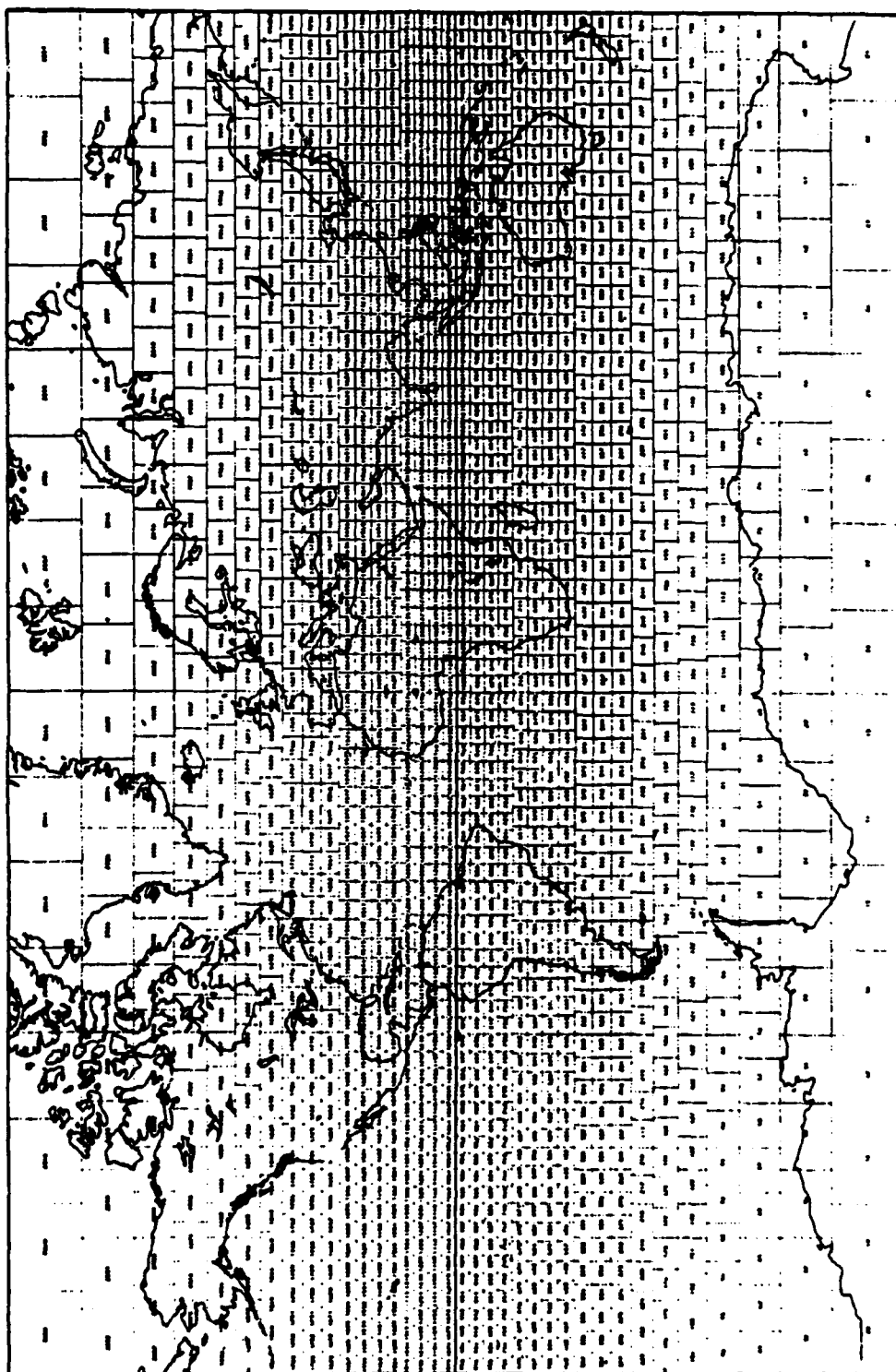


Fig 3.1 Global Nimbus 7 ERB grid target areas.

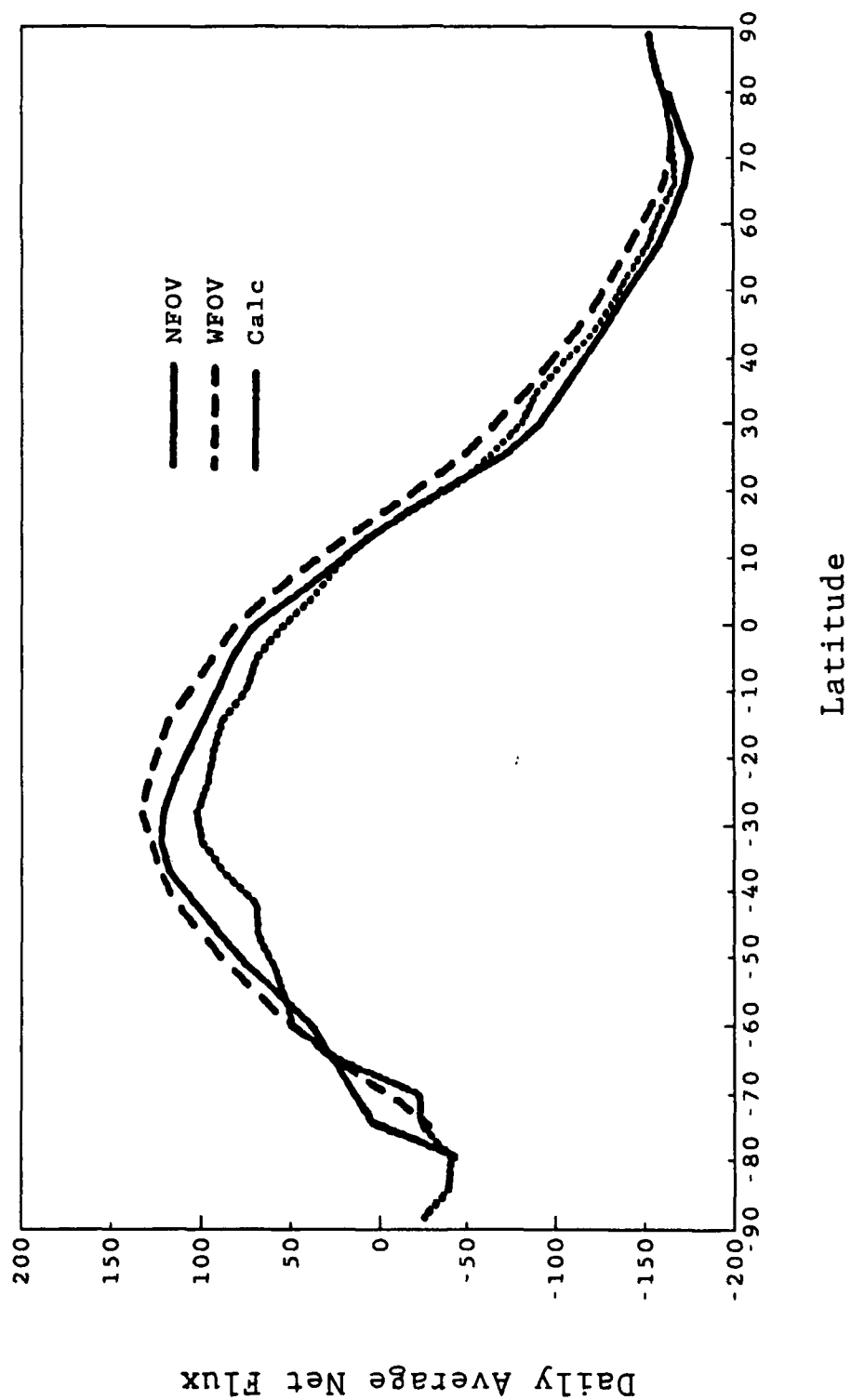


Fig 3.2 Computed zonal averages of the daily average NFOV net flux (---) plotted against published values from the NFOV (—) and WFOV (···) radiometers for January 1979.

global 19 layer atmospheric model that utilizes the same grid as the ERB dataset. In order to cut down the computation time required to obtain the monthly average values of flux for January and July, all the model input parameters have been put into an ERB (TA) grid system and averaged over the months of interest. The model was then run using these monthly values and returned the monthly averaged values of solar and IR flux at TOA and at the surface. Also, the model determines the monthly averaged heating rates.

3.3 Cloud Overlap Adjustments

The radiation model was run initially using the total cloud amount as determined by using the scheme developed by Griffin (1987). TOA outgoing radiation results were zonally averaged and correlated to the ERB data archive. The correlation was good, except in the ITCZ region (see Figures 2.13 and 2.14), the location of which is determined by the region of maximum total cloud amount close to the equator. In this region, the high convective cloud amount caused the model results to be too low for both solar and IR radiative fluxes. The absolute difference is greater between the model's and the ERB's TOA zonally averaged solar flux than between the model's and the ERB's TOA zonally averaged IR flux. This is due to the solar flux being four times more sensitive to changes in cloud amount than the IR flux (Koenig 1987). In addition, the model does not handle convective clouds well. In this region, an average overlap scheme was used as follows:

$$CTA = (C_L + C_M + C_H)/N. \quad (3.1)$$

where CTA is the average total cloud amount, C_L is the amount of low

clouds. C_M is the amount of middle clouds. C_H is the amount of high clouds. and N is the number of different cloud layer types. This average cloud overlap scheme reduces the CTA (as compared to Griffin's (1987) total cloud overlap scheme) that the radiative transfer model uses. Thus, it increases the amount of model-produced TOA solar and IR flux. This allows the model to better interpret convective clouds. Griffin's (1987) total overlap scheme was used over the rest of the globe, where there were fewer convective clouds.

3.4 Comparison of Model and ERB Results

Figures 3.3 and 3.4 depict the comparison between the model (top) and ERB (bottom) of the January 1979 global TOA net solar and IR fluxes, respectively. The January solar flux comparison (Figure 3.3) shows that the results of the adjustments are very good. The ERB (bottom) results for the Northern Hemisphere being more zonal (North Pole to $10^{\circ}N$) as compared to the model (top, North Pole to $20^{\circ}N$). The net solar flux values from $20^{\circ}N$ poleward are in very good agreement, with the values being 160 W/m^2 ($20^{\circ}N$) and decreasing poleward to 0 W/m^2 . The zonal pattern in the Northern (winter) Hemisphere is expected due to a decrease in surface and lower atmospheric temperatures and a decrease in convective activity. The low flux values are due to a lack of solar radiation present in the winter hemisphere. This is also the cause of the aforementioned changes in temperature and low convective activity. From about $15^{\circ}N$ southward both maps start to show more and more features due to more and more heating of the earth's surface and atmosphere. The maximum value ($\approx 360 \text{ W/m}^2$) occurs at the southern subtropical high (Figure 2.13)

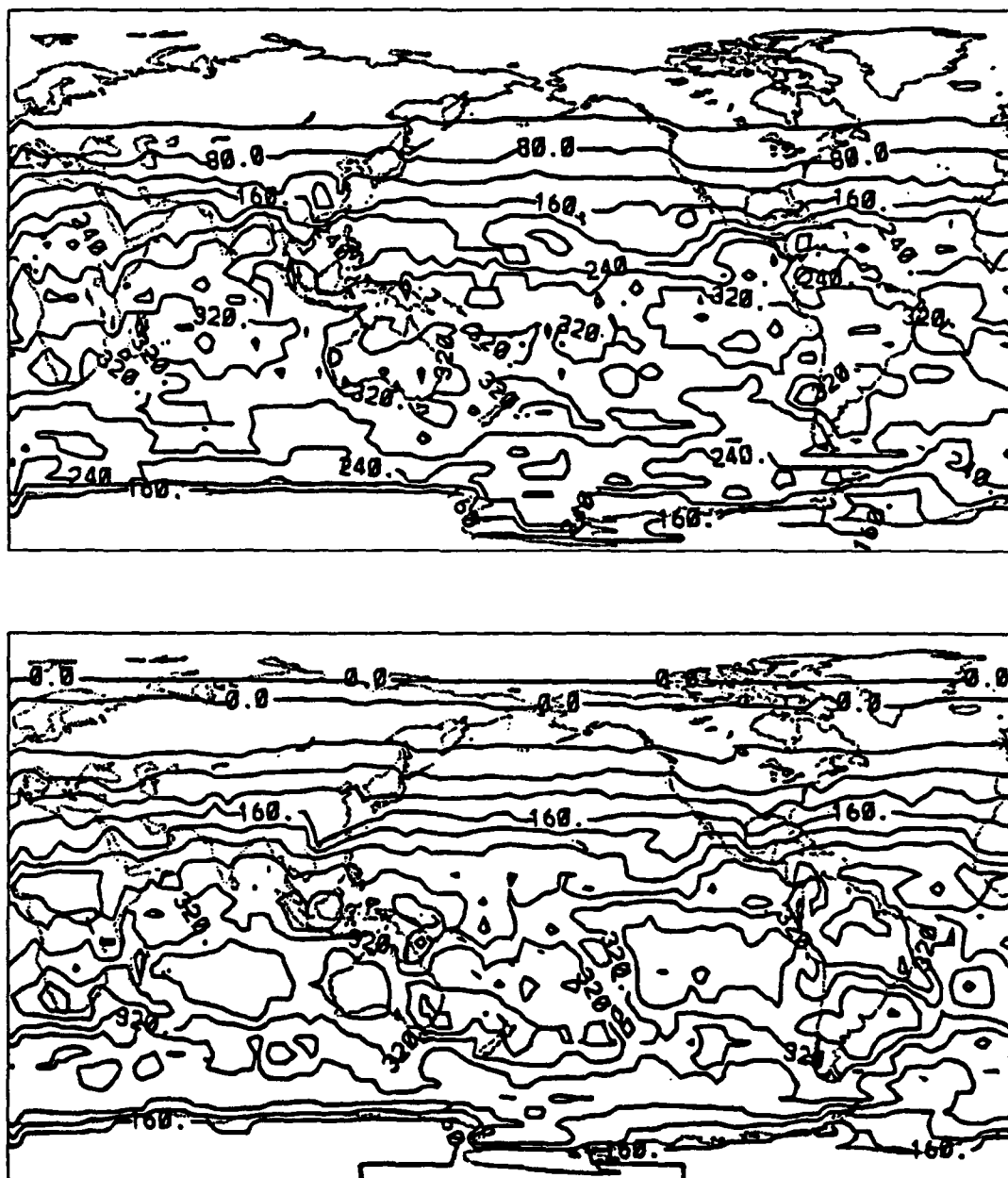


Fig 3.3 January 1979. Model (top) versus ERB (bottom), global net downward TOA solar flux (W/m^2). Contour interval is 40 W/m^2 .

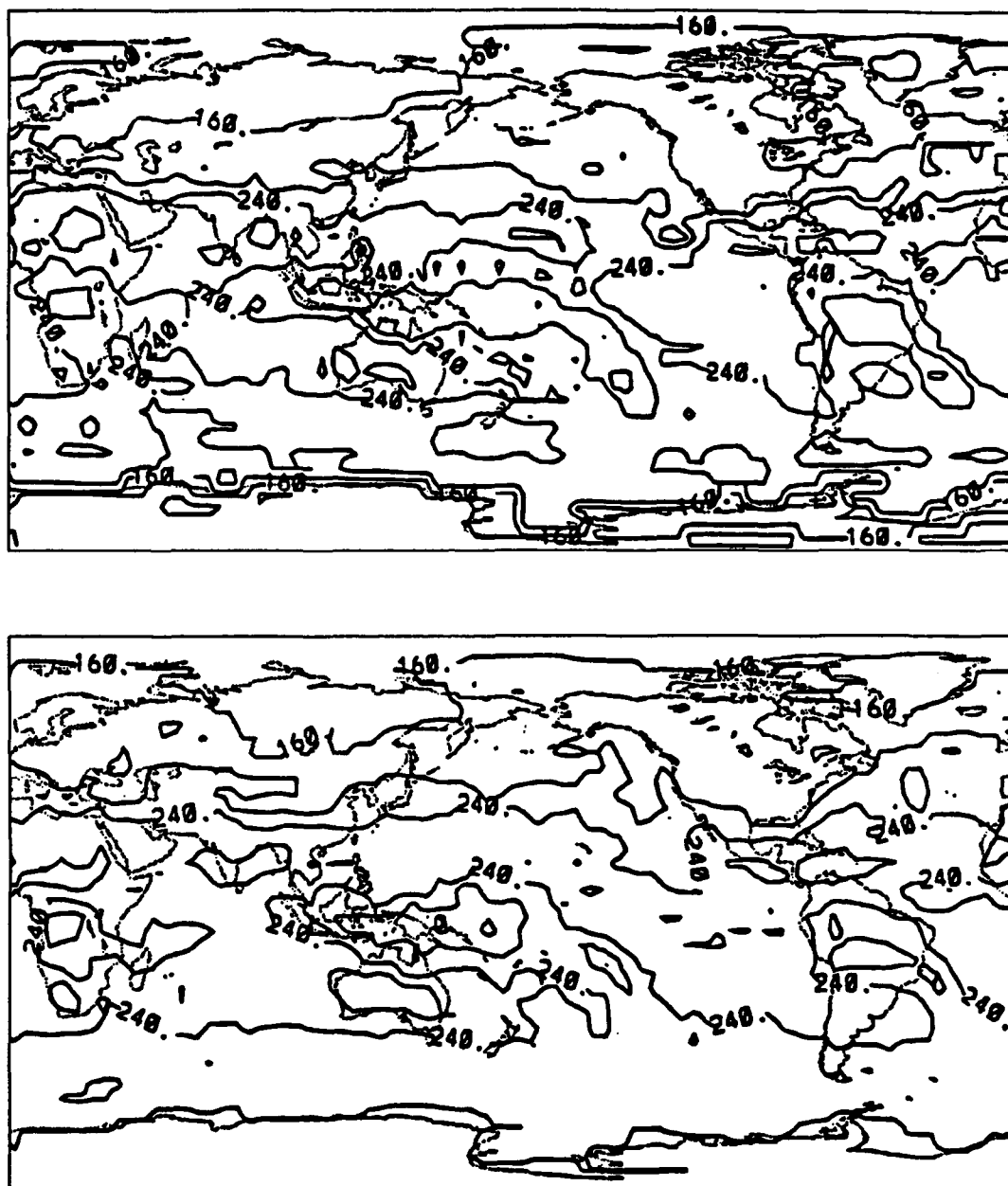


Fig 3.4 January 1979, Model (top) versus ERB (bottom), global outgoing TOA IR flux (W/m^2). Contour interval is 40 W/m^2 .

where there are few clouds and the sun's heating is the most intense. The model is about 25 to 30 W/m^2 lower, and this can be partially explained by the model's difficulty in handling convective clouds in the present mode. Once the total cloud amount has been determined, the model uses that amount for all cloud layers. For example, if the amounts of low, middle, and high clouds are 80%, 20%, and 10%, respectively, the model assumes the cloud cover to be 80% for all layers. This is done to reduce the computational complexity. Thus the amount of clouds is overestimated, with the result being an underestimation of the solar flux. Also, the 3DNEPH cloud climatology seems to have overestimated the amount of cloud cover in the southern subtropical high, the results of which are an underestimation of the solar flux at TOA. From the southern subtropical high, the values decrease poleward to a value of $\approx 160 \text{ W/m}^2$ for both model and ERB results. The value of the flux in the southeast Asia and Indonesia area is on the order of 280 W/m^2 .

For the January IR flux (Figure 3.4) the overall pattern is much the same. Starting in North America, the flux is $\approx 160 \text{ W/m}^2$ for both the model and ERB results. In South America and Australia, the flux is from 200 to 240 W/m^2 . Over the Eurasian continent, the flux is from 160 to 240 W/m^2 . For Antarctica, the flux for the model is from 160 to 200 W/m^2 , while the flux for the ERB are $\approx 180 \text{ W/m}^2$.

Figures 3.5 and 3.6 depict a comparison of the model (top) to the ERB (bottom) of the July 1979 global net solar and IR flux at TOA, respectively. As shown in Figures 3.3 (January) and 3.5 (July), the solar flux is very zonal in the winter hemisphere. Starting at 20°S

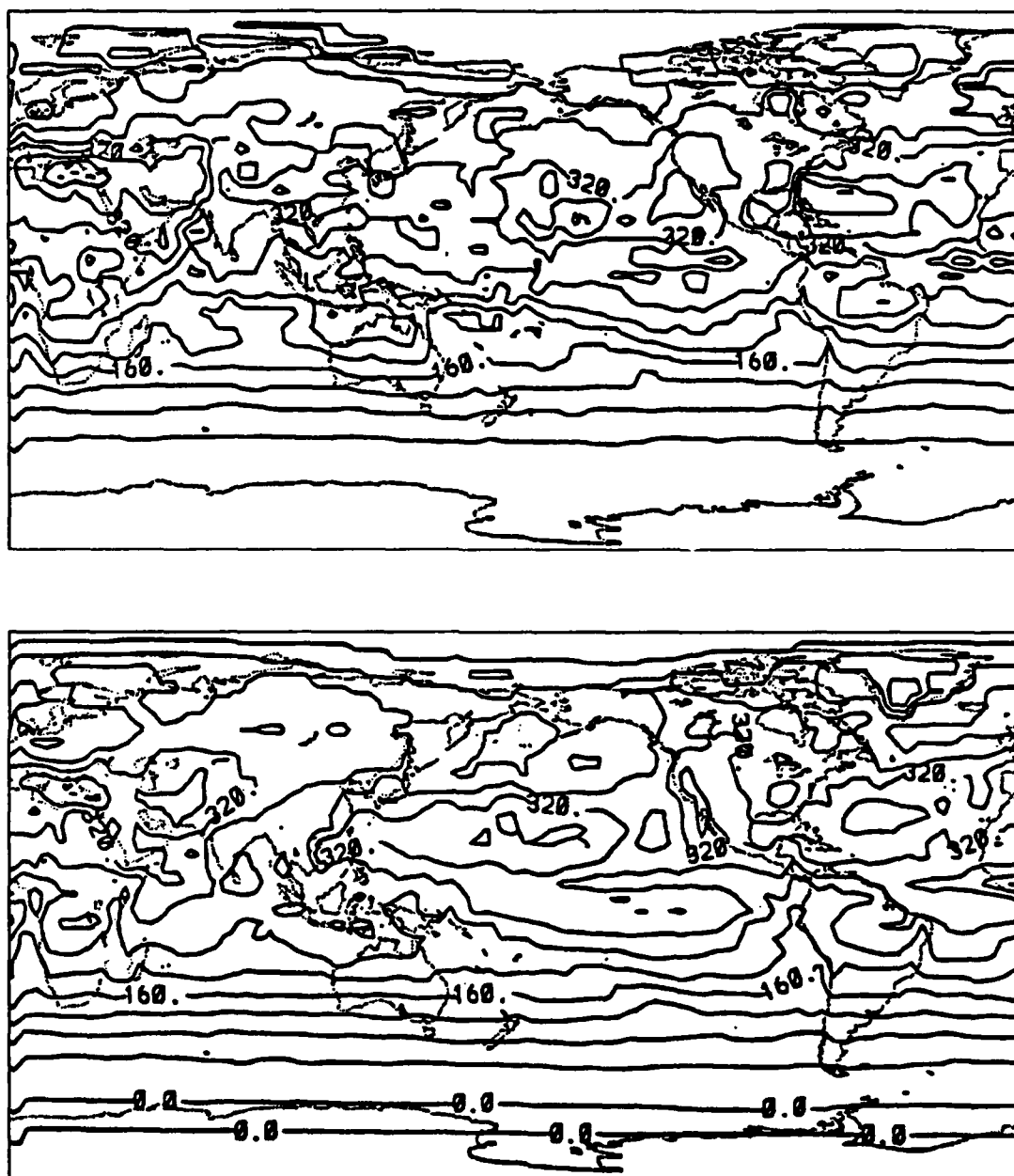


Fig 3.5 July 1979, Model (top) versus ERB (bottom), global net downward TOA solar flux (W/m^2). Contour interval is 40 W/m^2 .

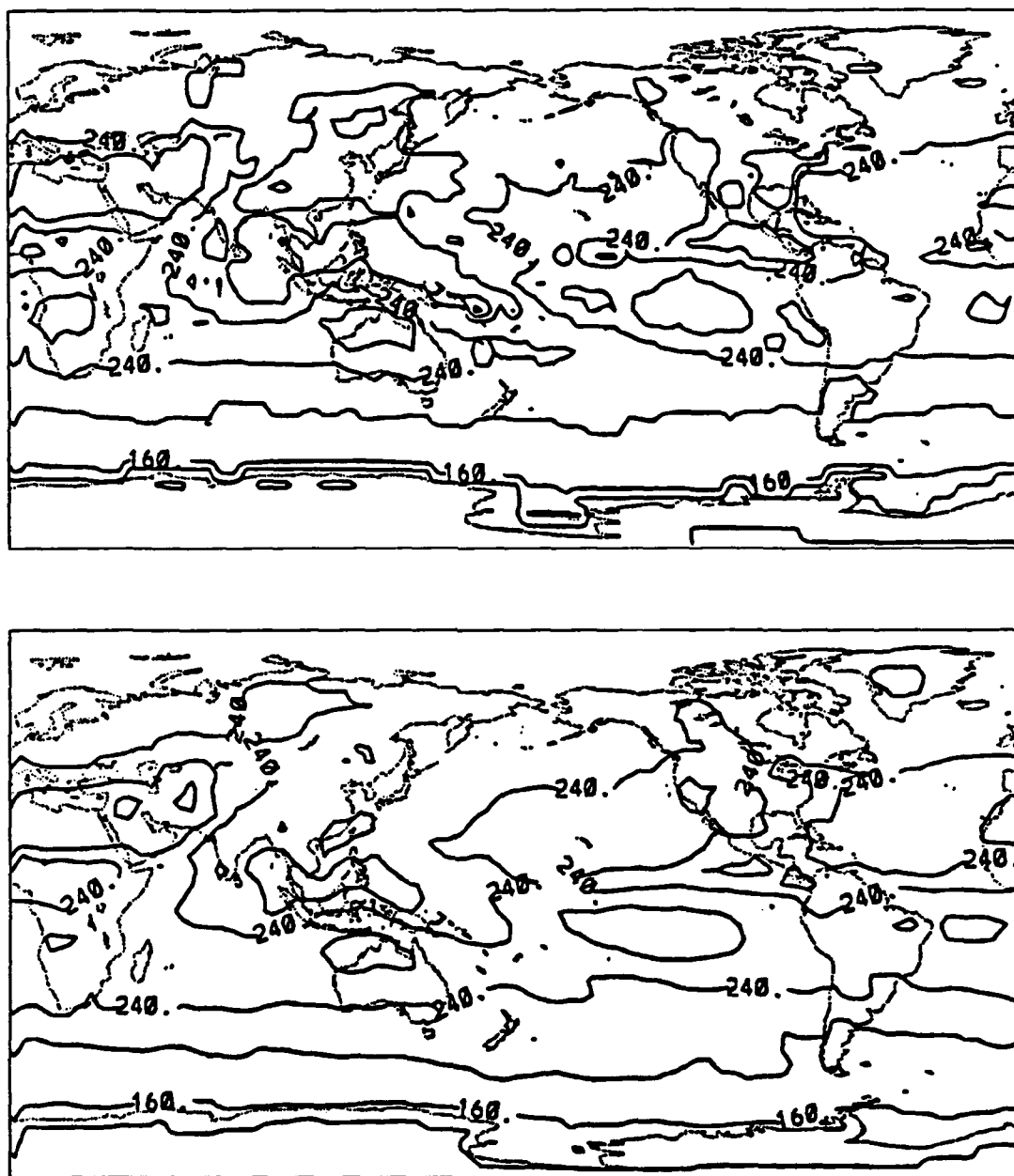


Fig 3.6 July 1979. Model (top) versus ERB (bottom), global outgoing TOA IR flux (W/m^2). Contour interval is 40 W/m^2 .

latitude, the solar flux values decrease poleward (South Pole) from 160 to 0 W/m^2 for both the model and ERB (Figure 3.5). Next, the maximum values of the solar flux occur in the area of the northern subtropical high ($\approx 30^\circ\text{N}$) where the cloud amounts are low, and are from 320 to 360 W/m^2 . Over the Eurasian and North American continents, the flux is from 280 to 320 W/m^2 . In the North Pole region, the flux is from 200 to 240 W/m^2 . Finally, in the vicinity of the ITCZ (see Figure 2.14), the solar flux decreases $\approx 40 \text{ W/m}^2$ because of the increased cloud cover.

For the July IR TOA flux values (Figure 3.6), there is a zonal decrease in the Southern Hemisphere, between about 30°S to the South Pole, from 240 to 120 W/m^2 for both the model and ERB. At the southern subtropical high, the IR flux is from 240 to 280 W/m^2 because of a lack of cloud cover. Just the opposite occurs along the ITCZ, where the values drop to $\approx 200 \text{ W/m}^2$, due to the increased cloud cover (see Figure 2.14). Like the southern subtropical high, the flux for the northern subtropical high is from 240 to 280 W/m^2 . The reason for the high values in the area of the subtropical high is a lack of cloud cover.

Figure 3.7 displays the differences between the model and ERB results of the January 1979 global net solar flux at TOA. This figure shows how closely the model results match with the ERB results. In the Northern Hemisphere, the difference between the two is near 0 W/m^2 . In the Southern Hemisphere there are areas where the model overestimates the solar flux values. According to the January cloud climatology, these are areas of deep convective cells. In general,

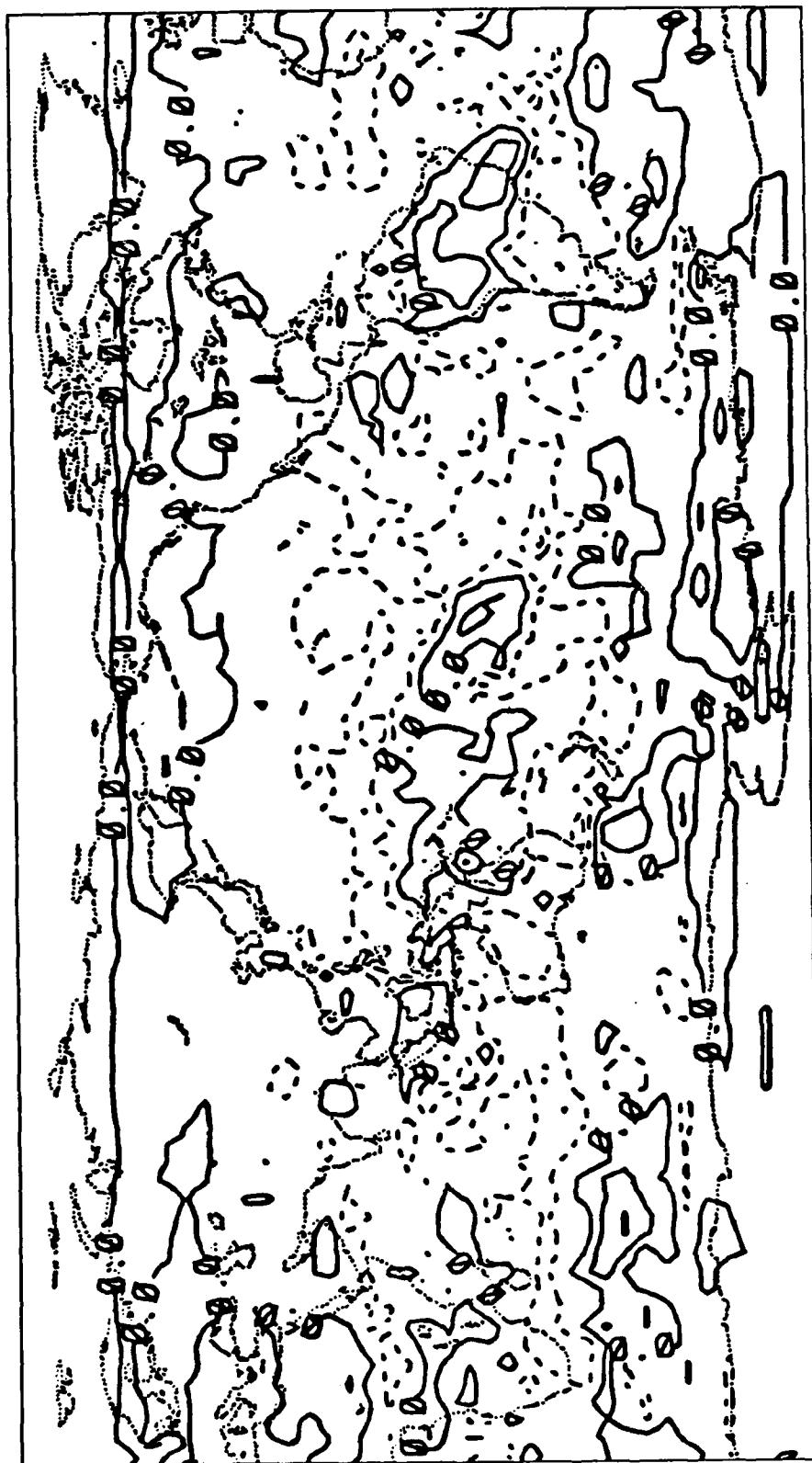


Fig 3.7 January 1979. Model - ERB, global net downward TOA solar flux (W/m^2). Contour interval is 40 W/m^2 .

the model is very sensitive to cloud amounts. We made a serious attempt to counteract this by manipulating the cloud overlap schemes (Section 3.3). As a result, the model still overestimates the cloud cover and underestimates the solar flux amounts, but by a lesser amount. This is the reason for the negative areas shown in Figure 3.7. Figure 3.8 depicts the differences between the model and ERB results of the January 1979 global net flux at TOA. This figure shows that the model results match well with the ERB data. Over most of the globe, the difference is very close to 0 W/m^2 . However, over the North Atlantic the model overestimated the cloud cover, which resulted in an underestimate of the IR flux by 40 W/m^2 .

Figures 3.9 and 3.10 depict the differences between the model and ERB results of the July 1979 global net solar and IR flux at TOA, respectively. For the solar flux, Figure 3.9 shows that from the southern midlatitudes northward, the model generally underestimated the cloud cover, and therefore overestimated the solar flux. The reason for the overestimation of the solar flux in the eastern Pacific and western Atlantic Oceans is fog and low stratus. The model does not handle low clouds and stratus, and this causes the overestimation of the solar flux. Figure 3.10 shows the difference between the model and ERB IR net fluxes at TOA for July 1979. When compared to Figure 3.9, the computed IR flux more closely matches the ERB data than does the solar flux. This is again due to the solar flux being four times more sensitive to the cloud cover amount than the IR flux, as reported by Koenig (1987). Generally, the IR difference contours are zero over most of the globe.

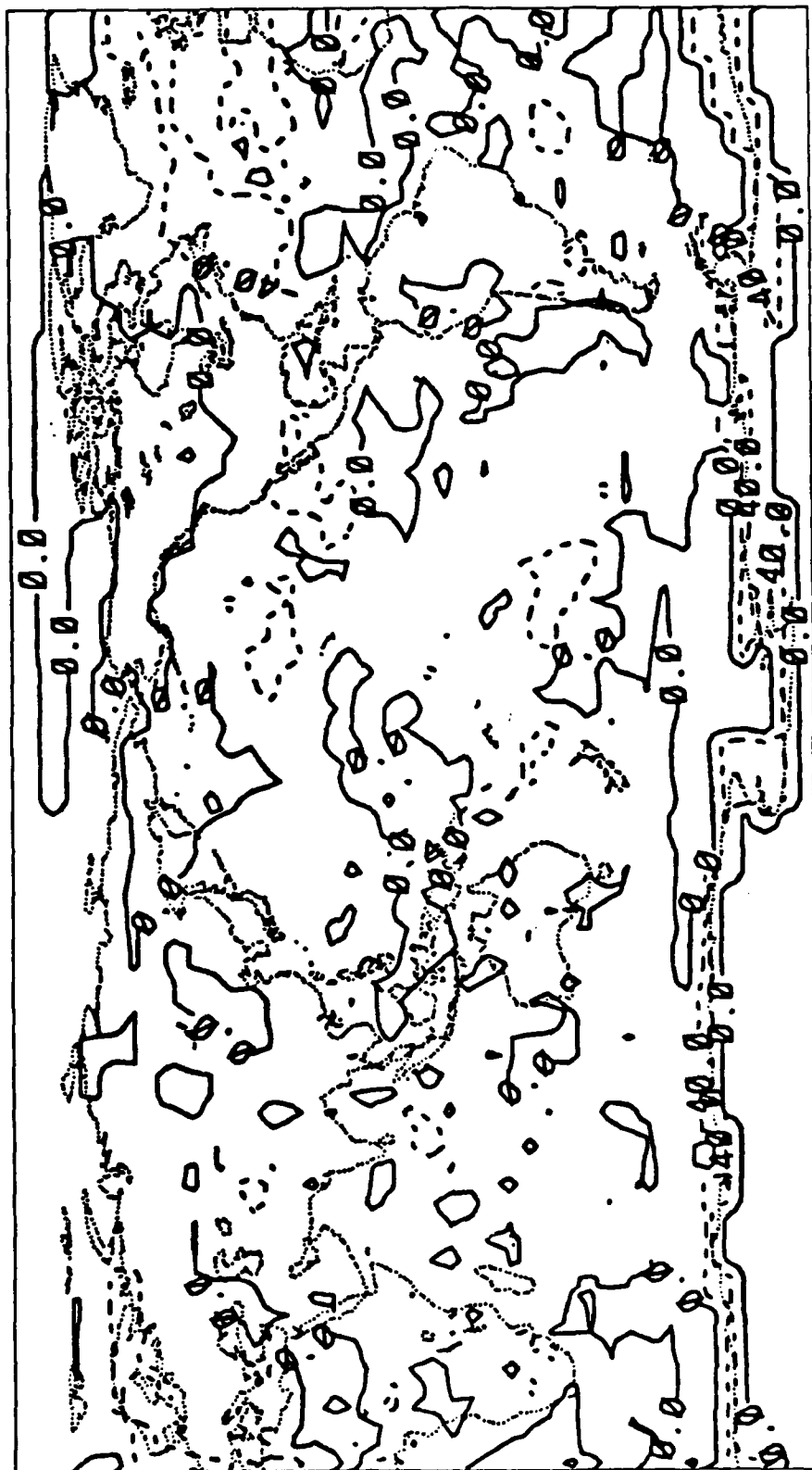


Fig 3.8 January 1979, Model - ERB, global out going TOA IR flux (W/m^2). Contour interval is $40 \text{ W}/\text{m}^2$.

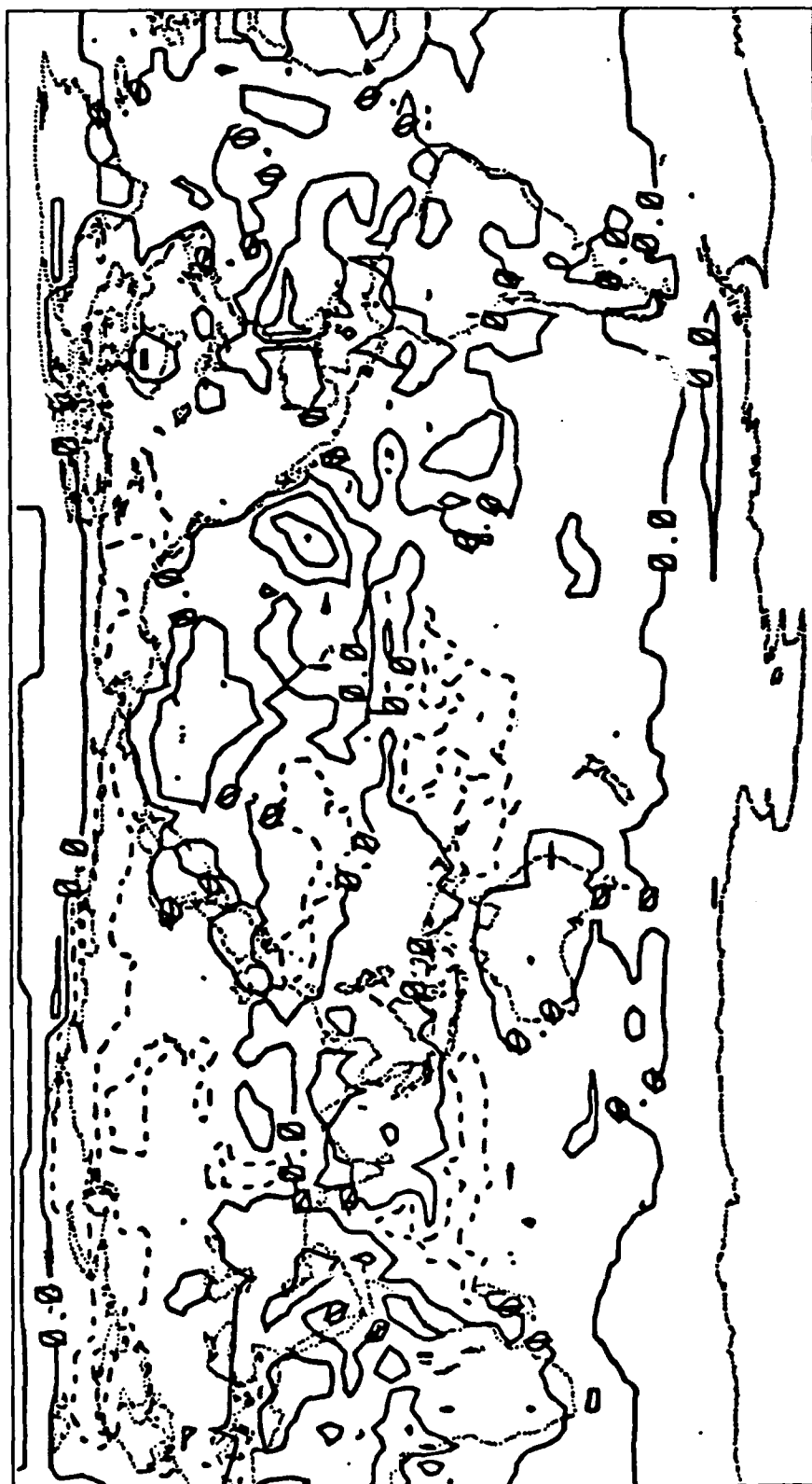


Fig 3.9 July 1979, Model - ERB, global net downward TOA solar flux (W/m²). Contour interval is 40 W/m².



Fig 3.10 July 1979, Model - ERB, global out going TOA IR flux (W/m^2).
Contour interval is 40 W/m^2 .

Figure 3.11 is a comparison of the zonal average solar flux at TOA derived from the model and ERB for January 1979. The comparison is very good except in the region of the northern (15°N) and southern (30°S) subtropical highs. The model overestimates the cloud amount and thereby underestimates the solar flux amount. However, the model results in these regions are still within 30 W/m^2 of the ERB results. The comparison is best at the poles, where the amount of available solar flux is the lowest (within 10 W/m^2). Figure 3.12 is a comparison of the zonal average IR flux at TOA derived from the model and ERB for January 1979. The comparison is very good from pole to pole. The areas of maximum IR flux occur at the northern and southern subtropical highs, where the amount of clouds is the lowest and the solar flux at the surface is the greatest. Hence, these areas will have the highest surface temperatures and therefore the greatest IR flux. The area of minima between the two maxima correlates to the ITCZ region (see Figure 2.13). This is a region of high cloud cover and low amounts of solar flux at the surface. Therefore, the surface temperatures are lower, and this results in lower IR flux. Comparing Figure 3.11 to 3.12 shows that the model for January is generally consistent, with the ERB results higher than the model results for both solar and IR fluxes.

Figure 3.13 is a comparison of the model and ERB results for the July 1979 zonal average solar flux at TOA. Differences between the two results are within 20 W/m^2 . The maximum in the solar flux occurs at approximately 22°N latitude, which corresponds to the total cloud minimum (Figure 2.14) associated with the northern subtropical high.

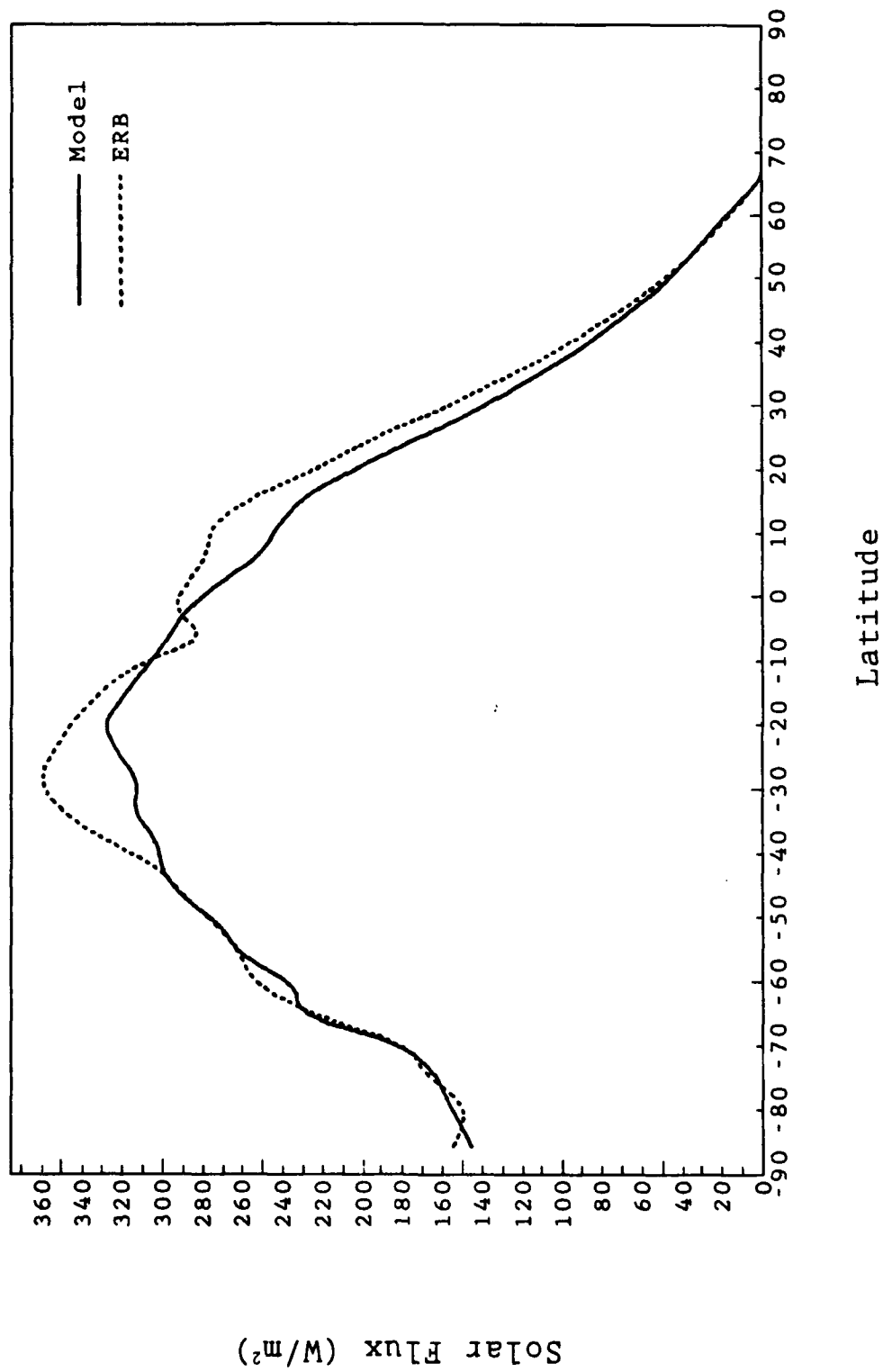


Fig 3.11 January 1979, Model versus ERB, zonal average net downward TOA solar flux.

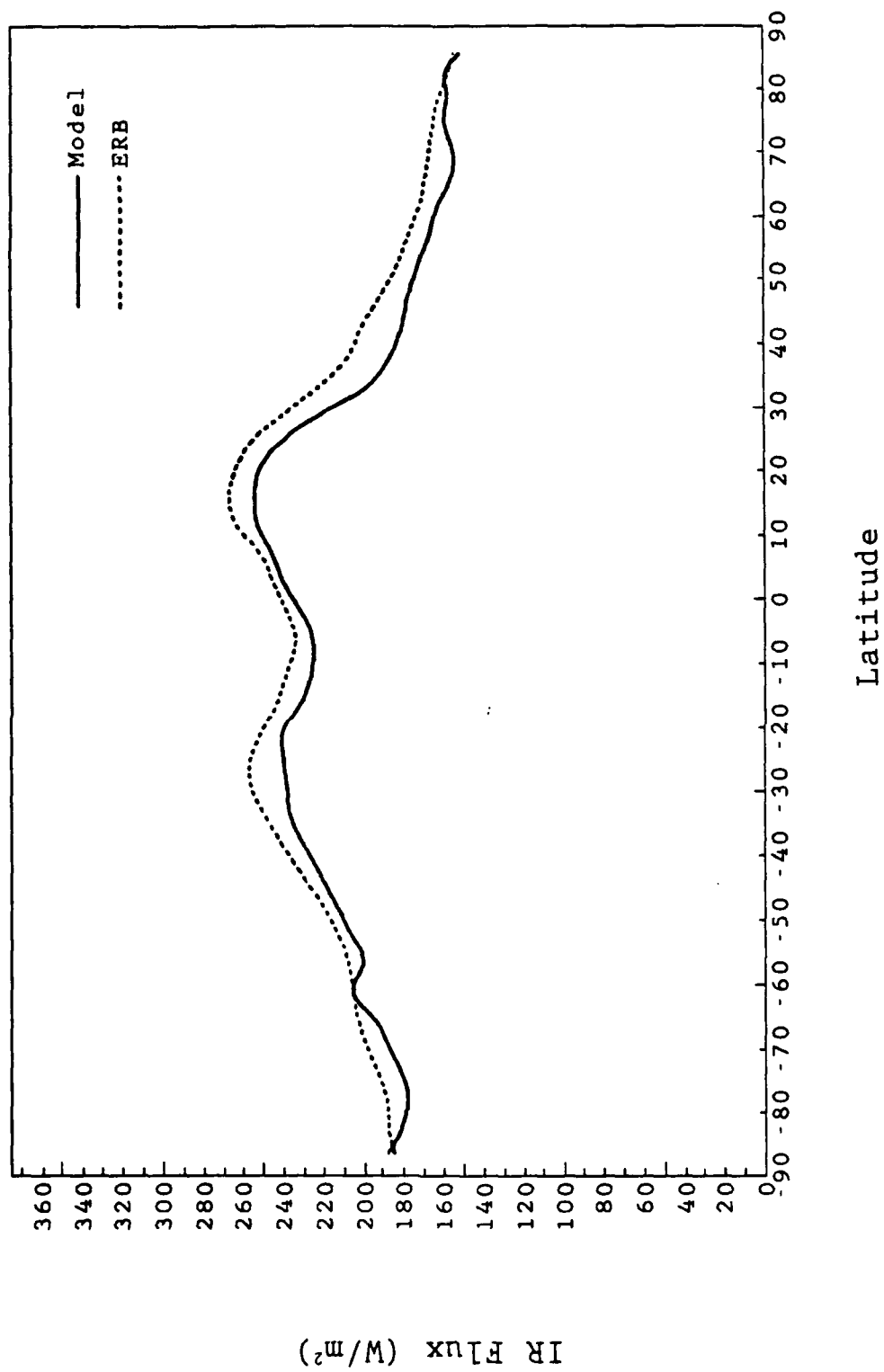


Fig 3.12 January 1979, Model versus ERB, zonal average outgoing TOA IR flux.

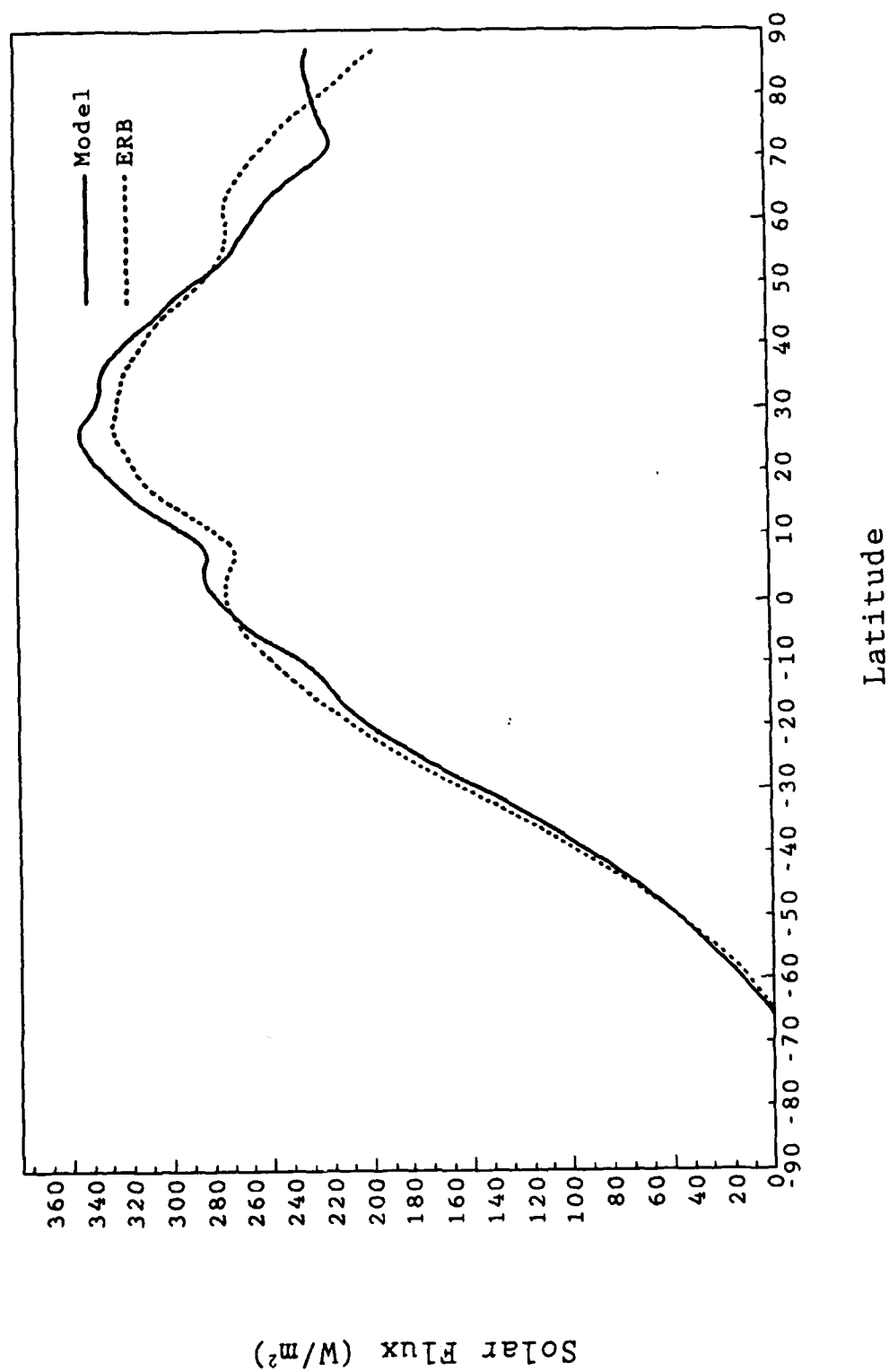


Fig 3.13 July 1979. Model versus ERB, zonal average net downward TOA solar flux.

The dip in the curve at 10°N corresponds to the sharp maximum in the total cloud amount (Figure 2.14) associated with the ITCZ. There is a slight dip in the curve at approximately 52°N , which is associated with the northern storm track (Figure 2.14). Figure 3.14 is a comparison of the model and ERB results for the July 1979 zonal average IR flux. As with Figure 3.13, the differences are within 20 W/m^2 . The minimum in the curve ($\approx 10^{\circ}\text{N}$) correlates to the sharp maximum in the total cloud amount (Figure 2.14) associated with the ITCZ. The maxima in the curve on both sides of the minimum ($\approx 20^{\circ}\text{S}$ and $\approx 30^{\circ}\text{N}$) are associated with the southern and northern subtropical highs. The rapid drop in IR flux values occurring from 60°S southward is due to the cold surface temperatures that occur on the Antarctic plateau. Comparing Figures 3.13 and 3.14, the results of the model are generally consistent except in the region from 5°S to 50°N . Here, the model solar flux results exceed those of the ERB, while the model IR flux results do not. Comparing Figures 2.13 and 2.14 (January and July cloud climatologies) with Figures 3.11 and 3.13 (January and July solar flux at TOA) shows that the January maxima ($\approx 330 \text{ W/m}^2$, model: 360 W/m^2 , ERB) occur at 30°S , where the total cloud amount is 50%. For July, the maximum solar flux at TOA is $\approx 340 \text{ W/m}^2$ for the model and 330 W/m^2 for the ERB. This occurs at $\approx 20^{\circ}\text{N}$, where the total cloud amount is 40%. Thus, whereas the model values increase 10 W/m^2 with a decrease in clouds, the ERB values decrease 30 W/m^2 . From this it would seem that the model results are more consistent than the ERB results.

Figure 3.15 shows the January 1979 global net surface solar

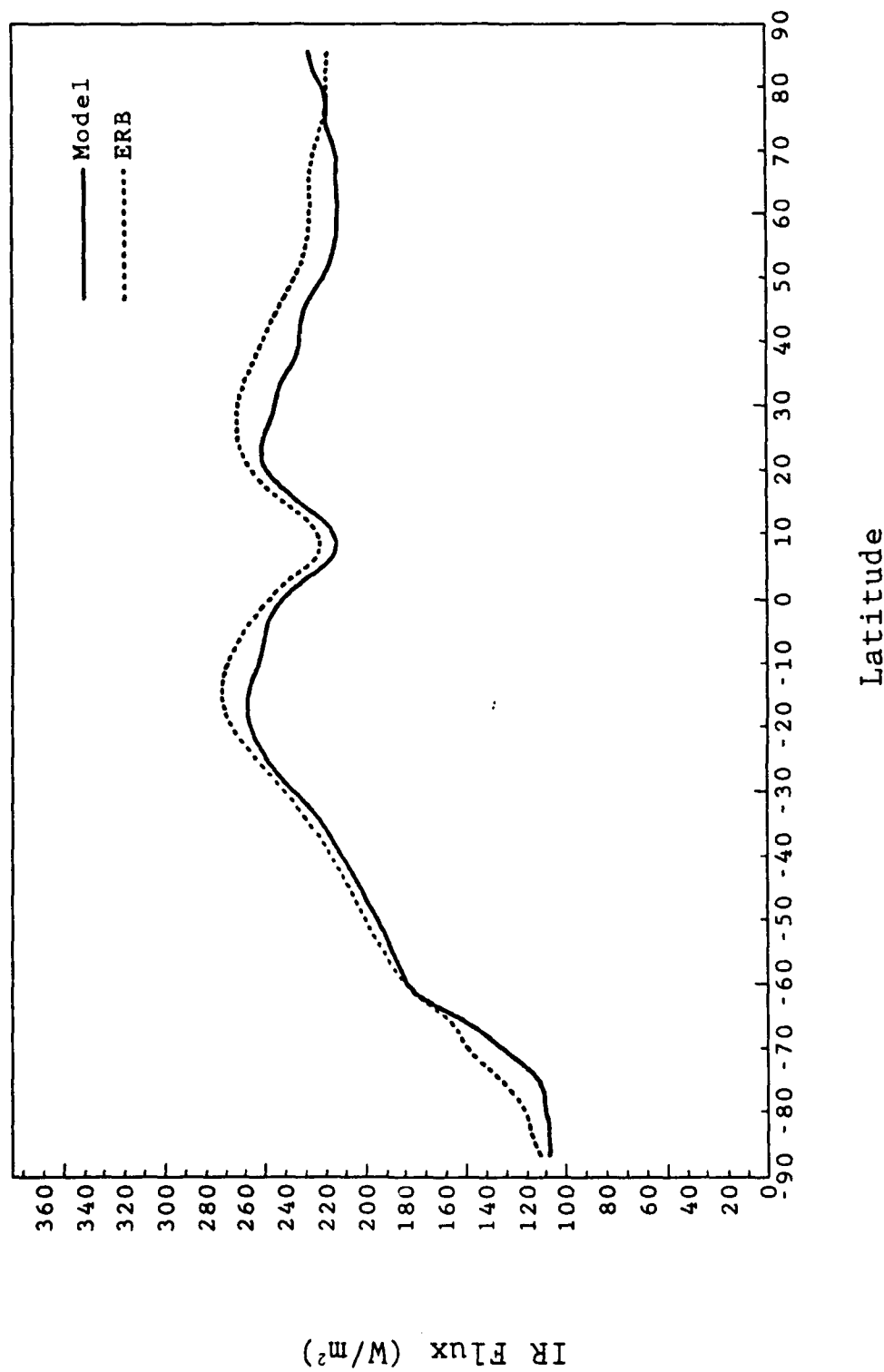


Fig 3.14 July 1979, Model versus ERB, zonal average outgoing TOA IR flux.

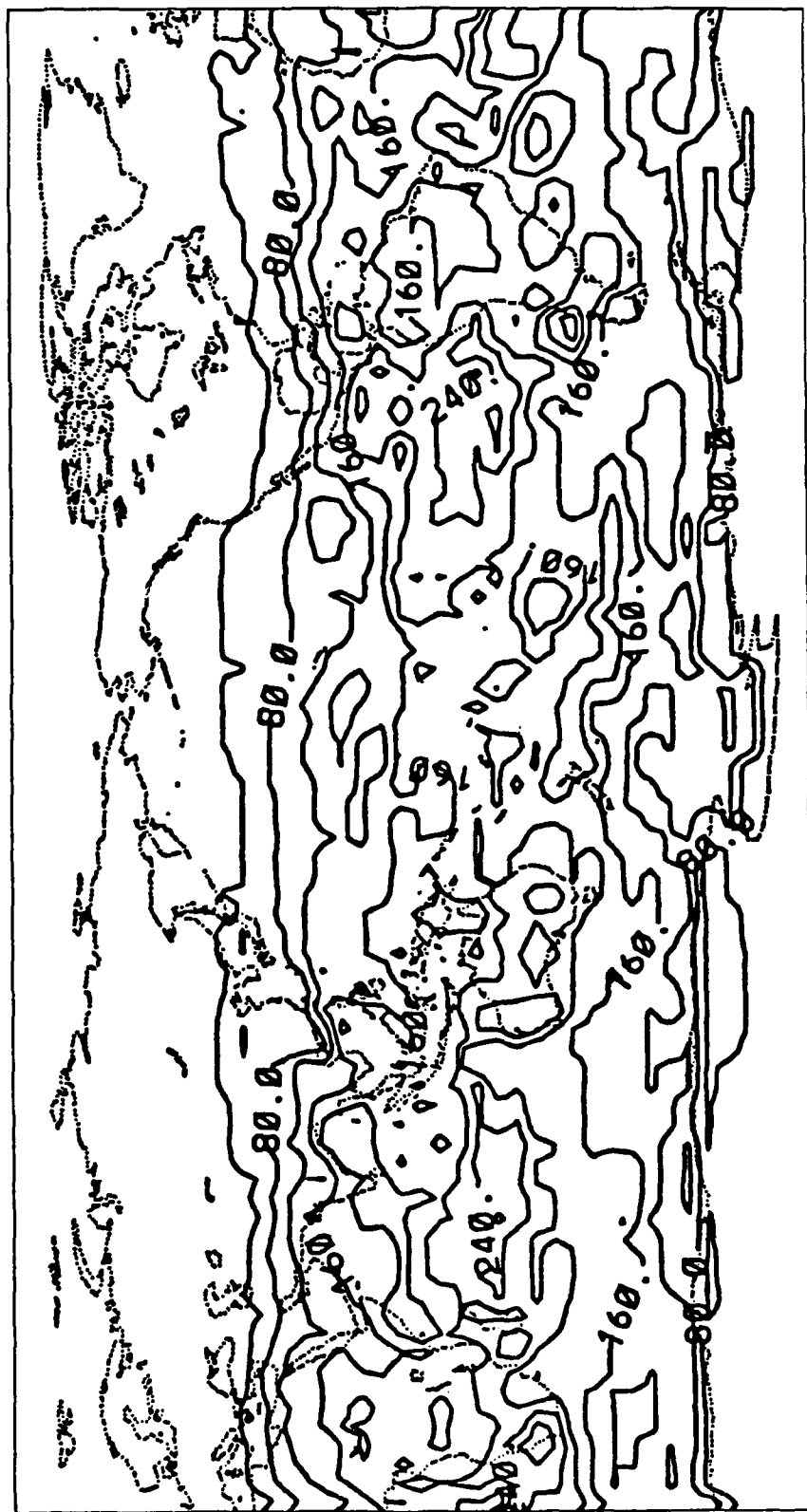


Fig 3.15 January 1979, Model global downward surface solar flux (W/m^2). Contour interval is 40 W/m^2 .

flux. In the Northern Hemisphere, north of $\approx 20^{\circ}\text{N}$, there is a zonal distribution (Northern Hemisphere winter) of solar flux decreasing from 80 to 0 W/m^2 . From $\approx 20^{\circ}\text{N}$ southward, the zonal pattern changes to one having more features due to convective heating. Proceeding southward, this new convective pattern does not change until Antarctica. The maximum values of the surface solar flux can exceed 240 W/m^2 in the southern subtropical high, where there is a minimum of cloud cover and a maximum of solar flux. The minimum values of the surface solar flux are found in the Arctic region ($\approx 0 \text{ W/m}^2$), where in January it is the land of eternal night. Griffin (1987) presented surface solar and IR flux values for the United States and China for January and July 1979. The model surface solar flux values are within 20 W/m^2 as compared to Griffin (1987) over the United States and China. Figure 3.16 shows the monthly average global surface IR flux for January 1979. Since the surface IR flux is a function of the surface temperature, it is expected that the maximum IR flux will be located where the surface temperatures are the greatest. As Figure 3.16 clearly shows, the maximum IR flux values occur over Australia and South Africa with values exceeding 120 W/m^2 , and the Sahara desert with values exceeding 160 W/m^2 . All of these areas have less than 20% total cloud cover for January 1979 (Figure 2.8). The minimum values occur in the Arctic, where surface IR flux values approach 0 W/m^2 . Over the United States and China the IR surface flux results are within 10 W/m^2 of Griffin's (1987) results.

Figure 3.17 shows the July 1979 global surface solar flux. The Southern Hemisphere from 20°S southward displays a zonal distribution



Fig 3.16 January 1979. Model global upward surface IR flux (W/m^2).
Contour interval is 20 W/m^2 .

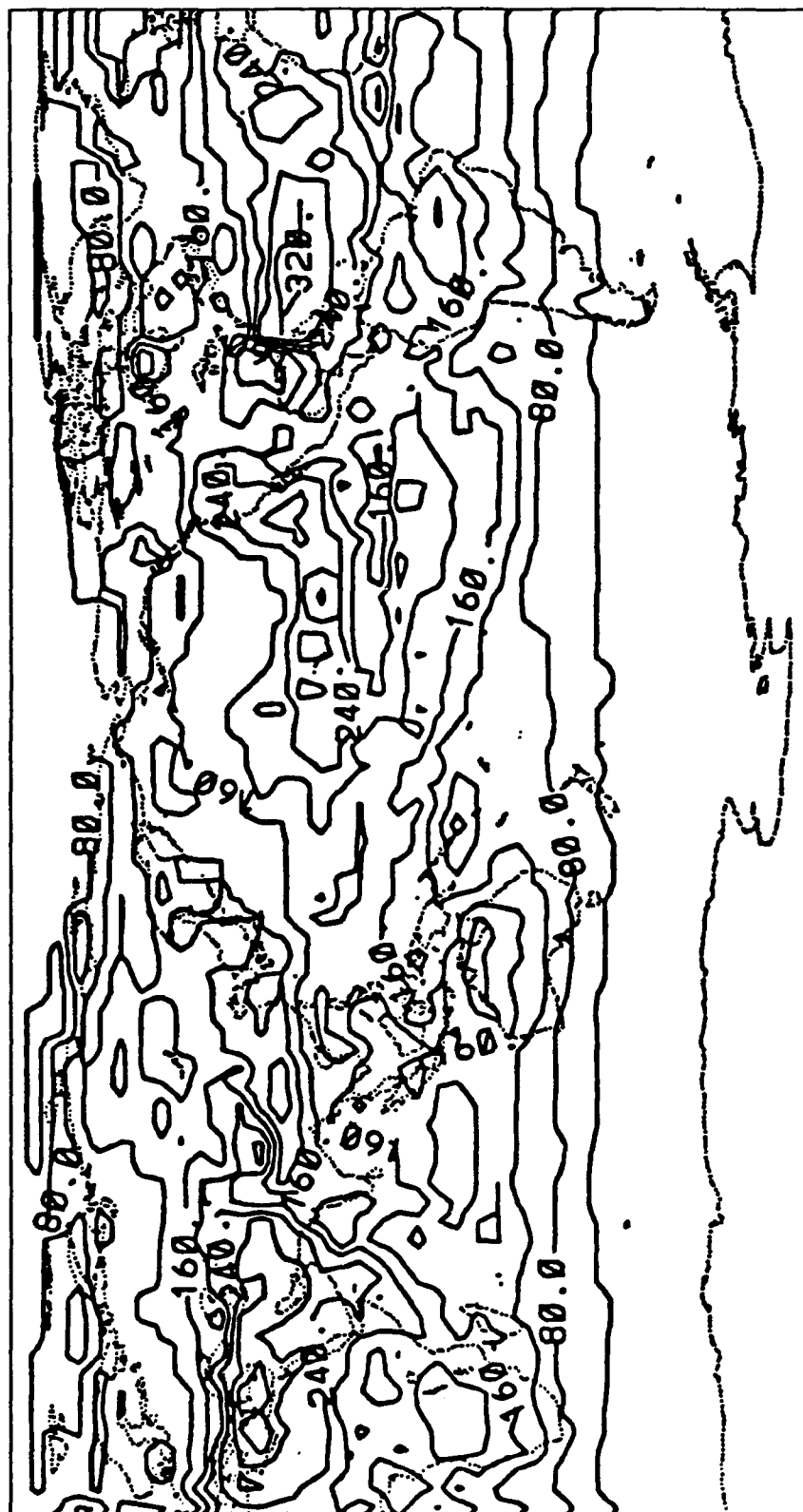


Fig 3.17 July 1979. Model global downward surface solar flux (W/m^2).
Contour interval is 40 W/m^2 .

(Southern Hemisphere winter) of the surface solar flux with values ranging from 120 to 0 W/m^2 . From 20°S northward, the zonal pattern changes to one having more features due to increased surface heating. In the region of the southern subtropical high, the surface flux can exceed 240 W/m^2 . In the area of the ITCZ (see Figure 2.14), the surface solar flux values reduce to $\approx 160 \text{ W/m}^2$, due to increased cloud cover. At the northern subtropical high, values can exceed 320 W/m^2 . This is an area typified by low cloud amounts and maximum solar flux. The surface solar flux decreases poleward, where surface solar flux values can be less than $\approx 80 \text{ W/m}^2$. When comparing the model results for the United States and China to Griffin's (1987) results, the surface solar flux values are within 15 W/m^2 . Figure 3.18 shows the July 1979 global surface IR flux. As in January, the maximum value of the surface IR flux will be found where the surface temperatures are the greatest. These areas are also typified by low cloud amounts allowing for maximum surface heating. These areas are South Africa and Australia (IR surface flux values exceeding 120 W/m^2 and cloud cover $\leq 20\%$), the western coast of South America (IR surface flux values exceeding 120 W/m^2 and cloud cover $\leq 30\%$), and North Africa (IR surface flux values exceeding 140 W/m^2 and cloud cover $\leq 20\%$). The minimum values occur in the Arctic region ($\approx 40 \text{ W/m}^2$) and in the Antarctic region ($\approx 0 \text{ W/m}^2$). Comparing the model surface IR flux results for the United States and China to Griffin's results, the two agree to within 10 W/m^2 .

Figure 3.19 shows the January 1979 zonal average surface solar flux. The maximum surface solar flux value of $\approx 210 \text{ W/m}^2$ occurs in the

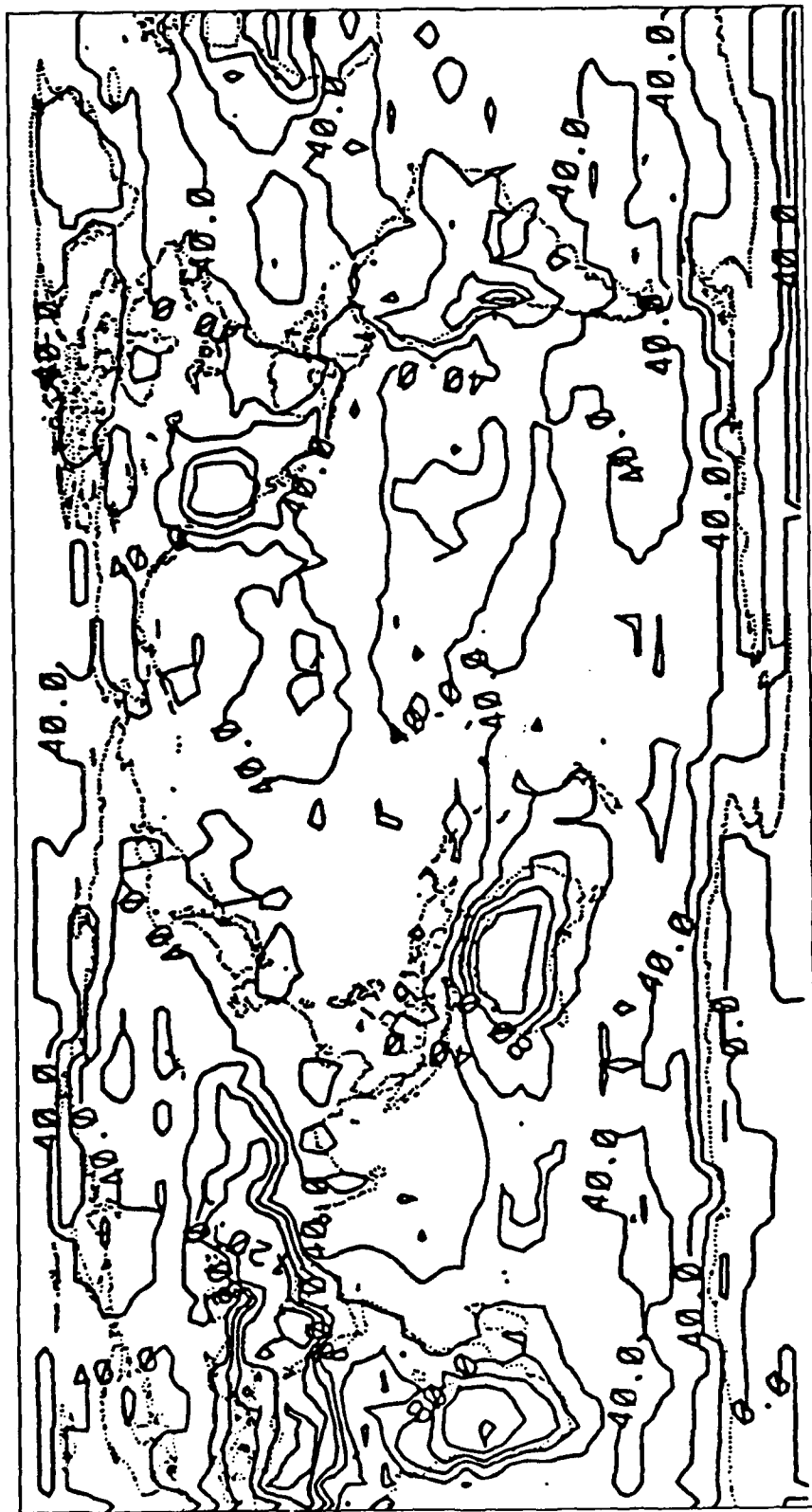


Fig 3.18 July 1979, Model global upward surface IR flux (W/m^2).
Contour interval is 40 W/m^2 .

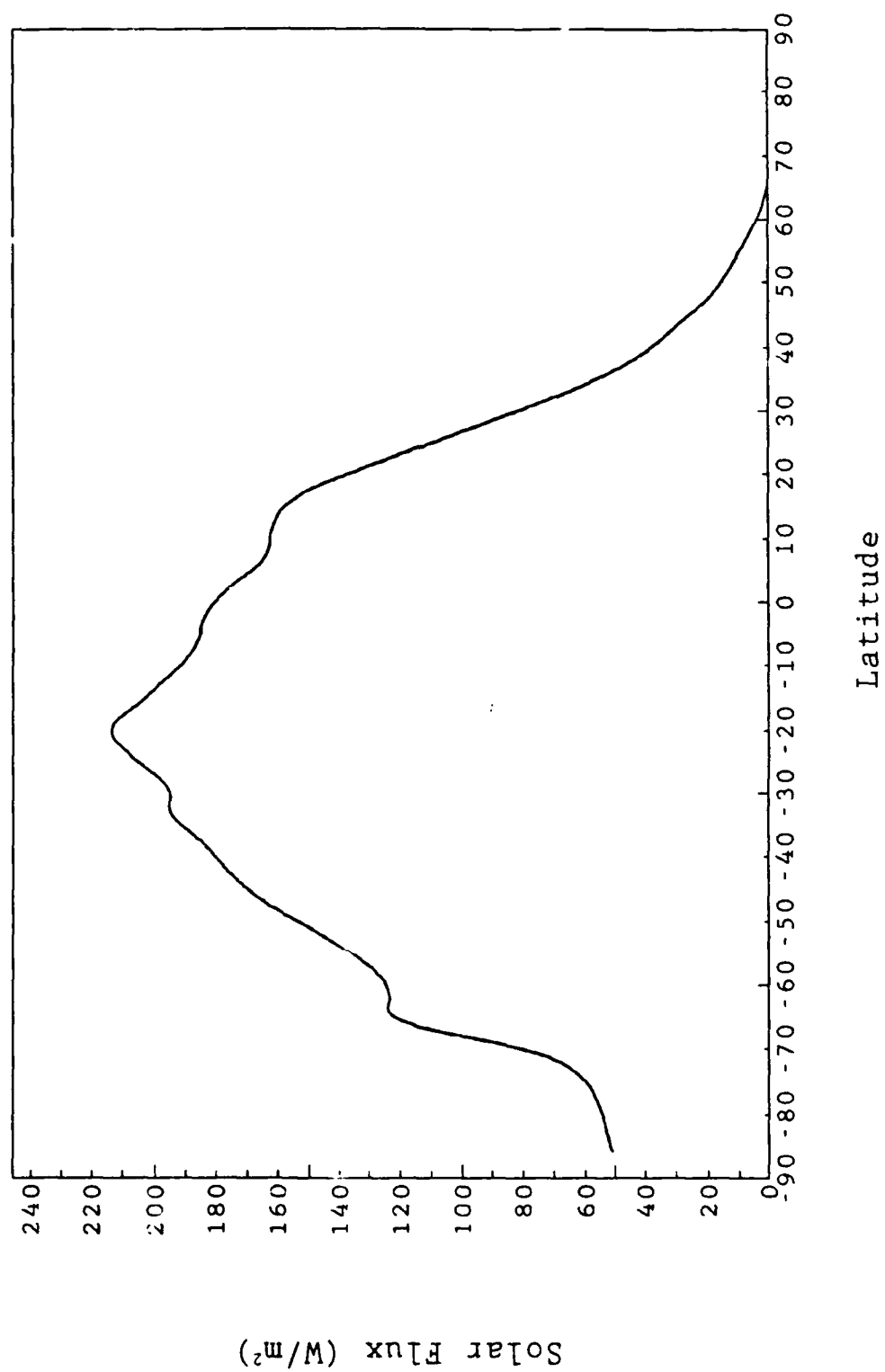


Fig 3.19 January 1979, zonal average downward surface solar flux.

region of the southern subtropical high where there is a low total cloud amount of $\approx 50\%$ and a maximum of solar flux. This is the same latitude of the maximum TOA solar flux and is approximately 100 W/m^2 less. The difference in the solar flux is mostly due to the solar flux being reflected by the earth's clouds. Figure 3.20 shows the January 1979 zonal average surface IR flux. The maximum values of the surface IR flux occur at the same place as the TOA IR flux, 30°S and 20°N , with values of 50 and 10 W/m^2 , respectively. These maximum values are reached in the regions of the southern and northern subtropical high where the cloud amounts are lower and the surface heating higher. The minimum between the two maxima is associated with the ITCZ (see Figure 2.13), where the cloud cover is the highest and the surface heating the lowest. The maximum over the Antarctic region (70 W/m^2) is due to low cloud amounts ($\approx 25\%$) during the summer. The difference between TOA IR flux and surface IR flux is approximately 170 W/m^2 . This difference can be attributed to the amount of IR flux that the atmosphere absorbs due to IR heating.

Figure 3.21 illustrates the July 1979 zonal average surface solar flux. The maximum amount of surface solar flux (230 W/m^2) is at the same location ($\approx 20^\circ\text{N}$) as the maximum for TOA, but is $\approx 100 \text{ W/m}^2$ less. The difference is attributed to the solar flux being reflected by the earth's clouds. The dip in the curve at 10°N is due to a sharp increase in the cloud cover (to $\approx 90\%$) in the region of the ITCZ (Figure 2.14). The maximum in the Arctic region is due to low cloud amounts (Figure 2.14) of $\approx 30\%$ and a high surface albedo of ≈ 0.6 (Figure 2.2).

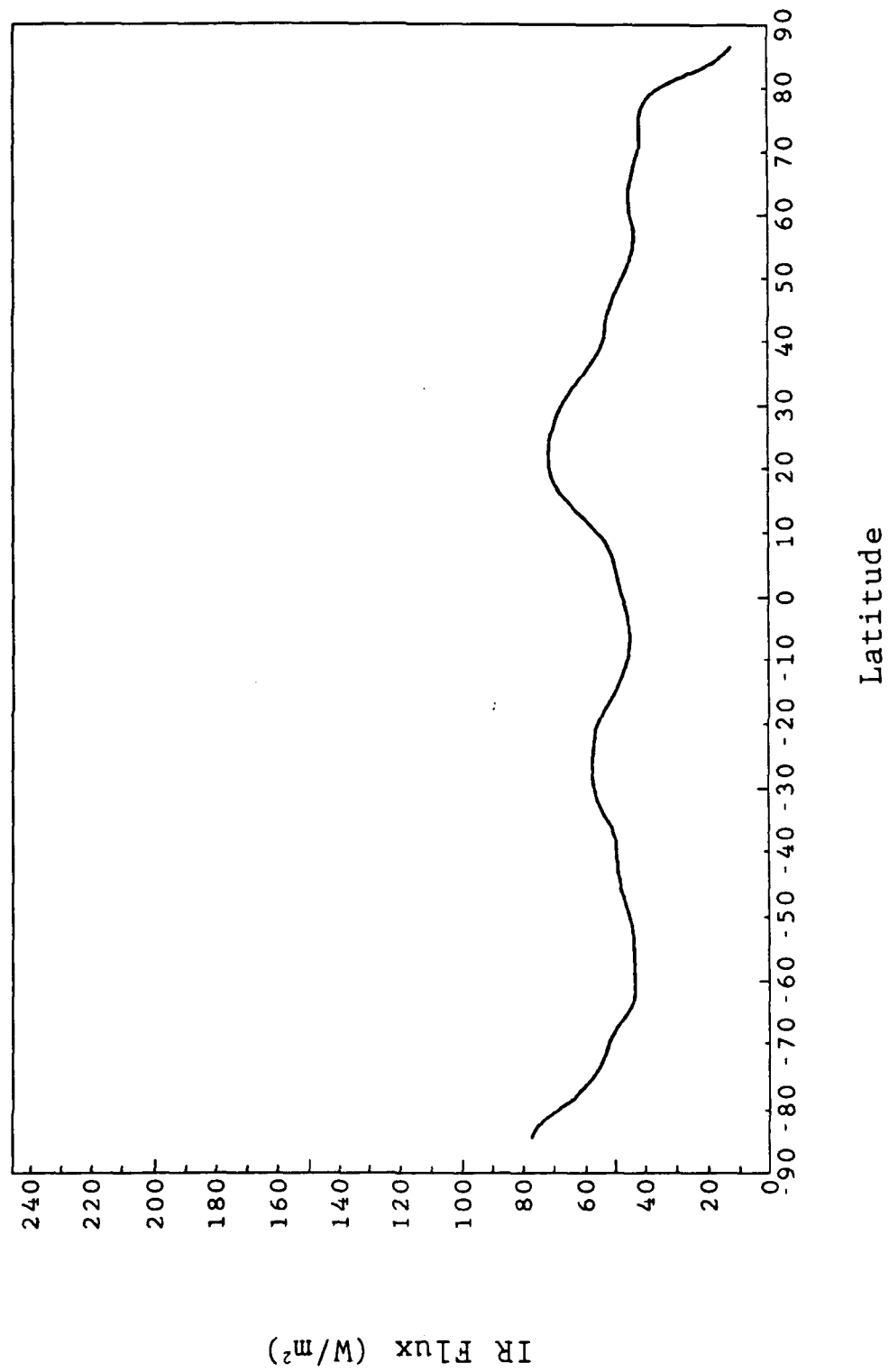


Fig 3.20 January 1979, zonal average upward surface IR flux.

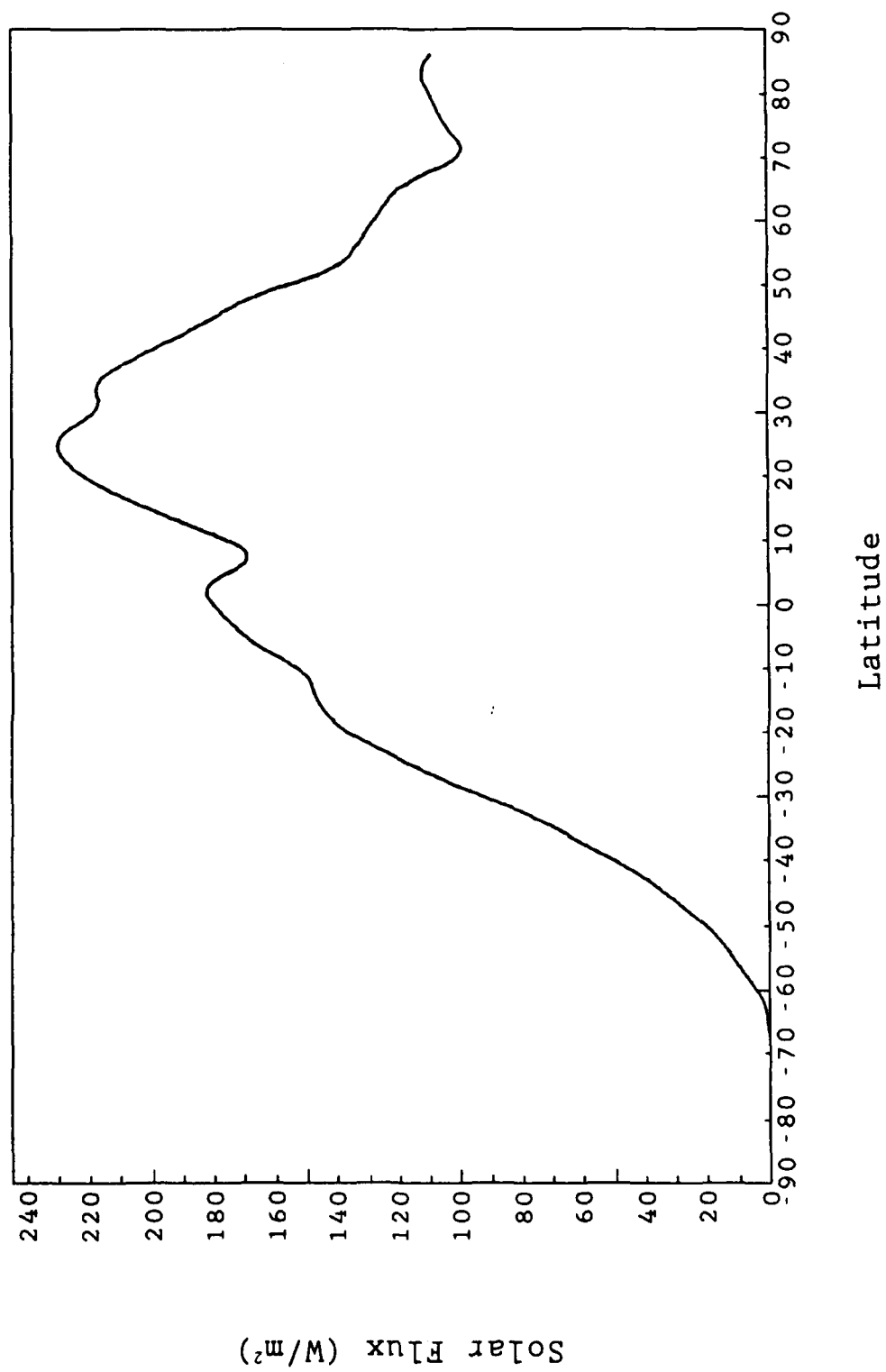


Fig 3.21 July 1979, zonal average downward surface solar flux.

The July 1979 zonal average surface IR flux pattern is shown in Figure 3.22. The maxima of the surface IR flux occur at the same places ($\approx 25^{\circ}\text{S}$ and $\approx 30^{\circ}\text{N}$) as the maxima for TOA IR flux, but are on the order of 170 W/m^2 less ($\approx 60 \text{ W/m}^2$). Their locations are associated with the subtropical highs, a region of low clouds and high surface heating. The difference in the IR flux can be attributed to the amount of IR flux being absorbed by the atmosphere. The minimum ($\approx 30 \text{ W/m}^2$ at 10°N) between the two maxima is associated with the ITCZ (see Figure 2.14), a region of high cloud cover ($\approx 70\%$). The maximum located in the Arctic region ($\approx 45 \text{ W/m}^2$) is due to low cloud cover ($\approx 30\%$) in the summertime.

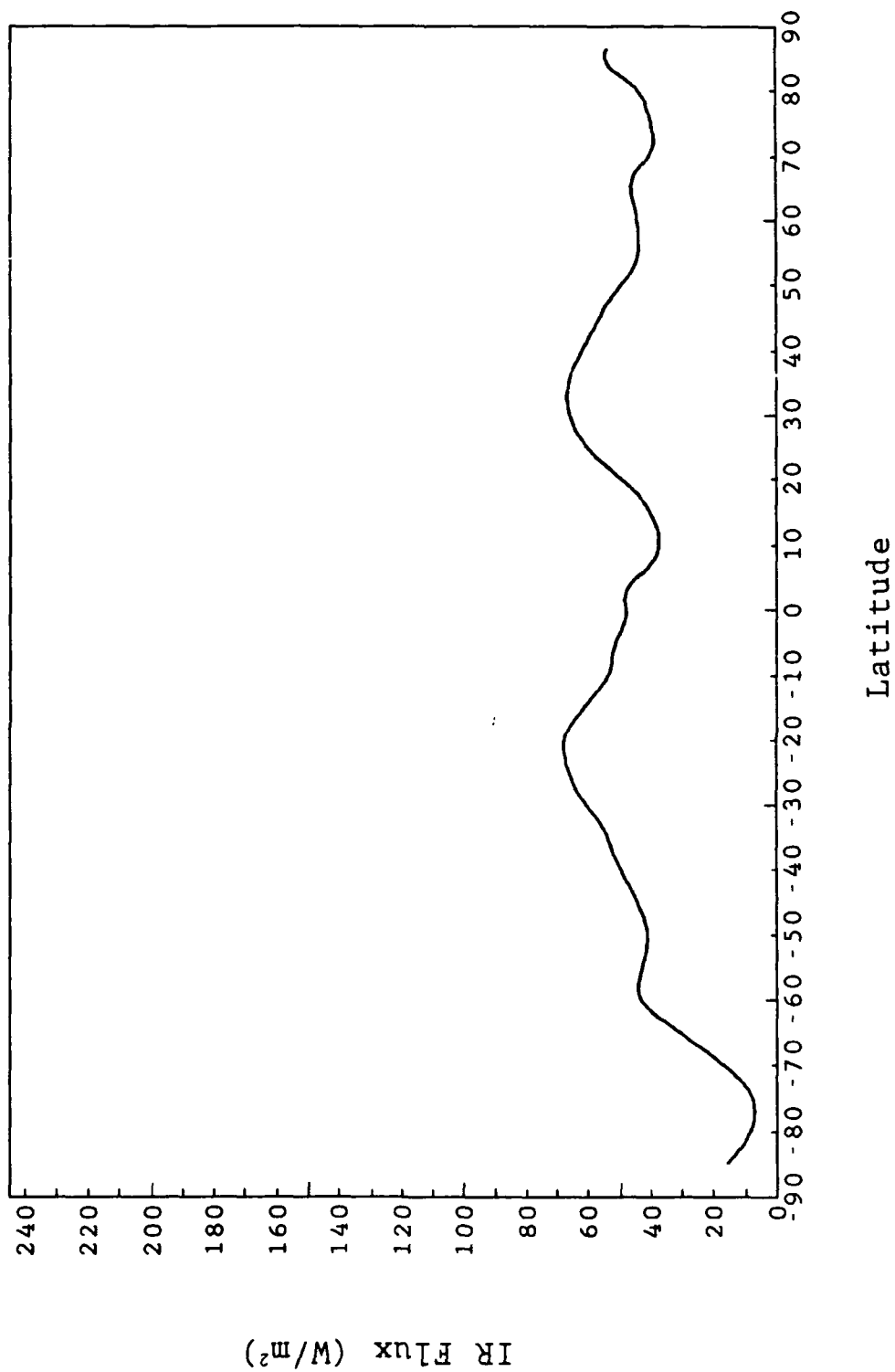


Fig 3.22 July 1979, zonal average upward surface IR flux.

CHAPTER 4

CLOUD RADIATIVE FORCING

As is well-known, cloud-radiation interactions in the general circulation of the atmosphere may be considered separately in two spectral regions, the incoming solar radiation from the sun and the outgoing IR radiation emitted by the planetary system. For solar radiation, clouds reflect it back to space and thus cool the system. In contrast, since cloud top temperatures are generally lower than those of the underlying atmosphere and surface, clouds reduce the outgoing IR radiation and thus enhance the greenhouse warming of the system. A determination of the net radiative effect of clouds on climate thus requires quantification of these two opposing forces.

4.1 TOA Fluxes

Similar to Ramanathan (1987), let F be the area-mean radiative flux at TOA reflected by, or emitted from, a region with partial cloud cover and let F_c be the flux for clear skies. Then the cloud radiative forcing, C_f , is defined by

$$C_f = F - F_c. \quad (4.1)$$

As mentioned previously, cloud radiative forcing may be considered separately in the solar and IR spectral regions.

4.1.1 Cloud Solar Forcing

Cloud solar forcing, C_{sf} , is defined by

$$C_{sf} = F_s - F_{sc}. \quad (4.2)$$

where F_S is the net downward flux absorbed by the earth's atmosphere for a partly cloudy atmosphere, and F_{Sc} is the flux for clear skies. C_{sf} is a measure reflecting the effect of the presence of clouds. Cloud forcing experiments are performed for January 1979 only. The results for July 1979 are omitted for the sake of brevity; both months on a global scale and seasonal basis are the same. Figure 4.1 shows the global monthly average, F_S , at TOA. This figure was previously described in Chapter 3 (Figure 3.3, top) and is included here for comparison. Figure 4.2 shows the global monthly average, F_{Sc} , at TOA. In the low latitude areas F_{Sc} is greater than F_S because the albedo of the clouds is much greater than that of the underlying surface. The exception to this is the high albedo of North Africa. Here the patterns are very similar. Because of the high albedos of the snow cover and sea-ice, the high latitudes are also very similar. Now, since F_{Sc} is greater than F_S , C_{sf} is negative. Figure 4.3, which plots solar cloud forcing, bears out the previous statement, and corresponds to the cooling of the earth-atmosphere system. The forcing has a maximum over the Southern Hemisphere midlatitudes, where both the insolation and cloud cover are large. Figure 4.3 shows that, in January 1979, most of the forcing occurs over the southern oceans. Compared to Slingo and Slingo (1988), who used persistent January cloud climatology values for the computations, the model results were lower by 40 W/m^2 . The difference can be accounted for by differences in the cloud fields.

4.1.2 Cloud IR Forcing

Cloud IR forcing, C_{IRf} , is given by

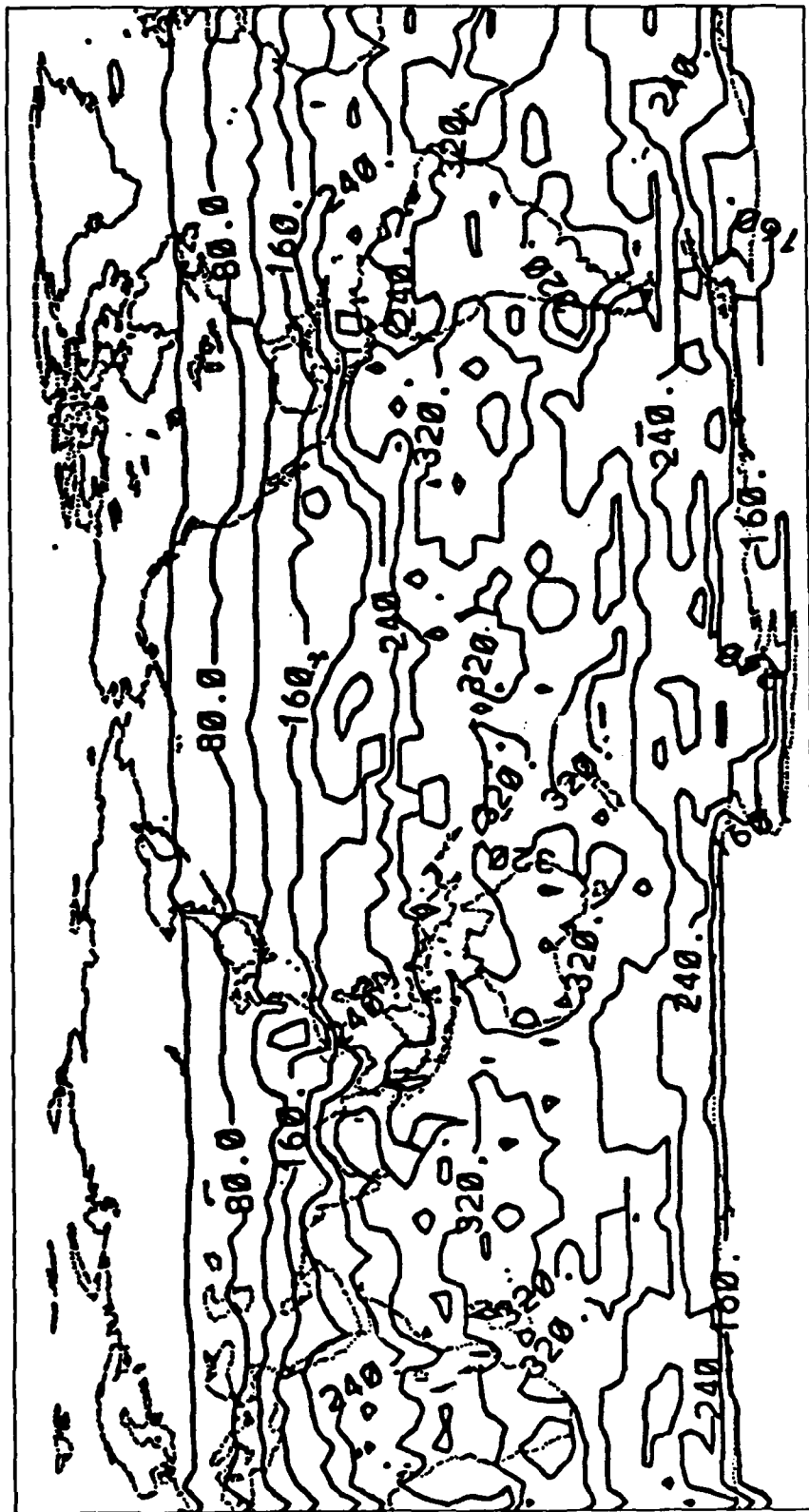


Fig 4.1 January 1979, Model global net downward TOA solar flux (W/m^2) for a partially cloudy sky. Contour interval is 40 W/m^2 .

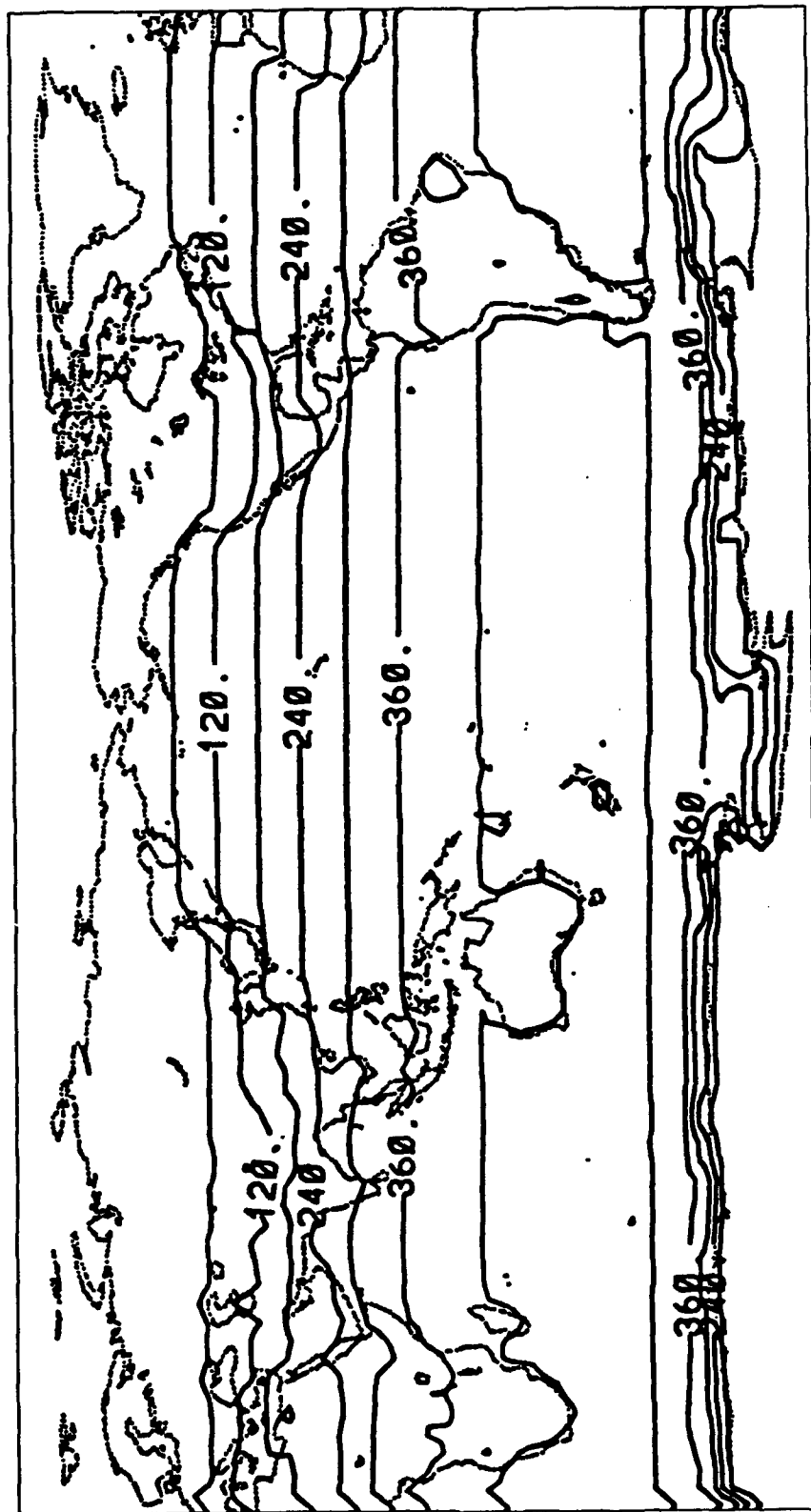


Fig 4.2 January 1979. Model global net downward TOA solar flux (W/m^2) for a clear sky. Contour interval is 60 W/m^2 .

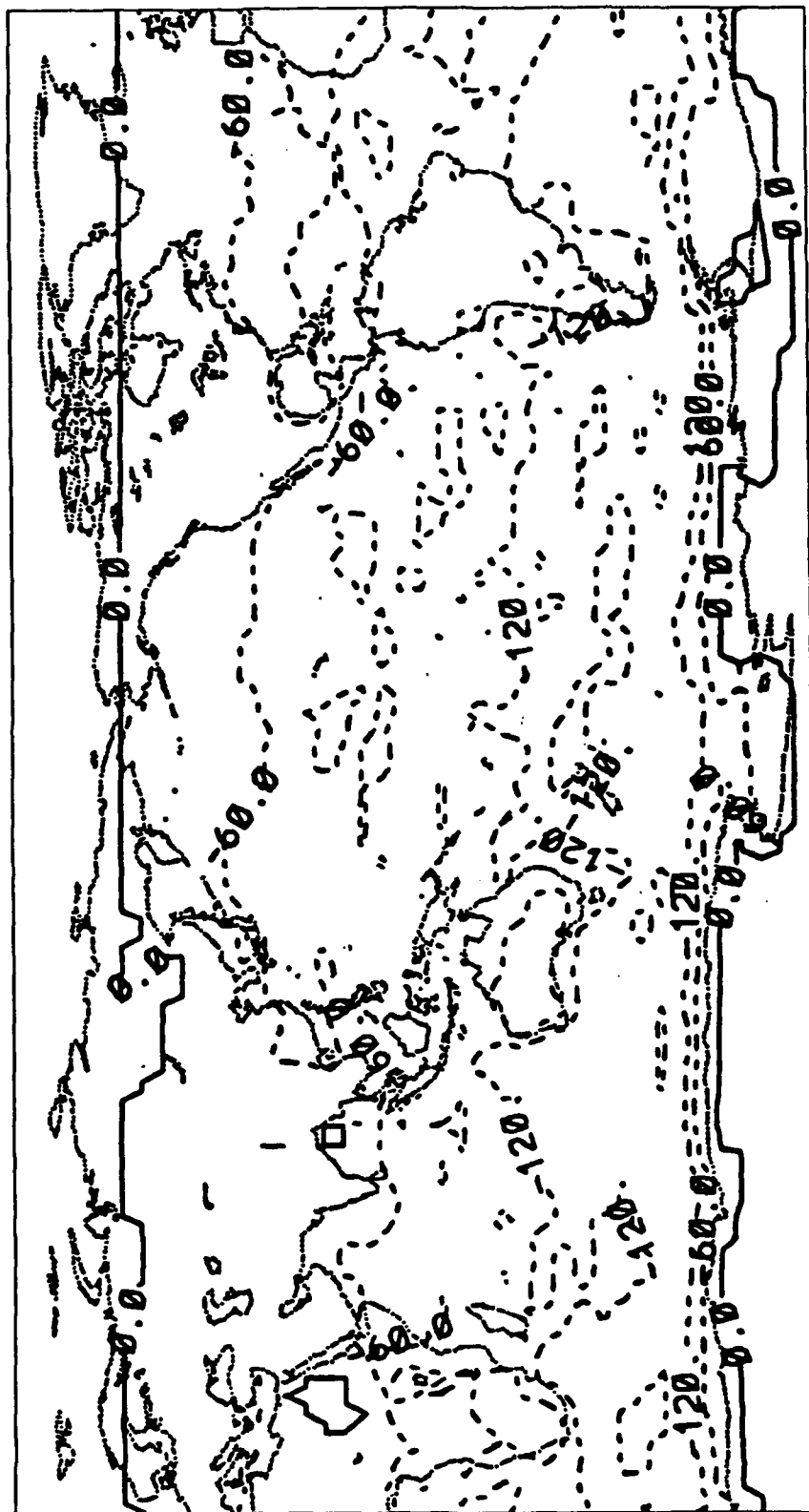


Fig 4.3 January 1979, Model global cloud forcing of the net incoming TOA solar flux (W/m^2). Contour interval is 60 W/m^2 .

$$CIRf = FIR - FIRc. \quad (4.3)$$

where FIR is the outgoing IR flux, and $FIRc$ is the value for clear skies. $CIRf$ is a measure reflecting the effect of the presence of clouds. Figure 4.4 shows the global monthly average FIR at TOA. This plot has been described in Chapter 3 (Figure 3.4) and is used here for comparison. Figure 4.5 depicts the global monthly average $FIRc$ at TOA. In the tropics, the value of $FIRc$ is typically about 280 W/m^2 and decreases poleward due to the lower surface and atmospheric temperatures. At high northern latitudes, the values are lowest over the cold continents and largest over the relatively warm North Atlantic Ocean. The greatest difference between Figures 4.4 and 4.5 is therefore in those regions where persistent high (and therefore cold) clouds are found above a warm surface, that is, in the areas of deep tropical convection and in the North Atlantic storm track. These are the regions that show the largest values of the cloud IR forcing (Figure 4.6), as was also noted by Slingo and Slingo (1988) and by Hartmann et al. (1986). The values from Slingo and Slingo (1988) are within 10 W/m^2 of our results. The IR forcing is negative everywhere, showing that clouds warm the lower atmosphere by enhancing the greenhouse effect.

4.1.3 Net Cloud Forcing

Net cloud forcing, CNf , is given by

$$CNf = FN - FNC. \quad (4.4)$$

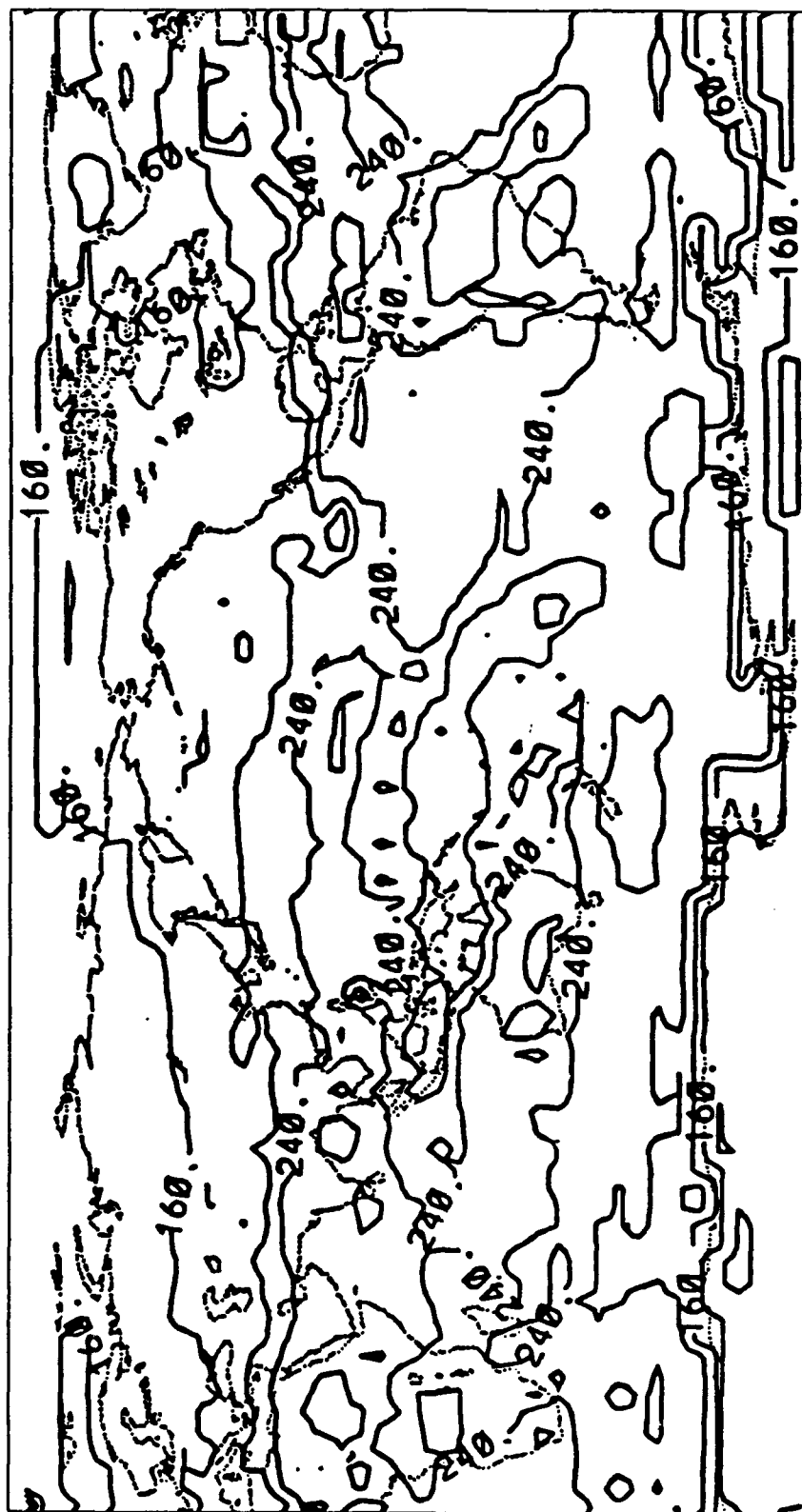


Fig 4.4 January 1979, Model global outgoing TOA IR flux (W/m^2) for a partially cloudy sky. Contour interval is 40 W/m^2 .

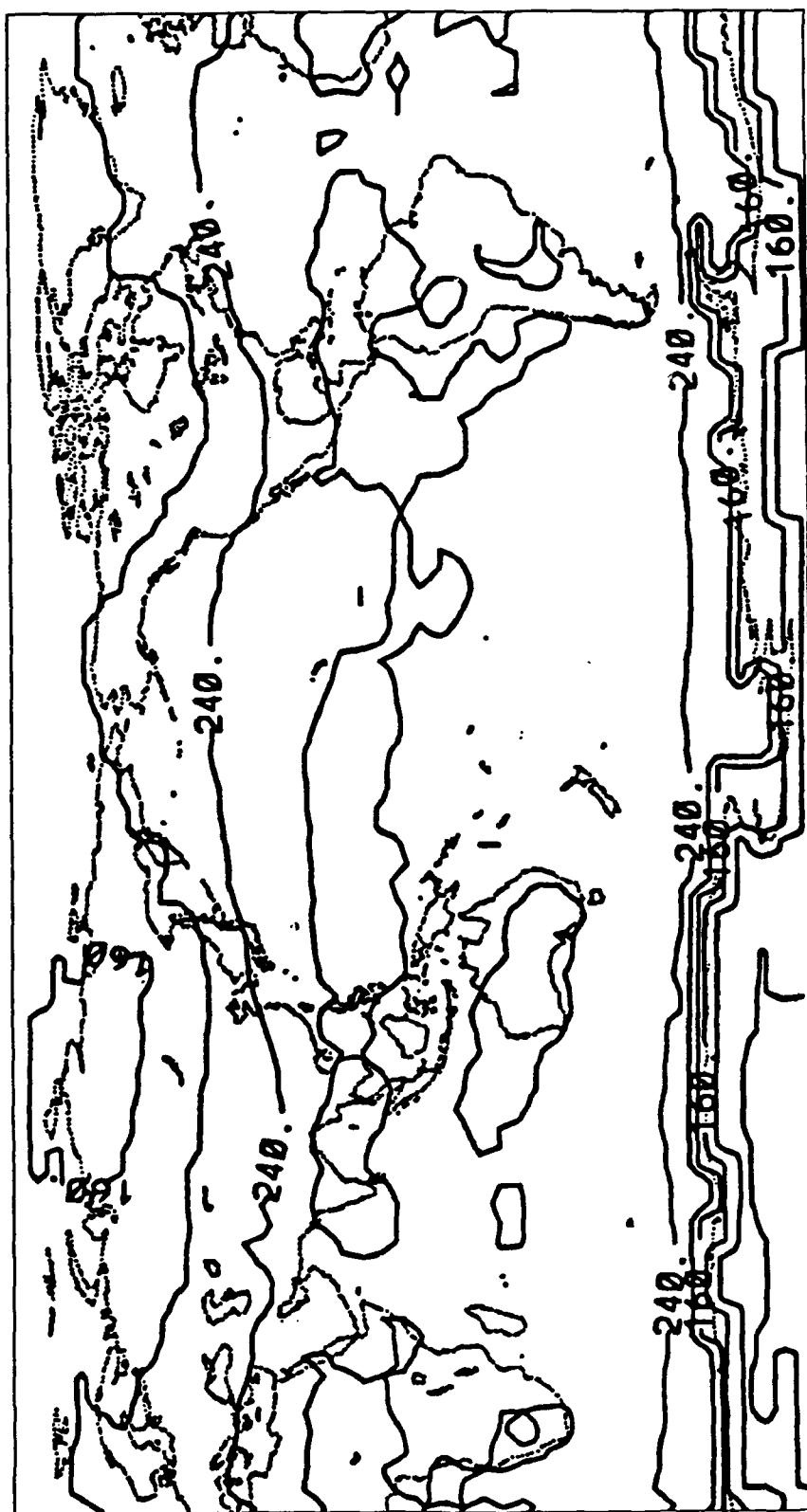


Fig 4.5 January 1979, Model global outgoing TOA IR flux (W/m^2) for a clear sky. Contour interval is 40 W/m^2 .

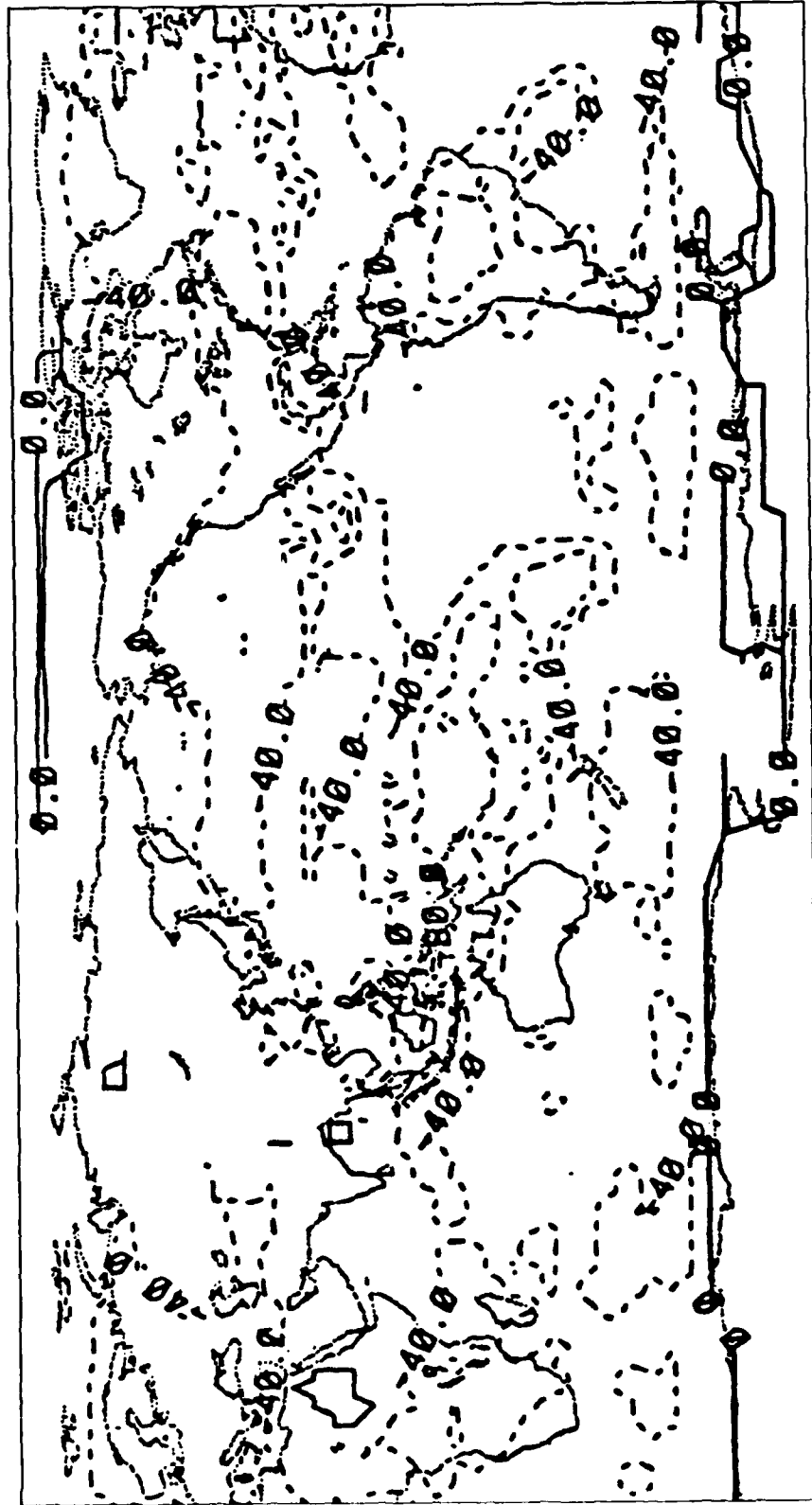


Fig 4.6 January 1979, Model global cloud forcing of the outgoing TOA IR flux (W/m^2). Contour interval is 40 W/m^2 .

where F_N is the net flux, and F_{Nc} is the value for clear skies. Since the net flux is equal to the difference between the net incoming solar flux and the net outgoing IR flux, the net cloud forcing, CN_f , becomes

$$CN_f = C_{sf} - C_{IRf}. \quad (4.5)$$

CN_f is a measure reflecting the effect of the presence of clouds. Figure 4.7 shows the global monthly average of the F_N at TOA. F_N is a measure of the difference between the solar and IR fluxes. For January 1979, the positive F_N is almost entirely in the Southern Hemisphere between the equator and Antarctica. The maximum value exceeds 160 W/m^2 in the southern midlatitudes. The negative F_N is almost entirely in the Northern Hemisphere with the exception of Antarctica, where the magnitude of the values exceeds -40 W/m^2 . In the Northern Hemisphere, the magnitude of the values exceeds -160 W/m^2 over the North American continent. The Northern Hemisphere pattern is somewhat zonal, while the Southern Hemisphere, which has more heating, displays a more convective pattern. Figure 4.8 shows the global monthly average of F_{Nc} at TOA. From the equatorial region southward to Antarctica, the net flux is positive with values exceeding 160 W/m^2 . Antarctica itself has mostly negative net fluxes, with the magnitude of the values exceeding -40 W/m^2 . From the equatorial region northward, the rest of the Northern Hemisphere is negative with the magnitude of the values exceeding -160 W/m^2 . Both the Northern and Southern Hemispheres display a very zonal flux poleward in magnitude. Figure 4.9 shows the global monthly average CN_f at TOA. With the exception of Antarctica, and small areas of South Africa and South America, the entire Southern Hemisphere has a negative CN_f , with

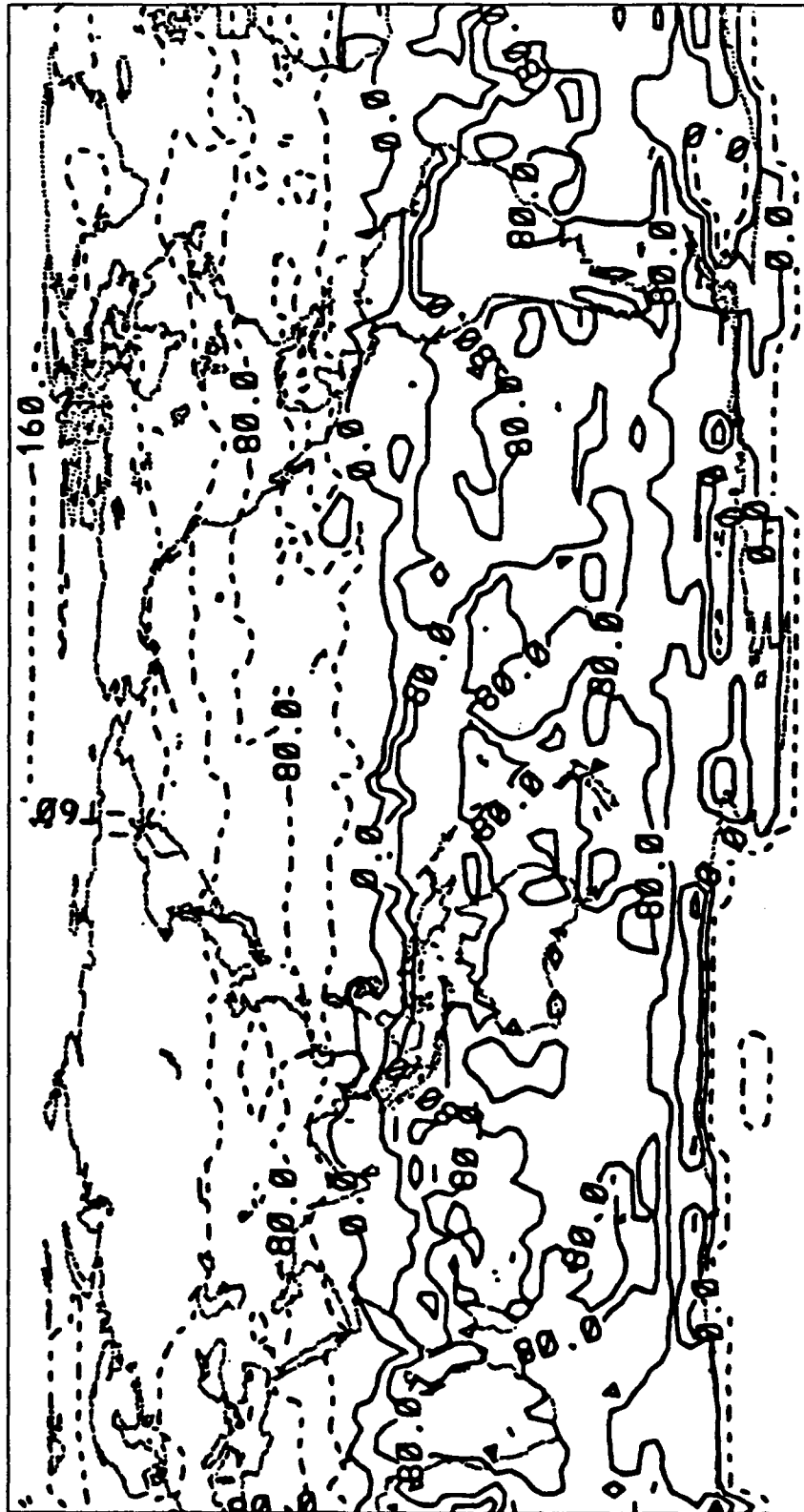


Fig 4.7 January 1979, Model global net TOA flux (W/m^2) for a partially cloudy sky. Contour interval is 40 W/m^2 .

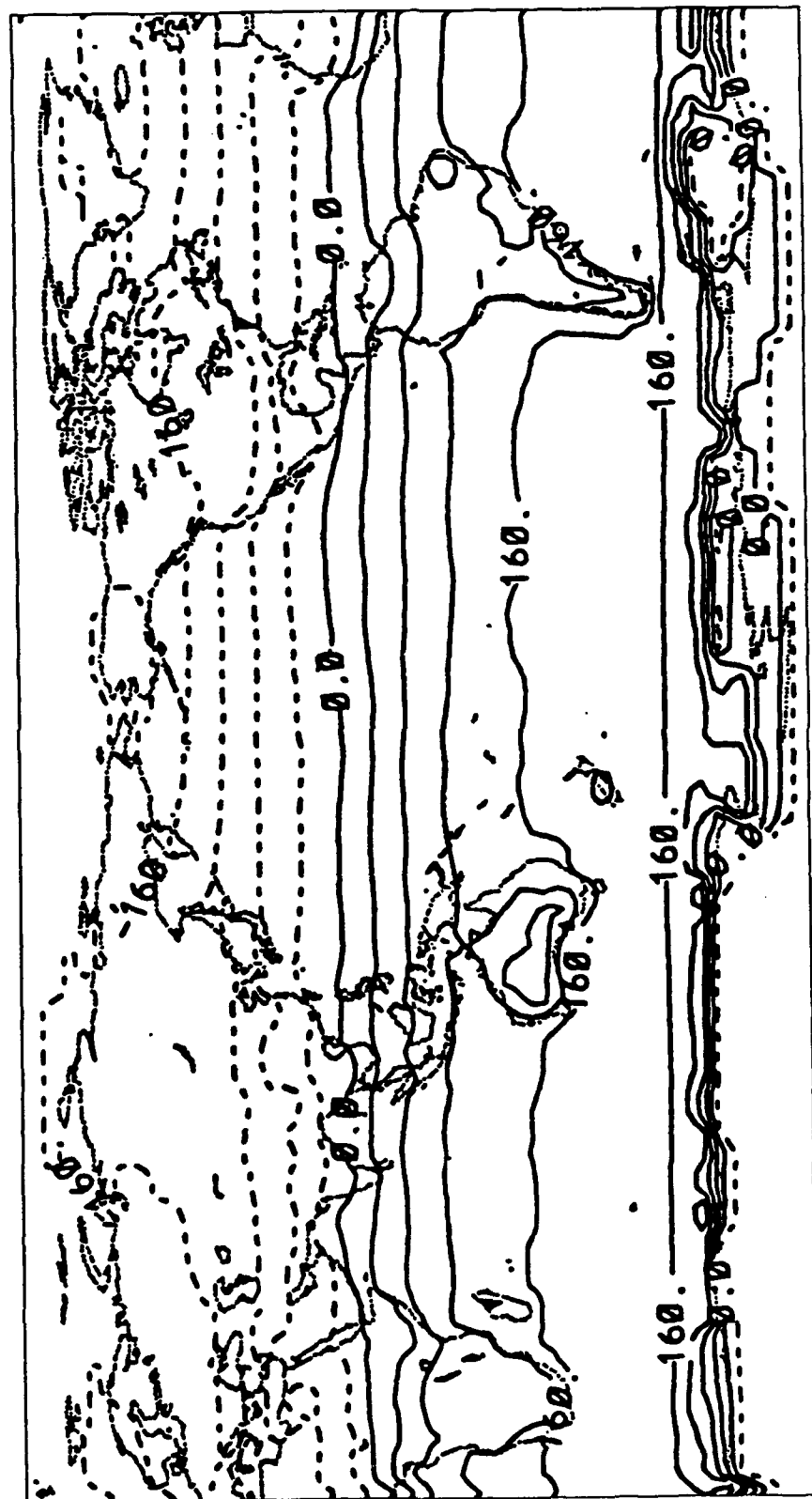


Fig 4.8 January 1979, Model global net TOA flux (W/m^2) for a clear sky. Contour interval is 40 W/m^2 .

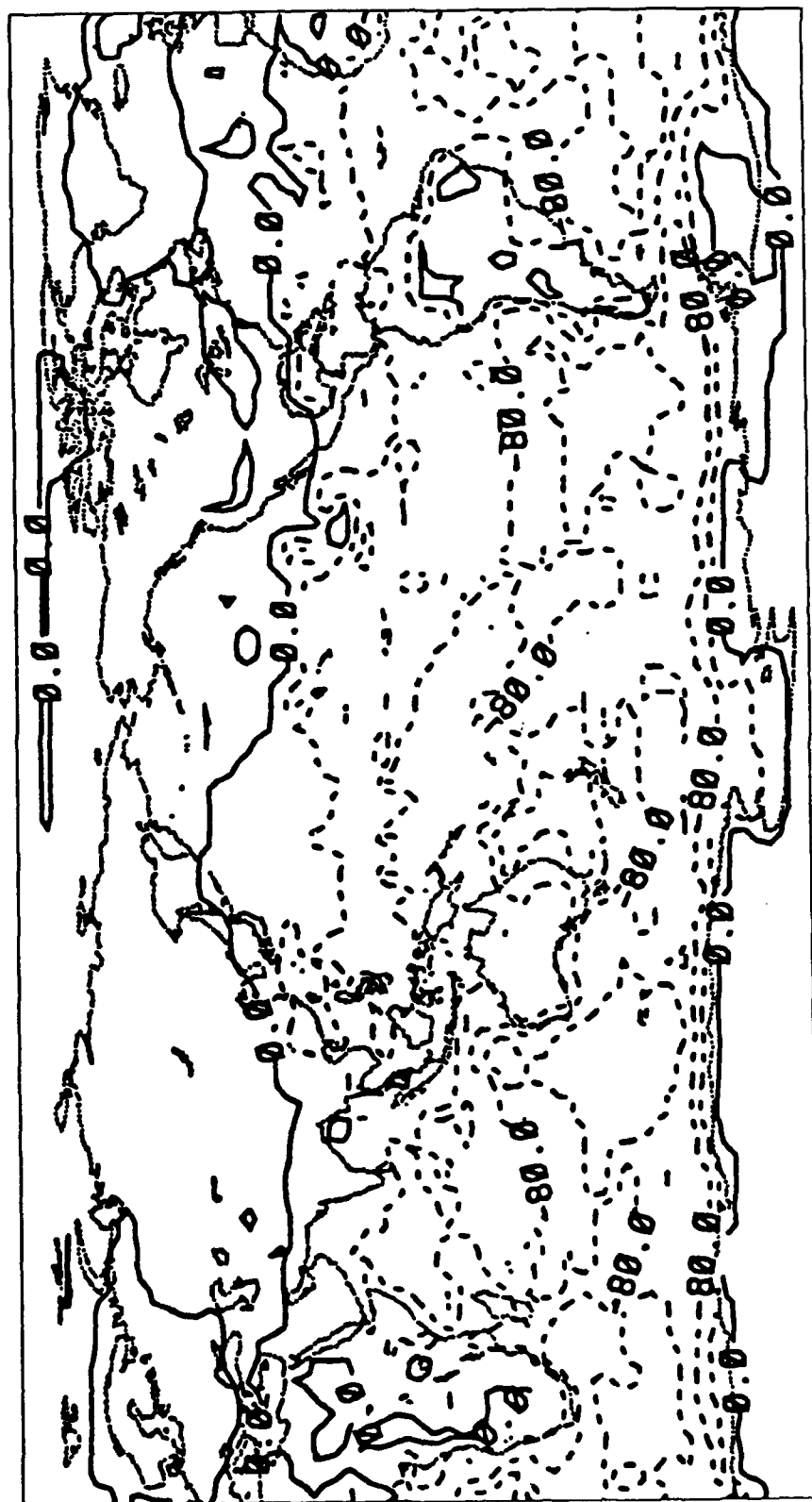


Fig 4.9 January 1979. Model global cloud forcing of the net TOA flux (W/m^2). Contour interval is 40 W/m^2 .

values less than 120 W/m^2 . In those areas of exception, the values did not exceed 40 W/m^2 . With the exception of North Africa, the Northern Hemisphere south of 20°N has negative C_{Nf} values, with some small localized areas being less than -80 W/m^2 . Most of North Africa is positive with some values exceeding 40 W/m^2 due to high clouds and the relatively high reflectivity of the desert. With the exception of the northwestern Pacific region, the Northern Hemisphere north of 20°N is positive. This area of the Pacific Ocean has negative C_{Nf} with the magnitude of the values greater than 40 W/m^2 . The rest of the Northern Hemisphere has positive C_{Nf} , with values mostly less than 40 W/m^2 . There are a few exceptions, however. Over the United States, there are some areas where the C_{Nf} exceeds 40 W/m^2 , and over the North Atlantic, Europe, and part of the Soviet Union, the C_{Nf} also exceeds 40 W/m^2 , with a small portion north of Great Britain exceeding 80 W/m^2 .

4.2 Surface Fluxes

Net cloud forcing at the surface, C'_{Nf} , is defined in the form

$$C'_{NF} = F'_N - F'_{Nc}, \quad (4.6)$$

where F'_N is the net flux at the surface, and F'_{Nc} is the value for clear skies. C'_{Nf} is a measure reflecting the effect of the presence of clouds. F'_N is a measure of the difference between the solar and IR fluxes at the surface. Figure 4.10 is a plot of the global monthly average surface net flux. From approximately 30°N northward, the Northern Hemisphere has negative net surface fluxes, mostly in the range of -40 W/m^2 , but with a small area in the northeastern Soviet Union being less than -80 W/m^2 . The rest of the earth has a positive



Fig 4.10 January 1979, Model global net surface flux (W/m^2) for a partially cloudy sky. Contour interval is 40 W/m^2 .

net surface flux. There is a narrow latitudinal band from 30°N to 0° where the net surface flux is mostly zonal with values ranging from 0 to 120 W/m^2 . From the equator south to Antarctica, the net surface flux displays a convective pattern with values ranging from about 80 to 160 W/m^2 . In areas like the southwestern African coast, middle Indian Ocean, and southeastern Pacific Ocean off South America, values of the net surface flux exceed 200 W/m^2 due to low total cloud values. Figure 4.11 shows the global monthly average net surface flux for a clear atmosphere. From about 30°N to 10°S , the net surface flux pattern is very zonal with values ranging from 0 to 240 W/m^2 . From 10°S to about 50°S , the values stay in the 240 W/m^2 range except in South Africa, Australia, and South America. The local minima in the tropics of South Africa and South America are in the 200 W/m^2 range with some areas less than 160 W/m^2 . In these areas, there are high surface temperatures and therefore increased IR emission. From 50°S to the Antarctic plateau, there is a rapid decrease in net surface flux from a high of 240 W/m^2 to a low of -40 W/m^2 due to reduced solar flux because of increased surface albedos. Figure 4.12 shows the global monthly average net cloud forcing at the surface. From approximately 30°N to the Arctic, the net cloud forcing is positive, with values in the 40 W/m^2 due to the IR emission being shielded by clouds. From 30°N to the Antarctic Plateau the net cloud forcing is negative due to reduced solar flux. The values generally are in the 80 to 120 W/m^2 range. There are small areas in the South Pacific where the magnitudes exceed -160 W/m^2 . The Antarctic plateau has positive net cloud forcing on the order of 0 to 40 W/m^2 .

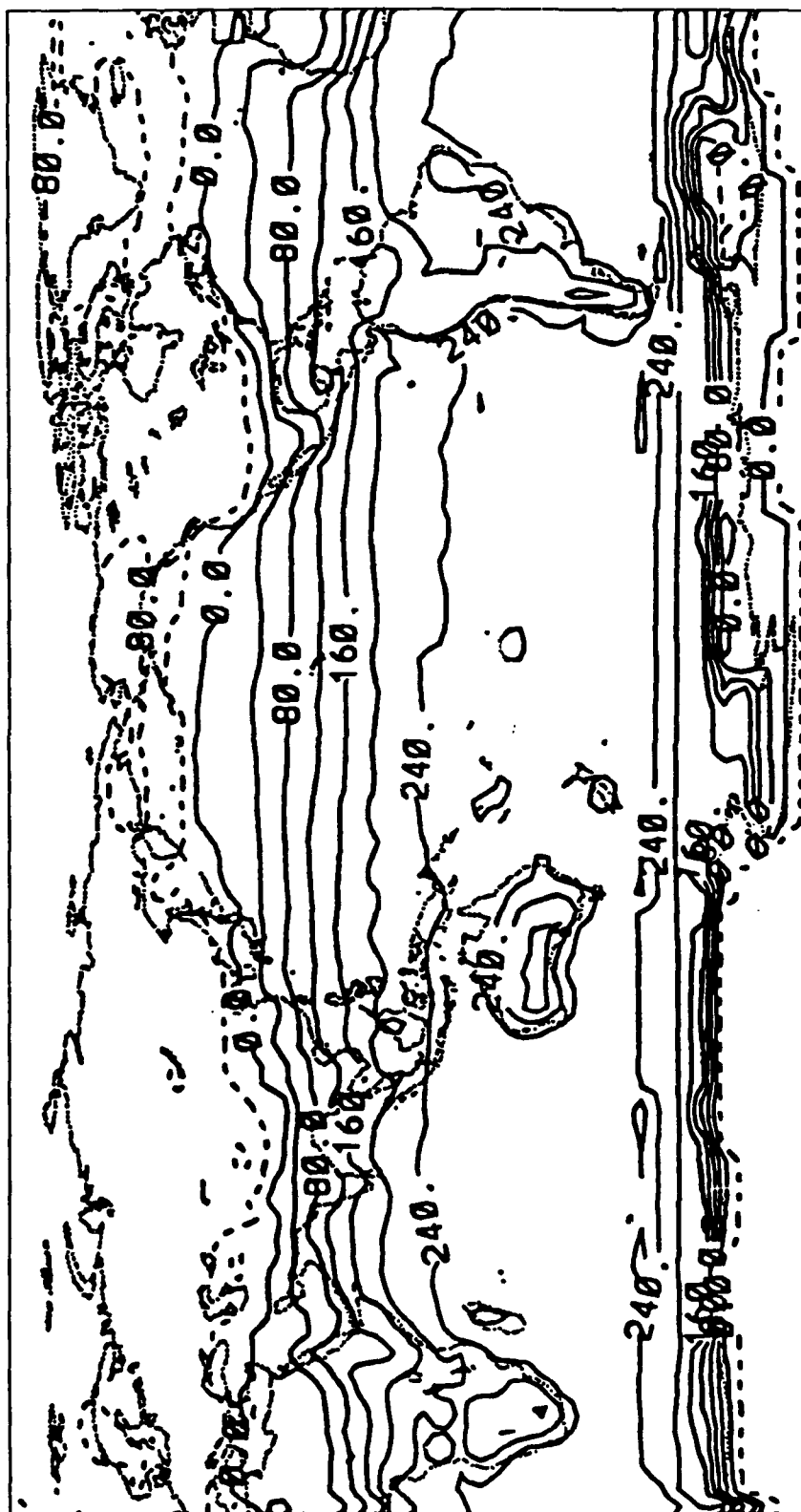


Fig 4.11 January 1979, Model global net surface flux (W/m^2) for a clear sky. Contour interval is 40 W/m^2 .

4.3 Heating Rates

The solar, IR, and net heating rates for January 1979 along with their counterparts for clear, high cloud-free and low cloud-free atmospheres have been zonally averaged. This was done so that the amount of cloud forcing can be determined by the high, low, and total cloud cover.

4.3.1 Forcing Due To All Clouds

Solar cloud forcing in the atmosphere, CH_{fs} , is

$$CH_{fs} = H_s - H_{sc}. \quad (4.7)$$

where H_s is the solar heating rate, and H_{sc} is the value for clear skies (K/day). CH_{fs} is therefore the solar heating due to the contribution of clouds. Figure 4.13a shows the zonally averaged H_s for January 1979. On this and the remaining figures, the x-axis goes from -90° to 90° latitude, and the y-axis goes from 0.05 to 1.00 sigma. Sigma (σ) equals P/P^* , with P^* being the surface pressure. The plot shows that the maximum heating, as would be expected, is in the Southern Hemisphere. There is a maximum solar heating rate at around $45^\circ S$ exceeding 3.0 K/day. There is a secondary maximum of 2.0 K/day in the upper atmosphere due to O_3 absorption. Figure 4.13b depicts the zonally averaged H_{sc} . The maximum of 2.0 K/day is again in the Southern Hemisphere but this time it is at about $10^\circ S$. Again, there is a secondary maximum of 2.0 K/day in the upper atmosphere due to O_3 absorption, as in the cloudy case. Figure 4.13c is a plot of CH_{fs} . The plot indicates that for January the maximum heating occurs at about $50^\circ S$ and at 0.7 σ at a value of 2.0 K/day due to a cloud cover maxima at 50° to $60^\circ S$. There is a minimum below the clouds close to

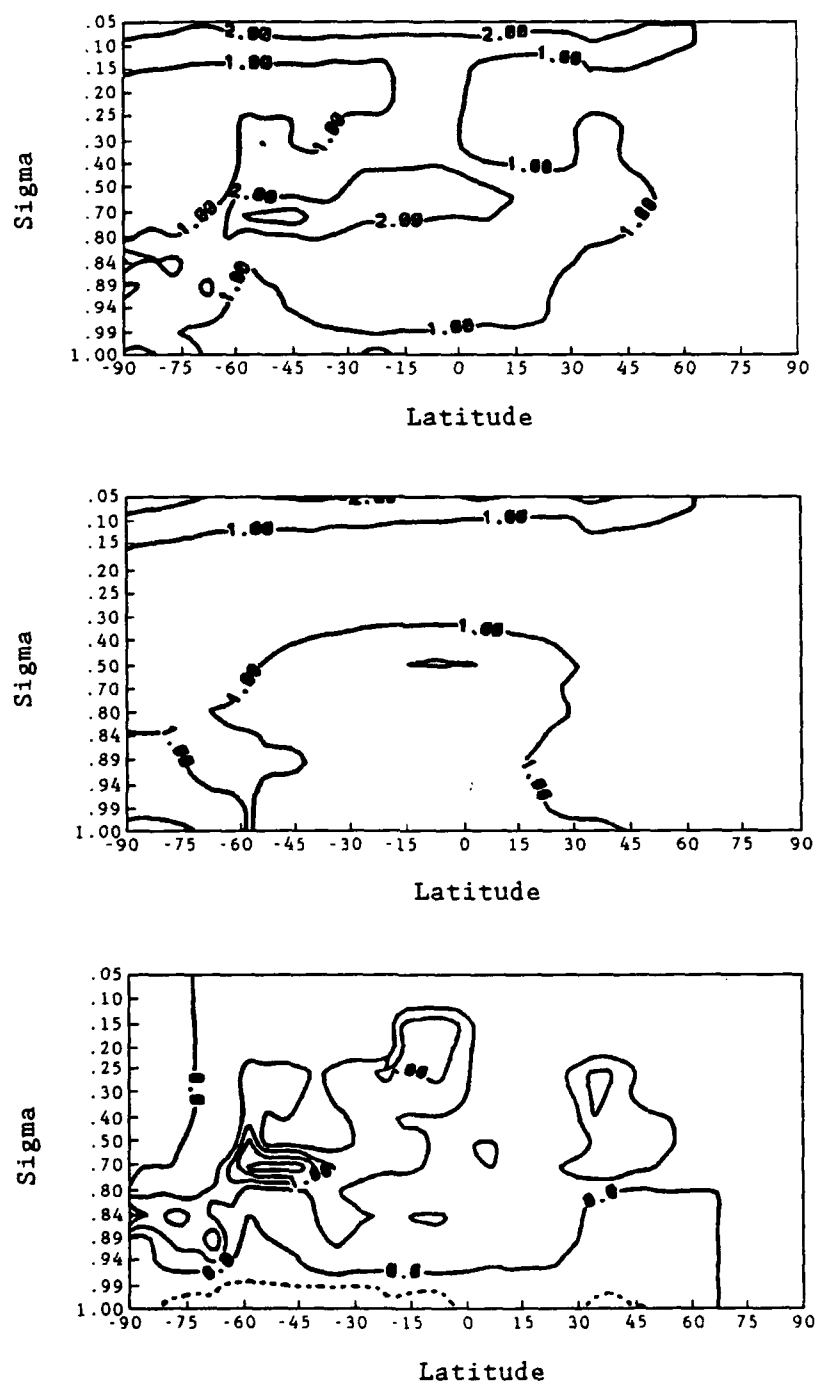


Fig 4.13 January 1979 solar heating rate. a) cloudy, contour interval 1K/day. b) clear, contour interval 1K/day, and c) solar cloud forcing, contour interval .5K/day.

the surface of less than -0.5 K/day due to attenuation of solar energy by clouds. This figure also indicates that the clouds cause a maximum of solar heating above the clouds due to the reflection of solar fluxes.

Cloud IR forcing, CH_{IRf} , is defined by

$$CH_{IRf} = H_{IR} - H_{IRc}. \quad (4.8)$$

where H_{IR} denotes the IR heating rate, and H_{IRc} is the value for clear skies. CH_{IRf} is therefore the IR heating due to the contribution from clouds. Figure 4.14a illustrates the zonally averaged H_{IR} for January 1979. Middle atmospheric cooling is on the order of -2.0 K/day due to the presence of middle clouds, with a secondary maximum of -2.0 K/day occurring near the surface due to the absorption of H_2O . The maximum of IR heating occurs above the primary maximum of IR cooling, with a secondary maximum of IR heating occurring between the aforementioned maxima of IR cooling. Figure 4.14b shows the zonally averaged H_{IRc} . Comparing this figure to the previous one, the areas of IR heating (cooling) here are more centrally located but are not as intense. In this case the maximum IR cooling occurs at the surface centered at about $10^\circ S$ (ITCZ) with a value of ≈ -4.0 K/day due to the H_2O continuum absorption. The only area of IR heating occurs at TOA centered at about $10^\circ S$ with a value less than 1.0 K/day. Figure 4.14c displays the zonally averaged CH_{IRf} . This figure shows the IR heating rate is negative (cooling) above the middle clouds due to cloud top emission, and it is positive (heating) below the clouds due to the trapping of thermal radiation emitted from the surface and lower atmosphere.

Net cloud forcing for atmospheric heating, CH_{Nf} , is

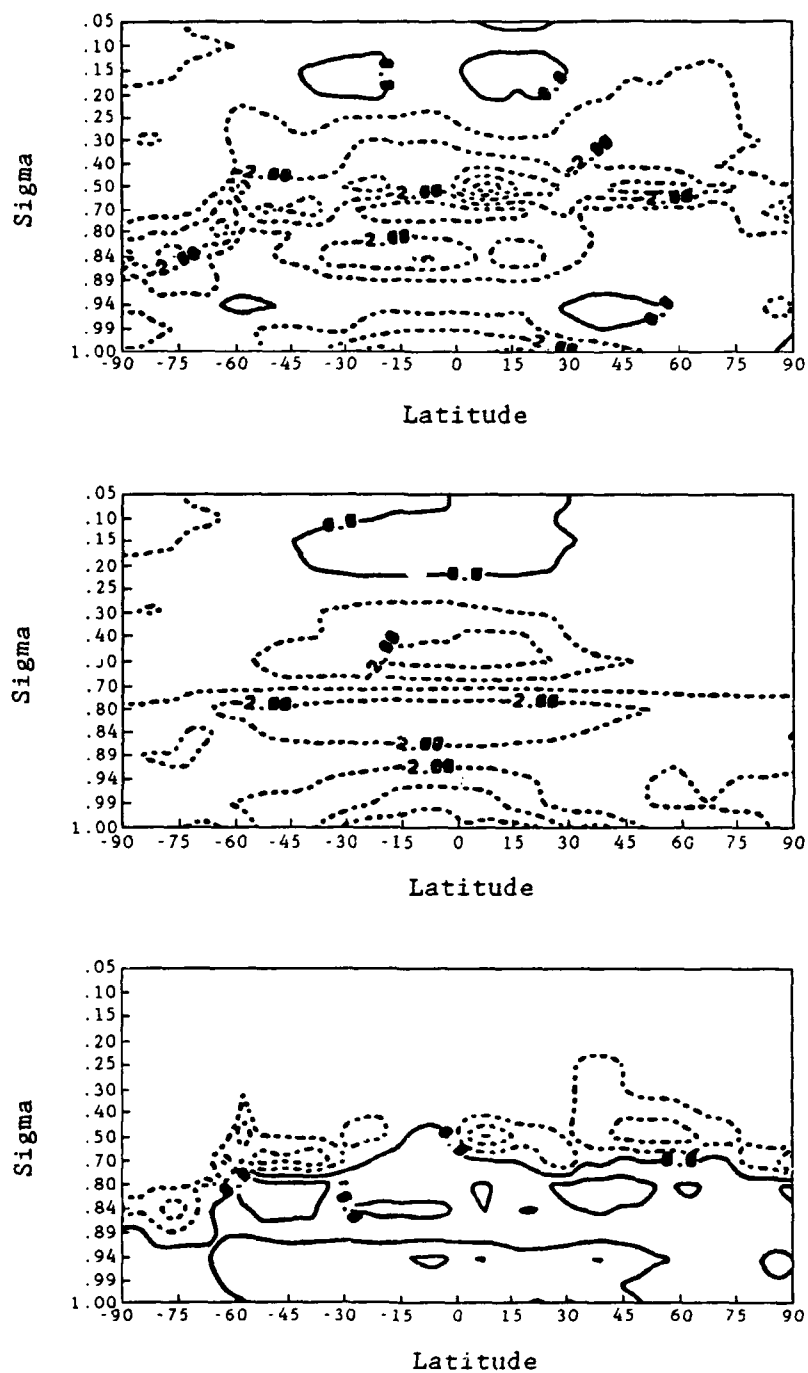


Fig 4.14 January 1979 IR heating rate, a) cloudy, contour interval 1K/day, b) clear, contour interval 1K/day, and c) IR cloud forcing, contour interval .5K/day.

$$CH_{Nf} = H - H_c. \quad (4.9)$$

where H is

$$H = H_s - H_{IR}. \quad (4.10)$$

and H_c is

$$H_c = H_{sc} - H_{IRc}. \quad (4.11)$$

The zonally averaged H for January 1979 is shown in Figure 4.15a. The largest area of positive (warming) net heating occurs in the upper third of the atmosphere. Heating pockets are due to the presence of middle and low clouds. While the maximum (2.0 K/day) is in the Northern Hemisphere (due to O_3 absorption), the majority of the net heating area is in the Southern Hemisphere (due to heating above the clouds from the reflection of solar fluxes). The largest area of negative (cooling) net heating occurs in the middle atmosphere and is entirely in the Northern Hemisphere (due to cloud top emission), with a local minimum of -3.0 K/day. Figure 4.15b shows the zonally averaged H_c . The top half of the atmosphere is entirely positive (warming) net heating with the same maxima features (2.0 K/day) at TOA (due to O_3 absorption). The bottom half of the atmosphere is predominately negative (cooling) net heating with the major negative feature being near the surface, centered at about $5^\circ S$, and with a value less than -3.0 K/day. This is produced by large IR cooling rates associated with the H_2O continuum absorption. In the bottom half of the atmosphere over the Antarctic there is a small area of positive (warming) net heating, with a local maxima of 1.0 K/day due to multiple reflections of solar fluxes between the ice and the atmosphere above the ice. Figure 4.15c displays the zonally averaged

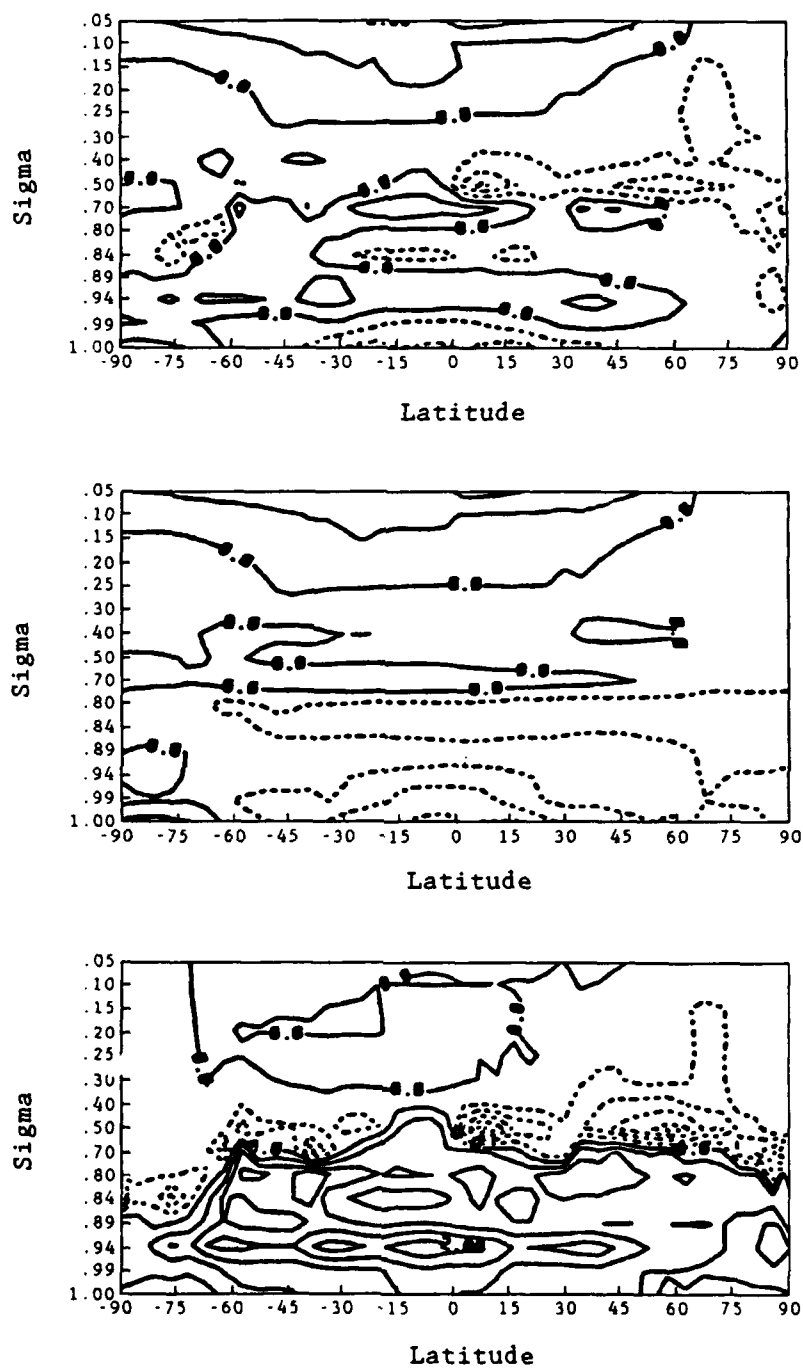


Fig 4.15 January 1979 net heating rate, a) cloudy, contour interval 1K/day, b) clear, contour interval 1K/day, and c) net cloud forcing, contour interval .5K/day.

CH_{Nf} . This figure shows the net effects of clouds. Below the clouds the warming due to solar and IR forcing is greater than the small amount of cooling near the surface due to solar forcing. The maximum warming (2.0 K/day) is in the lower atmosphere, fairly well centered north and south, but biased slightly to the south (5°S). There is a small area of warming directly above the center of the maximum warming (5°S). Directly above the clouds is a band of cooling with two primary maxima of cooling (-2.0 K/day) located at 5°N and 55°N. There are two secondary areas of cooling (-1.5 K/day) located at 40°S and at 75°S. This net cooling is a result of the strong IR being greater than the solar heating at the cloud tops. Above this area of cooling, there is a second area of warming due primarily to the reflection of the solar fluxes from tops of the clouds in the upper atmosphere.

4.3.2 Forcing Due To High Clouds

Cloud solar forcing due to high clouds (CH'_{fs}) which are clouds above 0.5 σ , is

$$CH'_{fs} = H_s - H'_{sc}. \quad (4.12)$$

where H'_{sc} is the atmospheric solar heating rate without the contribution of high clouds. Figure 4.16a shows the zonal average H_s for January 1979. Figure 4.16b depicts the zonal average of H_{sc} . The only difference between figures 4.16a and 4.16b is a lack of warming from 0.5 σ up to 0.15 σ . Figure 4.16c illustrates the zonal average of CH'_{fs} . Three areas of warming, in the range of 0.5 and 1.0 K/day, occur between 0.5 and 0.15 σ . These areas occur in the Southern Hemisphere storm track, ITCZ, and Northern Hemisphere storm track.

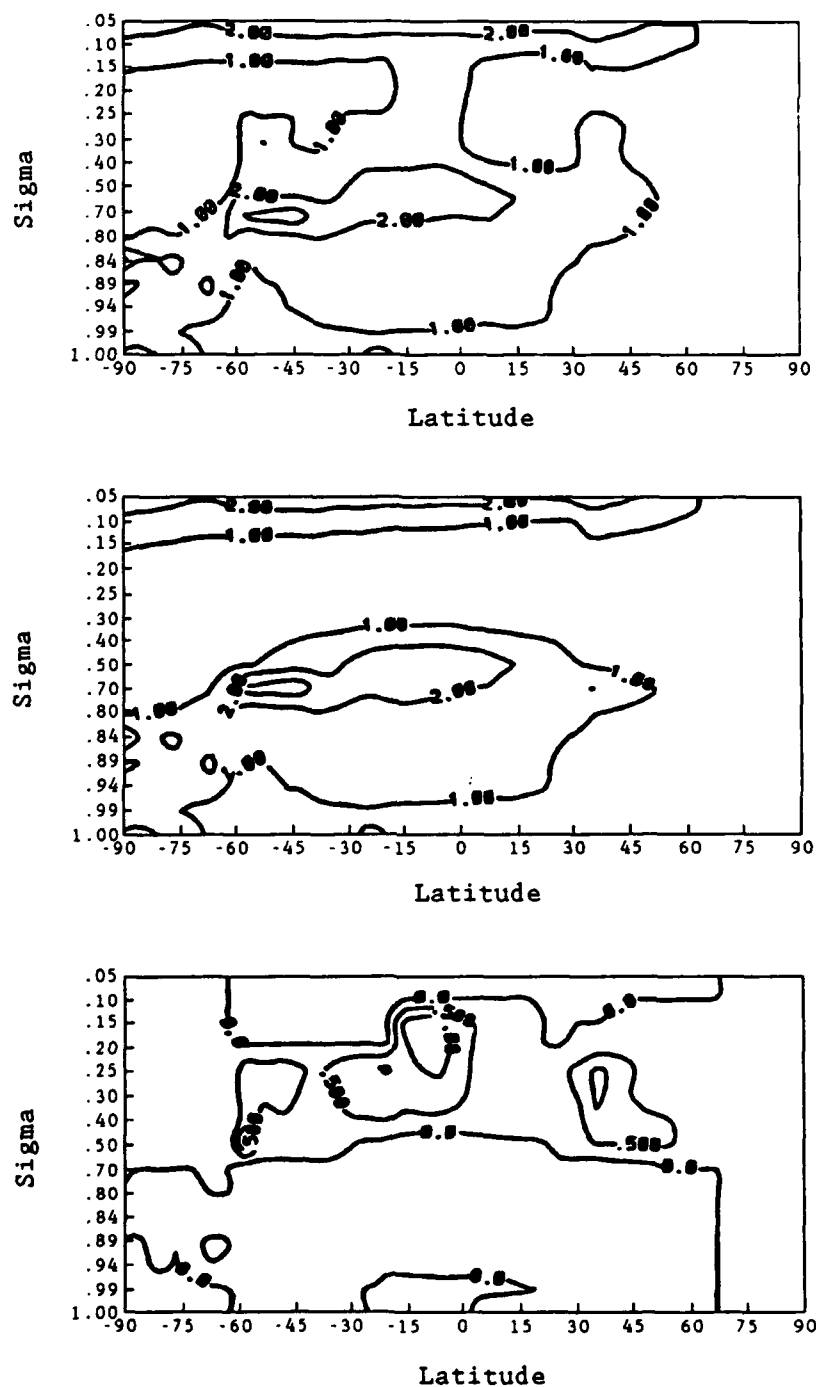


Fig 4.16 January 1979 solar heating rate, a) cloudy, contour interval 1K/day, b) cloudy without high clouds, contour interval 1K/day, and c) solar cloud forcing, contour interval .5K/day.

Warming in each these areas is due to the solar flux absorption of the high clouds.

Cloud IR forcing due to high cloud, $CH'IR_f$, is

$$CH'IR_f = HIR - H'IR_c. \quad (4.13)$$

where $H'IR_c$ is the atmospheric IR heating rate without the contribution from high clouds. Figure 4.17a shows the zonal average of H_{JR} for January 1979. Figure 4.17b depicts the zonal average of $H'IR_c$. Comparing figures 4.17a and 4.17b, it is clear that removing the high clouds causes an increase in the emission from the warmer middle clouds. Subsequently, the cooling at the middle cloud top increases. Figure 4.17c shows the zonal average of $CH'IR_f$. IR heating produced by the high clouds leads to warming, in the range of 0.0 to 3.0 K/day, below the clouds over the areas of the southern storm track ($60^\circ S$), ITCZ ($10^\circ S$), and the northern storm track ($45^\circ N$). The cooling, -1.0 to -2.0 K/day, above the high clouds in the area of the northern and southern storm tracks is due to cloud top emission.

Net cloud forcing due to high clouds, $CH'N_f$, is

$$CH'N_f = H - H'_c. \quad (4.14)$$

where H'_c is the net atmospheric heating rate without the contribution of high clouds, defined by

$$H'_c = H'_s - HIR_c. \quad (4.15)$$

Figure 4.18a shows the zonal average of the H for January 1979. Figure 4.18b depicts the zonal average of H'_c for January 1979. Removing the high clouds causes additional cooling at the top of the middle clouds and an increase in warming above the high clouds. Figure 4.18c illustrates the $CH'N_f$. High clouds cause a net warming

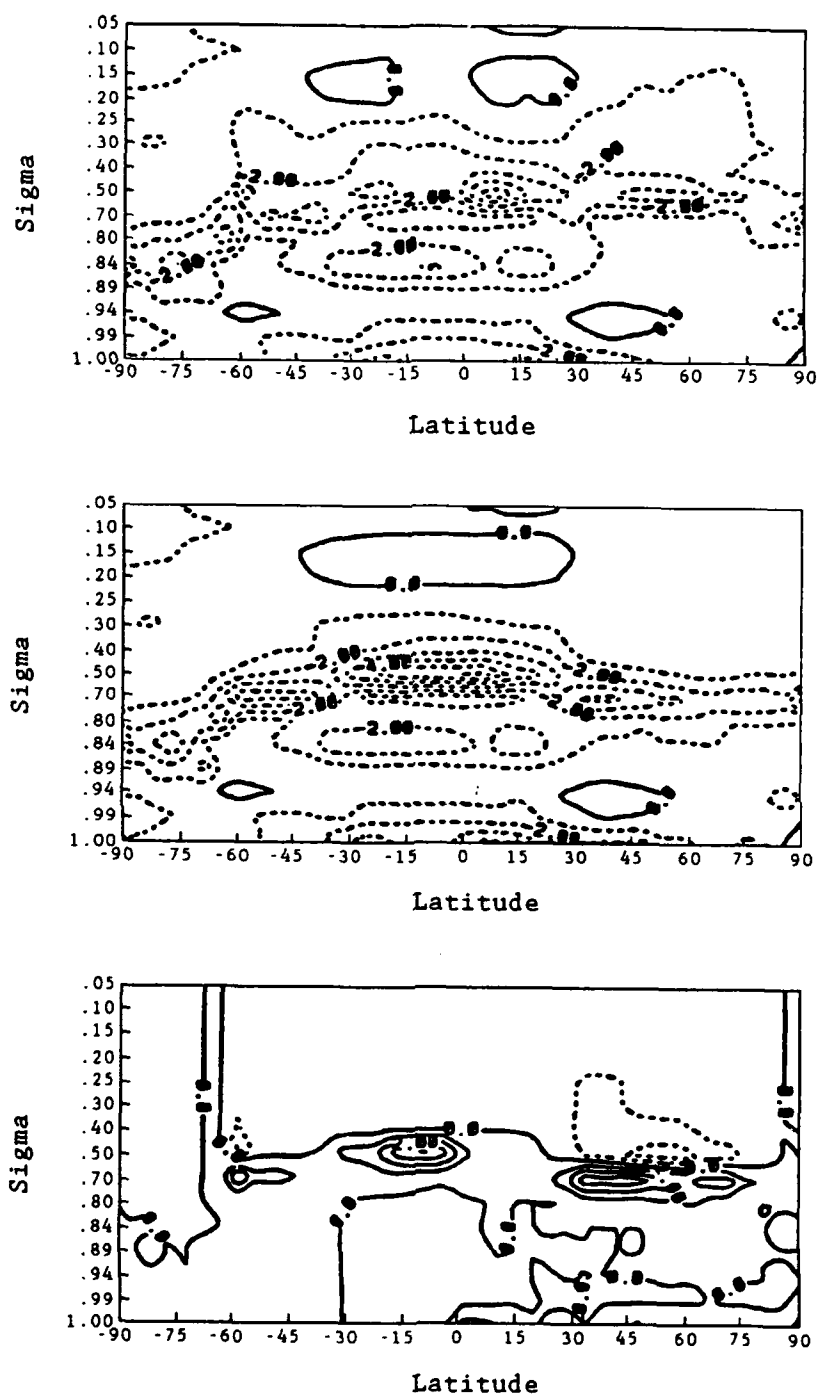


Fig 4.17 January 1979 IR heating rate. a) cloudy, contour interval 1K/day, b) cloudy without high clouds, contour interval 1K/day, and c) IR cloud forcing, contour interval .5K/day.

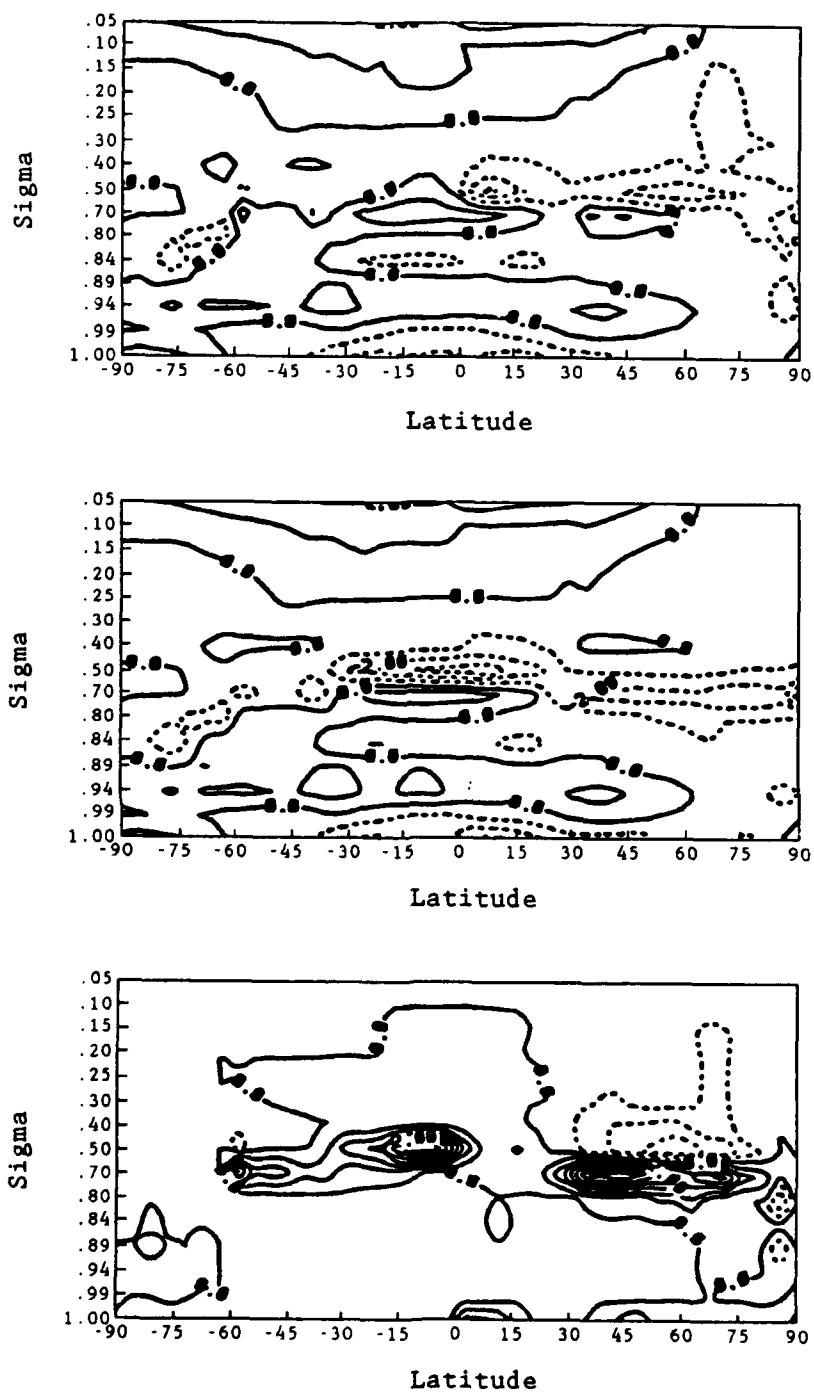


Fig 4.18 January 1979 net heating rate. a) cloudy, contour interval 1K/day. b) cloudy without high clouds, contour interval 1K/day, and c) net cloud forcing, contour interval .5K/day.

immediately below the clouds. This occurs mostly in the area of the southern storm track (1.0 K/day), ITCZ (2.0 K/day), and the northern storm track (3.0 K/day). Also, there is cooling in the location of high clouds with a value of 1.0 K/day that is associated with the northern storm track.

4.3.3 Forcing Due To Low Clouds

Cloud solar forcing due to low clouds (0.94 to 0.8σ), CH''_{fs} , is

$$CH''_{fs} = H_s - H''_{sc}. \quad (4.16)$$

where H''_{sc} is the atmospheric solar heating rate without the contribution of low clouds. Figure 4.19a shows the zonal average of the H_s for January 1979. Figure 4.19b depicts the zonal average of H''_{sc} . For the cases with no low clouds, there is additional cooling at the cloud level. Also, removing the low clouds causes an increase in warming below the low clouds ($\sigma > 0.94$). Figure 4.19c illustrates the zonal average of CH''_{fs} . Low clouds cause a warming in them (in the range of -0.5 to 0.0 K/day), and they cause a cooling below.

Cloud IR forcing due to low clouds, CH''_{IRf} , is

$$CH''_{IRf} = H_{IR} - H''_{IRc}. \quad (4.17)$$

where H''_{IRc} is the atmospheric IR heating rate without the contribution of low clouds. Figure 4.20a shows the zonal average of H_{IR} for January 1979. Figure 4.20b depicts the zonal average of H''_{IRc} . Removing the low clouds causes a warming in the position of these clouds in the areas of the southern storm track ($60^\circ S$), ITCZ ($10^\circ S$), and northern storm track ($45^\circ N$). Figure 4.20c illustrates the zonal average of CH''_{IRf} . This figure shows that low clouds cause

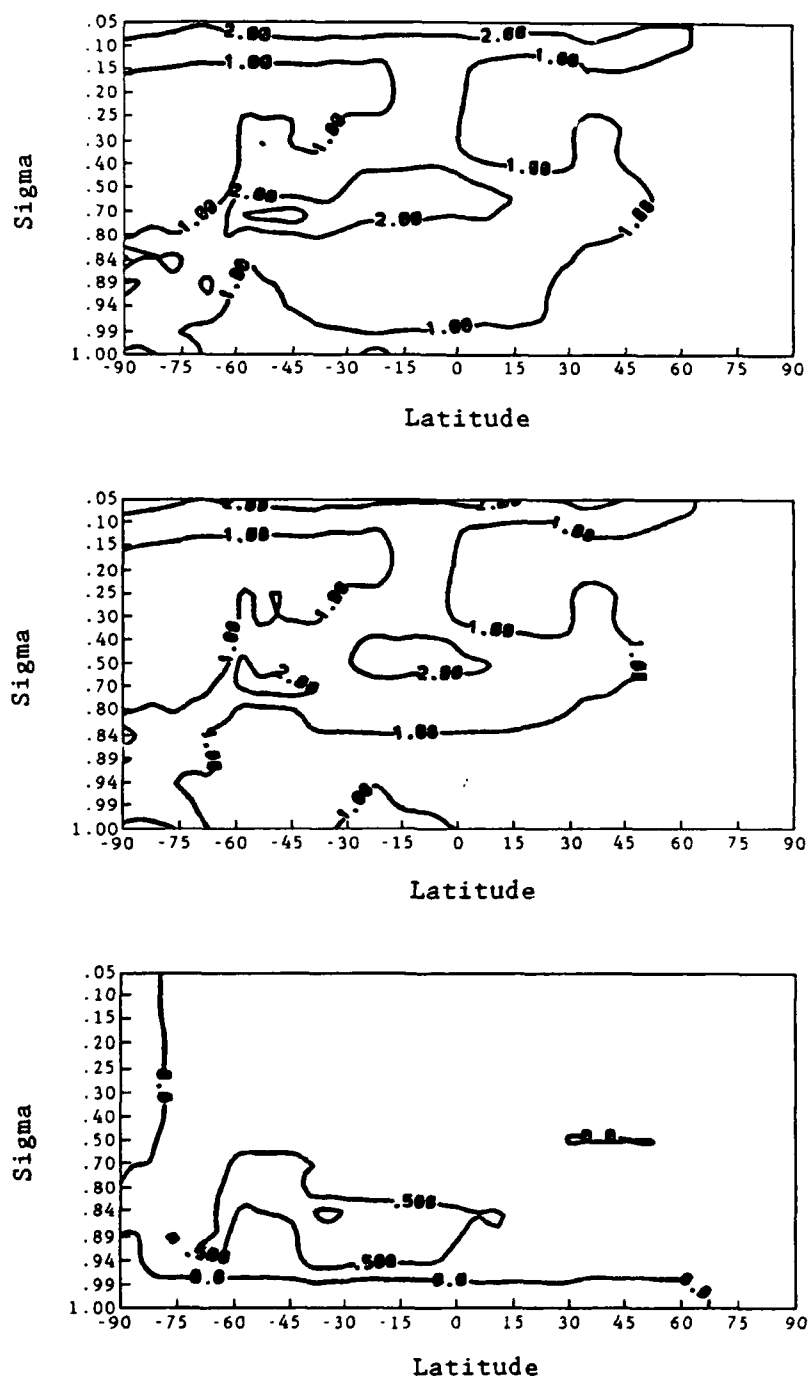


Fig 4.19 January 1979 solar heating rate. a) cloudy, contour interval 1K/day. b) cloudy without low clouds, contour interval 1K/day. and c) solar cloud forcing, contour interval .5K/day.

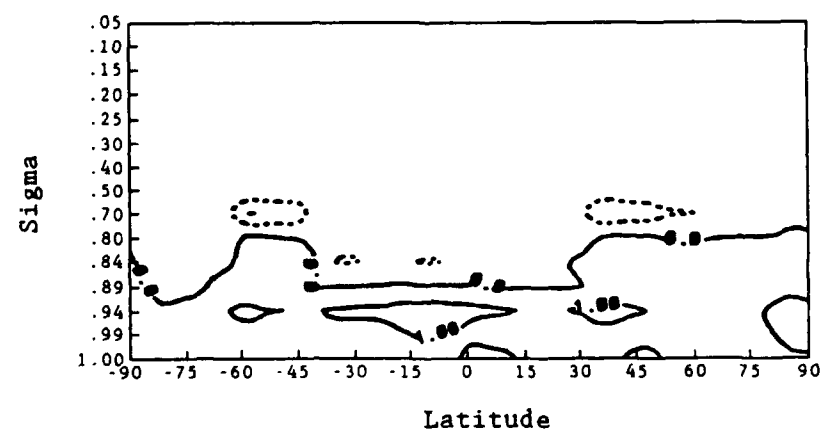
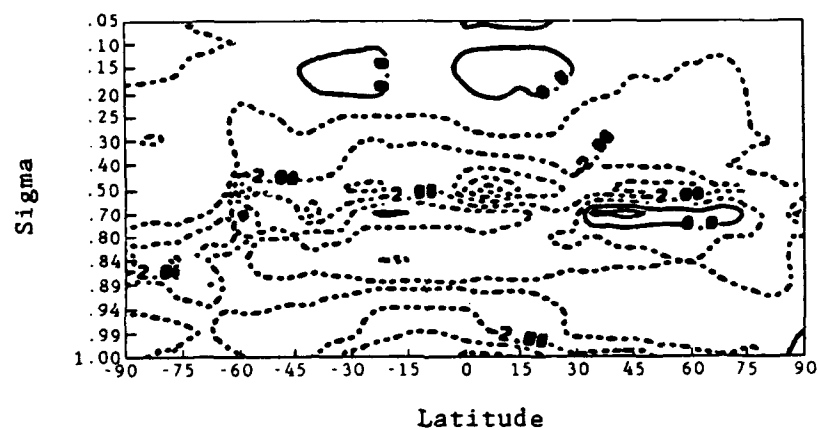


Fig 4.20 January 1979 IR heating rate, a) cloudy, contour interval 1K/day, b) cloudy without low clouds, contour interval 1K/day, and c) IR cloud forcing, contour interval .5K/day.

cooling (≈ -1.0 K/day) near the cloud top and warming (≈ 1.0 K/day) near the cloud base.

Net cloud forcing due to low clouds, CH''_{Nf} , is

$$CH''_{Nf} = H - H''_c. \quad (4.18)$$

where H''_c is the net atmospheric heating rate without the contribution of low clouds, defined by

$$H''_c = H''_s - H''_{IRc}. \quad (4.19)$$

Figure 4.21a shows the zonal average of H for January 1979. Figure 4.21b depicts the zonal average of H''_c . Removing the low clouds causes a net warming above the location of the clouds in the southern storm track ($60^\circ S$), ITCZ ($10^\circ S$), and northern storm track ($45^\circ N$). Also, it causes a net cooling below these low clouds in those regions. Figure 4.21c illustrates the zonal average of CH''_{Nf} . A net cooling (≈ -0.5 to -1.0 K/day) of the atmosphere at the low cloud tops and a net warming (≈ 0.5 to 2.0 K/day) at the low cloud base and below are shown.

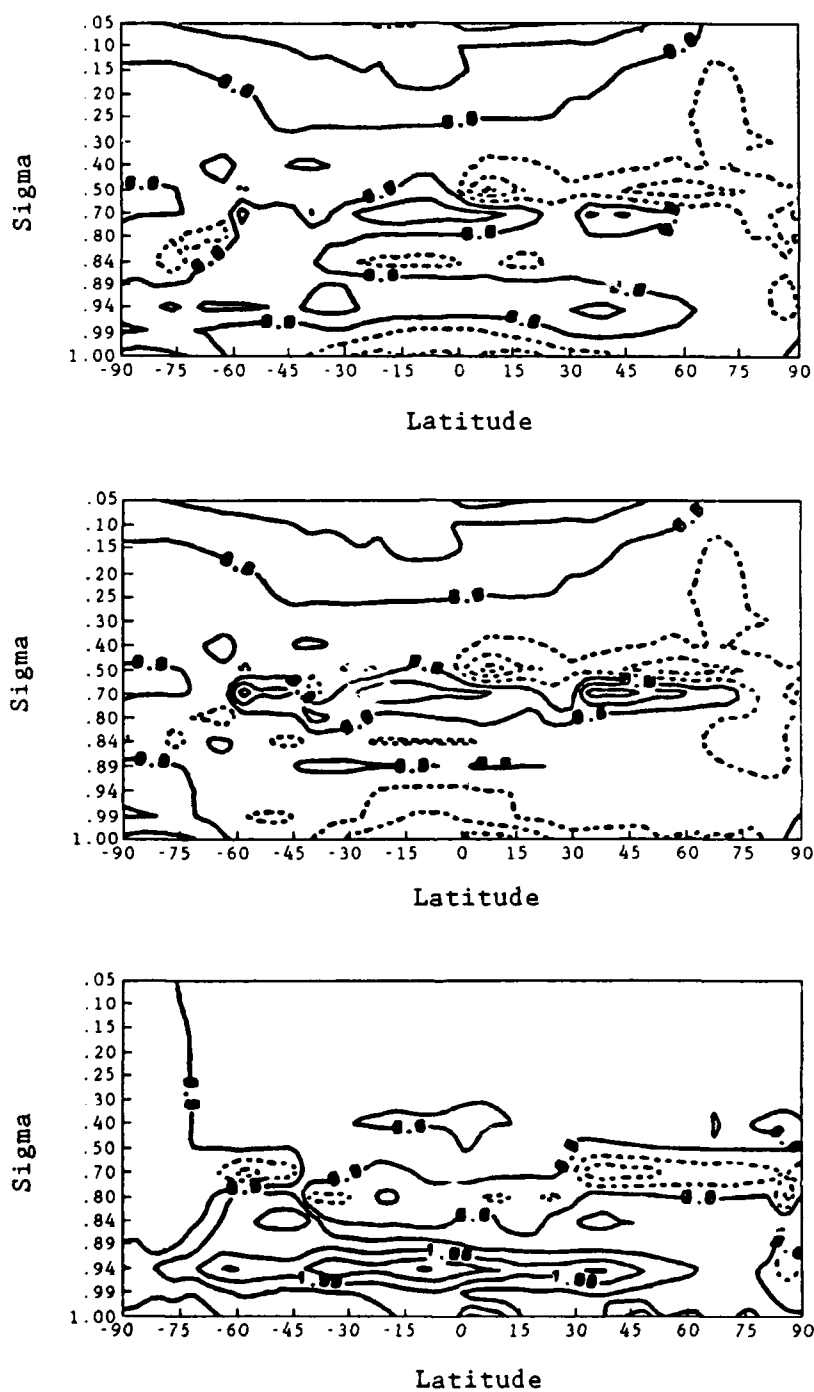


Fig 4.21 January 1979 net heating rate, a) cloudy, contour interval 1K/day, b) cloudy without low clouds, contour interval 1K/day, and c) net cloud forcing, contour interval .5K/day.

CHAPTER 5

SUMMARY AND CONCLUSIONS

This thesis studied the radiative effects of clouds on TOA and surface radiation budgets, as well as cloud radiative forcing. In order to do this, the model input datasets had to be created and verified. The first dataset discussed was the surface albedo. A global surface albedo dataset was constructed using the same methodology used by Griffin (1987) to construct his northern hemisphere surface albedo dataset. A zonal average of the dataset was determined and this dataset was verified by comparing it to Hummel and Reck (1979). The zonally averaged model surface albedo differed by no more than 15% when compared to Hummel and Reck (1979).

The last input dataset to be created and verified was the global cloud climatology. The AFGWC 3DNEPH was used. The study used the cloud climatology that Griffin (1987) created for the northern hemisphere for the months of January and July 1979. The same methodology used to create the northern hemisphere cloud climatology was used to create the southern hemisphere cloud climatology for the same months. The two climatologies were combined to form a global cloud climatology. This was then compared to the global cloud climatology created by Henderson-Sellers (1986) for the same months. The two datasets differed by no more than 10%.

Next, the model's datasets were incorporated into a modified version of a radiation model that was developed by Ou and Liou (1987). This radiation model was fine-tuned at TOA by comparing its computed results to the ERB TOA results. Generally, the computed solar and IR fluxes were within 20 W/m^2 of the ERB results. Solar and IR surface radiation budgets were then computed and discussed. Comparisons of the computed solar and IR fluxes at the surface were made with Griffin (1987) and are within 10 W/m^2 .

Cloud forcing experiments were then performed for January 1979. The cloud solar forcing results were compared with those presented by Slingo and Slingo (1988) and found to be low by 40 W/m^2 . However, they used persistent January cloud cover, and since solar flux is very sensitive to cloud amount, this could account for the difference between the results. The model was also low when compared to the ERB data by 20 W/m^2 . The presented cloud IR forcing results were compared with those presented by Slingo and Slingo (1988) and were found to be within 10 W/m^2 . The difference between the solar and IR results can be explained by the following reasons. First, as previously stated, solar flux is four times more sensitive to cloud amount than the IR flux (Koenig, 1987). Second, the previous statement tied to the differences in the construction of the two cloud climatologies.

Finally, cloud forcing at TOA experiments involving heating rates were performed and discussed. First, the atmospheric solar and IR heating rates were analyzed. Then, the solar and IR contributions were combined and the net atmospheric heating rate was analyzed. The cloud solar forcing results showed that for January the maximum

heating (2.0 K/day) occurred at $\approx 50^\circ\text{S}$ and at $\sigma=0.7$. This was due to a cloud cover maxima at 50° to 60°S . The minima (-0.5 K/day) existed below the clouds close to the surface. This was due to attenuation of the solar fluxes by the clouds. There was also a maxima (1.0 K/day) above the clouds due to the reflection of solar fluxes. Next, the cloud IR forcing results showed the maximum heating (0.5 to 1.0 K/day) occurred below the clouds due to the trapping of thermal radiation emitted from the surface and the atmosphere. The minima (-0.5 to -1.0 K/day) existed above the middle clouds due to cloud top emission. Last, the net cloud radiative forcing for atmospheric heating results showed that the maximum warming (2.0 K/day) occurred in the lower atmosphere. The minima heating (-2.0 K/day) existed above the clouds as a result of the strong IR cooling being greater than the solar heating at the cloud top. Above this area of cooling it was shown that there was a second area of warming (0.0 to 0.5 K/day) primarily due to the reflection of solar fluxes from the cloud tops in the upper atmosphere. Subsequently, the cloud forcing experiments involving heating rates with high and low clouds alone were performed and discussed. Atmospheric solar heating (0.5 to 1.0 K/day) with high clouds occurs primarily in three areas between $\sigma=0.5$ and $\sigma=0.15$. These three areas of warming occur in the Southern Hemisphere storm track, ITCZ, and in the Northern Hemisphere storm track. Each one of these areas is due to the high cloud absorption of solar flux. Next, atmospheric IR heating (0.0 to 3.0 K/day) with high clouds was shown to exist in the same areas as the solar heating, but it occurs below the high clouds due to H_2O absorption. Above these same clouds

cooling (-1.0 to -2.0 K/day) occurs because of cloud top emission. Last, the solar and IR atmospheric heating of high clouds were combined to obtain the net atmospheric heating rate. The results showed that high clouds cause a net warming (1.0 to 3.0 K/day) immediately below them and cooling (\approx 1.0 K/day) above them.

Finally, atmospheric heating by low clouds was investigated. First, it was shown with respect to solar heating, that low clouds cause a warming (0.5 to 1.0 K/day) in them and a cooling (0.0 to -0.5 K/day) below them. Second, it was then shown with respect to IR heating, that low clouds cause cooling (\approx -1.0 K/day) near the low cloud top and warming (\approx 1.0 K/day) near the low cloud base. Last, the combined effects of solar and IR atmospheric heating were investigated. The results showed that there is a net atmospheric cooling (\approx -0.5 to -1.0 K/day) at the low cloud tops, and a net atmospheric warming (\approx 0.5 to 2.0 K/day) at the low cloud base and below.

To summarize this study, high quality input data were used to produce the global radiation budgets and cloud radiative forcing. Studies concerning the sensitivity of high and low clouds to heating rates were made. From these studies it was shown that the net effect high clouds cause warming below and cooling above. Also, it was shown that low clouds cause cooling at the cloud tops and warming at the base and below.

REFERENCES

- GARP/JOC. 1978: JOC Study Conference on Parameterization of Extended Cloudiness and Radiation for Climate Models. GARP Climate Dynamics Sub-programme. World Meteorological Organization. Oxford, England. 37 pp.
- Gordon, C.T., R.D. Hovanec, and W.F. Stern. 1984: Analysis of monthly mean cloudiness and their influence upon model diagnosed radiative fluxes. J. Geophys. Res., 89, 4713-4738.
- Griffin, M.K.. 1987: The role of clouds in surface radiation budgets. Ph.D. dissertation, University of Utah. 334 pp.
- Griffin, M.K., K.N. Liou, and G. Koenig. 1987: Cloud climatology derived from the AFGWC 3D-Nephanalysis for January and July 1979. AFGL Tech. Report, 87-0122. Air Force Geophysical Laboratory, Hanscom AFB, MA. 56 pp.
- Hartmann, D.L., and D.A. Short. 1980: On the use of radiation budget statistics for studies of clouds and climate. J. Atmos. Sci., 37, 1233-1250.
- Henderson-Sellers, A., 1986: Layered cloud amounts for January and July 1979 from 3D-Nephanalysis. J. Clim. Appl. Meteor., 25, 118- 132.
- Hummel, J.R., and R.A. Reck. 1979: A global surface albedo model. J. Appl. Meteor., 18, 239-253.
- Koenig, C.G., 1985: Cloud and radiation budget studies. Ph.D. dissertation, University of Utah, 307 pp.
- Koenig, C.G., K.N. Liou, and M.K. Griffin. 1987: An investigation of cloud/radiation interactions using three-dimensional Nephanalysis and Earth Radiation Budget data bases. J. Geophys. Res., 92, 5540-5554.
- Liou, K.N., and G.D. Wittman. 1979: Parameterization of the Radiative Properties of Clouds. A. Meteor. Soc., 36, 1262-1273.
- Matthews, E., 1985: Atlas of archived vegetation, land use and seasonal albedo data sets. Tech. Memo., 86199, NASA Goddard Space Flight Center, New York, NY. 54 pp.

- McClatchey, R.A., R.W. Fenn, J.E.A. Selby, F.E. Volz and J.S. Garing. 1971: Optical properties in the atmosphere. Environmental Research Paper, 354. ARCRL-71-0279. 81 pp.
- Oort, A.H., and E.M. Rasmusson. 1971: Atmospheric Circulation Statistics. NOAA Professional Paper, 5. U.S. Department of Commerce, 323 pp.
- Ou, S.C., and K.N. Liou. 1988: Development of radiation and cloud parameterization programs for AFGL global models. Final Report. Contract F19628-84-K-0040 (AFGL-TR-88-0018). University of Utah, 88pp.
- Ramanathan, V., 1985: Scientific use of surface radiation budget data for climate studies. Position paper for Panel 1 Workshop on Surface Radiation Budget for Climate Applications, Columbia, MD, 30 pp.
- Slingo, A., and J.M. Slingo. 1988: The response of a general circulation model to cloud longwave radiative forcing. I: Introduction and initial experiments. Q.J.R. Meteor. Soc., 114, 1027-1062.
- Vonder Haar, T.H., and V.E. Suomi. 1971: Measurements of the earth's radiation budget from satellites during a five-year period. I: Extended time and space means. J. Atmos. Sci., 28, 305-314.

VITA

Name	Bruce G. Mitchell
Birthdate	27 September 1954
Birthplace	Los Angeles, California
Universities	Rio Hondo Community College Whittier, California 1972-1974 Fort Lewis College Durango, Colorado 1978-1979 Colorado School of Mines Golden, Colorado 1979-1981 Creighton University Omaha, Nebraska 1984-1985
Degree	B.S., 1981, Petroleum Engr. Colorado School of Mines
Certificate	1985, Meteorology Creighton University